Rozprawa Doktorska

Nowe Fazy Prototypowych Metalocenów

New Phases of Prototypical Metallocenes

Ida Moszczyńska

Praca wykonana w
Zakładzie Chemii Materiałów Wydziału Chemii
Uniwersytetu im. Adama Mickiewicza w Poznaniu
celem uzyskania stopnia doktora nauk chemicznych

Promotor:

Prof. dr hab. Andrzej Katrusiak

Poznań, 2025

Swoją pracę dedykuję

Wspaniałej rodzinie, w szczególności ukochanemu
mężowi Konradowi i cudownej córeczce Klarze

Podziękowania

Przedstawiona poniżej rozprawa stanowi podsumowanie mojej sześcioletniej pracy, drogi, której nie przeszłam sama, lecz przy wsparciu wielu osób, którym chcę serdecznie podziękować.

Ogromne podziękowania kieruję do promotora mojej pracy doktorskiej **Pana Profesora Andrzeja Katrusiaka** za poświęcony czas i cenne sugestie, które pozwoliły mi lepiej zgłębić temat mojej pracy. Dziękuję także za poczucie humoru i pozytywną energię, którą dzielił się Pan i motywował mnie w momentach gdy nie wszystko układało się idealnie.

Pragnę także podziękować wszystkim pracownikom i doktorantom Zakładu Chemii Materiałów: Ewie Patyk-Kaźmierczak, Ani Olejniczak, Kindze Roszak, Marcinowi Podsiadło, Shivie Batmanghelich, Szymonowi Sobczakowi za pomoc merytoryczną, organizacyjną i koleżeńską atmosferę. Szczególne wyrazy wdzięczności należą się:
Natalii Sacharczuk, nasze cenne, długie rozmowy i światopoglądowe dyskusje często pozwalały mi ujrzeć dany temat z innej perspektywy.
Michalinie Rusek, Twój codzienny uśmiech i życiowe, racjonalne podejście do wielu sytuacji pomagały mi w skupieniu się na małych zadaniach, które starannie wykonane przynosiły satysfakcjonujący, większy efekt.
Paulinie Ratajczyk, dziękuję Ci za Twój spokój, opanowanie, wyważony i zawsze przemyślany komentarz do rzeczywistości.
Fatemeh Safari, dzięki Tobie dowiedziałam się z praktycznej strony ile piękna i radości może przynieść integracja kulturowa.

Serdecznie dziękuję całej mojej rodzinie w szczególności rodzicom **Małgorzacie i Przemysławowi**, którzy ogromnym nakładem pracy stworzyli fundament na którym mogę dalej rozwijać siebie. Mojemu mężowi **Konradowi** dziękuję za codzienne długie rozmowy, cierpliwość i stałe, codzienne, wzajemne rozpalanie chęci poznawania świata i zdobywania coraz to nowych kompetencji. Mojej najdroższej córeczce **Klarci** dziękuję za radość, którą swoją obecnością wprowadza do mojego życia. Podziękowania należą się również moim **dziadkom**, którzy odkąd pamiętam są przykładem pięknego życia na którym chcę się wzorować.

Dziękuję także wszystkim pozostałym przyjaciołom m. in. Ani i Dominice, a także znajomym i dalszej rodzinie których nie sposób tu wymienić, jednak jestem głęboko przekonana o tym że każda przeprowadzona z Wami rozmowa buduje i wzbogaca moje życie każdego dnia, jestem Wam za to bardzo wdzięczna!

Spis treści

WZKAZ SKRÓTÓW

Cp	– pierścień cyklopentadienylowy $[C_5H_5]^-$
Cp_c	– centroid pierścienia cyklopentadienylowego
Cp^*	– podstawiony pierścień cyklopentadienylowy
M	– centralny kation metalu
MCp_2	– metalocen
$FeCp_2$	– ferrocen
$NiCp_2$	– niklocen
$RuCp_2$	– rutenocen
$OsCp_2$	– osmocen
THF	– tetrahydrofuran
DAC	– komora diamentowa (*ang. Diamond Anvil Cell*)
SCXRD	– rentgenowska dyfraktometria monokrystaliczna (*ang. Single Crystal X-ray Diffraction*)
PXRD	– rentgenowska dyfraktometria proszkowa (*ang. Powder X-ray Diffraction*)
MEW	– mieszanina metanol: etanol: woda w stosunku 16:3:1 (obj.)
ΔE_p	– energia potencjalna bariery rotacji pierścienia cyklopentadienylowego
SOF	– cząstkowe obsadzenie atomu (*ang. Site Occupancy Factor*)
CSD	– krystalograficzna baza danych (*ang. Cambridge Structural Database*)
IR	– spektroskopia w podczerwieni (*ang. Infrared spectroscopy*)

STRESZCZENIE W JĘZYKU POLSKIM

Metaloceny to prototypowa grupa związków metaloorganicznych, których odkrycie zapoczątkowało intensywny rozwój tej dziedziny chemii. Niedawne publikacje nowych faz krystalicznych ferrocenu, modulowanej I″ i wysokociśnieniowej I′, skłoniły mnie do bardziej wnikliwej analizy również pozostałych prototypowych metalocenów. Przeprowadzone badania struktur niklocenu i ferrocenu, przy założeniu modelu niezależnych położeń pierścieni wskazały, że w izostrukturalnych fazach I tych związków, współistnieją konformacja naprzemianległa z konformacjami skręconymi. Ten, 'miękki model' wyjaśnia na podstawie danych strukturalnych obserwowane wcześniej eksperymentalnie dielektryczne właściwości ferrocenu, niezgodne z symetrią C_5 cząsteczek.

W wysokim ciśnieniu kryształy α-rutenocenu (α-$RuCp_2$, *Pnma*) i α-osmocenu (α-$OsCp_2$, grupa przestrzenna *Pnma*) ulegają przemianom fazowym ze zmianą symetrii do grupy przestrzennej *Pcmb* (β-$RuCp_2$) i *Pcab* (β-$OsCp_2$). Pomiary spektroskopii Ramana, dyfraktometryczne pomiary proszkowe i obserwacje wizualne kryształów świadczą o szerokich histerezach przemian fazowych, rozciągających się w zakresach 0.7-3.9 GPa ($RuCp_2$) i 0.3-3.6 GPa ($OsCp_2$). W wysokociśnieniowych polimorfach β preferencja do tworzenia krótkich oddziaływań CH···*M* (gdzie *M* = Ru, Os) jest wyższa niż do tworzenia oddziaływań CH···π, przeważających w fazie α. Dzięki dyfraktometrycznym pomiarom monokryształów $RuCp_2$ i $OsCp_2$ w ciśnieniu atmosferycznym i wysokich temperaturach, odpowiednio 395 K i 427 K, zaobserwowałam przemiany fazowe do izostrukturalnych faz γ o symetrii *Fmmm*. W wyniku tych przemian zerwane zostają wszystkie kontakty CH···*M*, a cząsteczki metalocenów stają się nieuporządkowane w konformacjach na przemian- i naprzeciwległej.

STRESZCZENIE W JĘZYKU ANGIELSKIM

(Summary in Englisch)

Metallocenes constitute a prototypic group of metalloorganic compounds. The discovery of ferrocene indicated the intensive development of metaloorganic chemistry. The recently revealed new high-pressure crystal phase I′ and modulated phase I″ of ferrocene convinced me to investigate also other prototypic metallocenes. The structural analysis of nickelocene and ferrocene, by applying the model of independent rotation of cyclopentadienyl rings to their isostructural phases I, shows that the staggered molecular conformation coexists with rotated conformations. Based on structural data, this 'soft model' explains the previously reported dielectric properties of ferrocene. These properties were inconsistent with the C_5 symmetry of ferrocene molecules.

The compression of α-ruthenocene (α-$RuCp_2$, space group *Pnma*) and α-osmocene (α-$OsCp_2$, *Pnma*) crystals lead to phase transitions, which change of crystal symmetry into space group *Pcmb* (β-$RuCp_2$) and *Pcab* (β-$OsCp_2$). The Raman spectra, diffractometric measurements on powder samples, and visual observations of single crystals revealed a wide hysteresis of the α – β phase transitions between 0.7-3.9 GPa ($RuCp_2$) and 0.3-3.6 GPa ($OsCp_2$). The high-pressure β polymorphs are stabilized by short contact CH···*M* (*M* = Ru, Os), whereas phase α is dominated by bonds CH···π. Diffractometric measurements on single crystals of $RuCp_2$ and $OsCp_2$ at ambient pressure and 395 K and 427 K respectively reveal the α to γ phase transitions. The high-temperature γ phases are isostructural, space group *Fmmm*. These phase transitions break all CH···*M* bonds, and the molecules become disordered in staggered and eclipsed conformations.

KOMENTARZ DO ARTYKUŁÓW

1. Wstęp o metalocenach

Odkrycie ferrocenu w 1951 roku[1] było przełomowym wydarzeniem, które zapoczątkowało dynamiczny rozwój chemii metaloorganicznej. W kolejnych latach otrzymano kolejne ważne metaloceny o prostej budowie, którą można opisać ogólnym wzorem MCp$_2$, gdzie symbol Cp oznacza pierścień cyklopentadienylowy, natomiast M dwudodatni kation metalu znajdujący się pomiędzy dwoma pierścieniami aromatycznymi (rysunek 1a). Do takich prototypowych metalocenów kanapkowych (*ang. sandwich compounds*) można zaliczyć wspomniany już wcześniej ferrocen (FeCp$_2$),[2] niklocen (NiCp$_2$),[3] rutenocen (RuCp$_2$),[4] osmocen (OsCp$_2$),[5] wanadocen (VCp$_2$),[6] chromocen (CrCp$_2$),[7] kobaltocen (CoCp$_2$),[8] oraz magnezocen (MgCp$_2$).[9] Z powyższych metalocenów jedynie FeCp$_2$, RuCp$_2$ oraz OsCp$_2$ spełniają regułę 18-nastu elektronów[10,11] natomiast pozostałe nie spełniają tej reguły (rysunek 1b). Wszystkie metaloceny spełniające regułę 18-tu elektronów są stabilne w atmosferze powietrza. Osmocen i rutenocen znane były wyłącznie w postaci kryształów o symetrii rombowej grupy przestrzennej *Pnma*, izostrukturalnych z niskotemperaturową fazą III ferrocenu. W strukturach tych atomy węgla tworzące pierścienie cyklopentadienylowe w cząsteczkach MCp$_2$ ułożone są względem siebie naprzeciwlegle (konformacja naprzeciwległa, *ang. eclipsed conformation*). Druga grupa metalocenów krystalizuje w jednoskośnej grupie przestrzennej $P2_1/n$. Struktury te są izostrukturalne z fazą I ferrocenu, a pierścienie Cp cząsteczek MCp$_2$ są nieuporządkowane. Ze względu na położenie cząsteczek w krysztale w pozycji specjalnej na centrum inwersji przez lata przyjmowano, że pierścienie Cp ułożone są względem siebie naprzemianlegle (konformacja naprzemianległa, *ang. staggered conformation*).

Ferrocen niewątpliwie był najdokładniej przebadanym metalocenem, oprócz struktur rombowej i jednoskośnej odkryto również niskotemperaturową trójskośnią fazę II o cząsteczkach w konformacji skręconej o około ±9°. Do niedawna uważano, że jest to jedyny metalocen, który w strukturach krystalicznych może przyjmować różne konformacje: naprzemianległą, naprzeciwległą i skręcone.

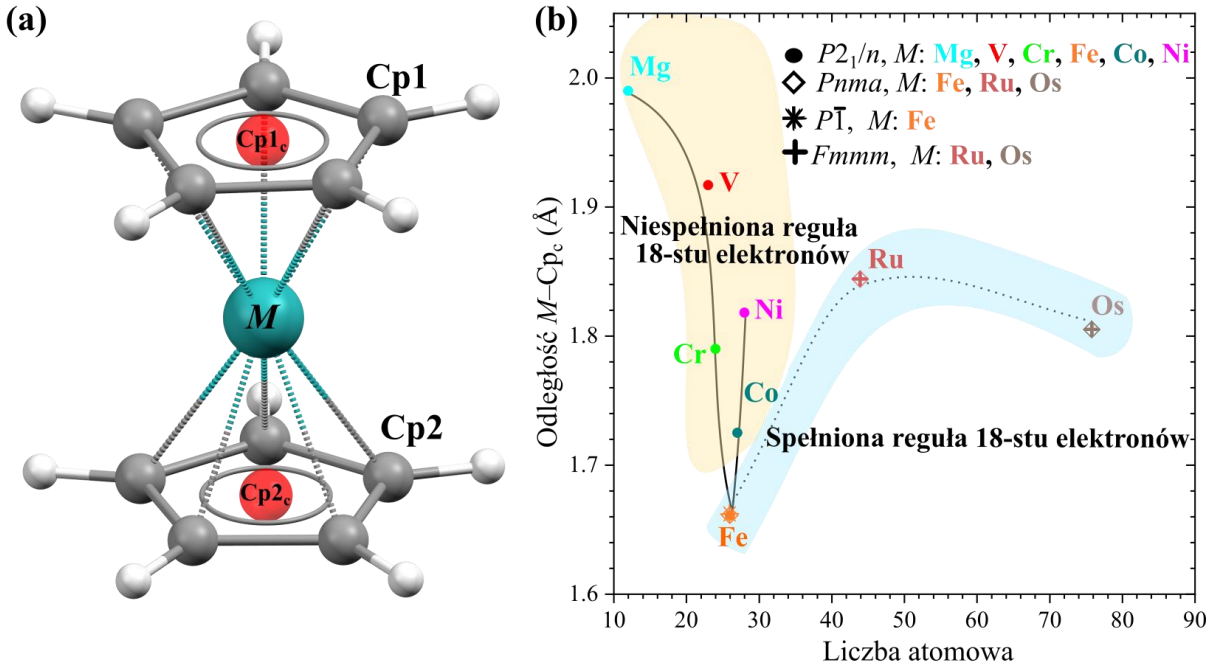

Rysunek 1. (a) Cząsteczka metalocenu z zaznaczonymi symbolami pierścieni cyklopentadienylowych i ich centroidów. (b) Odległość M-Cp_c w funcji liczby atomowej dla metalocenów $M^{2+}Cp_2$ o kącie θ, $Cp1_c$-M-$Cp2_c$ równym lub bliskim 180° w ciśnieniu 0.1 MPa. W legendzie zawarto informacje o grupie przestrzennej i kationie. Niebieskie i żółte tło obejmuje odpowiednio metaloceny spełniające i niespełniające reguły 18-elektronów.

1.1 Przełomowe odkrycie ferrocenu

W latach 1951-1982 odkryto trzy fazy ferrocenu. Jednoskośna faza I ferrocenu (I-$FeCp_2$) o symetrii grupy przestrzennej $P2_1/n$, która w 163.5 K przechodzi w fazę II (II-$FeCp_2$) o symetrii trójskośnej grupy przestrzennej $P\bar{1}$.[12] Wkrótce po odkryciu tej przemiany, opublikowana została nowa faza III ferrocenu (III-$FeCp_2$) o symetrii *Pnma*. Może ona zostać otrzymana w wyniku powolnej rekrystalizacji w temperaturze 98 K[13] i pozostaje stabilna do 250 K. Przez następne lata, gdy dynamicznie rozwijała się chemia metalocenów i świętowano rocznice odkrycia ferrocenu[14,15] stwierdzano izostrukturalność kolejnych związków i interpretowano ich właściwości odnosząc się do tych trzech faz I, II i III ferrocenu, a konformacje cząsteczek prototypowych metalocenów przedstawiano w wyidealizowanych symetriach D_{5d} i D_{5h} (S_{10})[16–18] wykluczających moment dipolowy. Dopiero w 2013 roku odkryto przemianę wysokociśnieniową ferrocenu w 3.24 GPa do jednoskośnej uporządkowanej fazy I′,

gdzie wszystkie cząsteczki rzeczywiście są centrosymetryczne (C_i), czyli posiadają symetrię przypisywaną fazie I. Izostrukturalna przemiana pomiędzy fazami I i I′ związana jest z porządkowaniem się pierścieni cyklopentadienylowych.[19] Badania kryształów ferrocenu w szerokim zakresie ciśnień do 40 GPa wskazały na stabilność fazy I′.[20] W wyniku tych badań powyżej 3.24 GPa odkryto nową fazę I′ ferrocenu, W 2023 roku w ciśnieniu atmosferycznym w niskiej temperaturze, pomiędzy 172.8 K i 163.5 K odkryto nową modulowaną fazę I″.[21]

1.2 Nieporządek w strukturach kryształów

Nieporządek pozycyjny zachodzi, gdy jeden atom lub grupa atomów zajmuje dwie lub więcej pozycji w uśrednionej strukturze kryształu. Wyróżnia się nieporządek statyczny, gdy atomy zajmują stałe, częściowo obsadzone pozycje w różnych komórkach elementarnych, i nieporządek dynamiczny, gdy atomy przeskakują między różnymi pozycjami.

Nieuporządkowanie pierścieni cyklopentadienylowych w cząsteczkach metalocenów najlepiej opisano dla modelowego związku, ferrocenu. Wyznaczono modele struktury fazy I (I-$FeCp_2$), w których pierścienie Cp znajdują się w dwóch[22] a nawet w trzech[23] położeniach. Nieporządek ten w ferrocenie ulega modulacji poniżej 172.8 K w fazie I″ i całkiem zanika poniżej 163.5 K po przemianie do trójskośnej fazy II;[12] można także wyeliminować nieporządek przez kompresję powyżej 3.24 GPa.[19] Badania dyfraktometryczne niklocenu pokazują, że nieporządek zanika w wyniku obniżenia temperatury poniżej 170 K,[24] zatem ma on charakter dynamiczny. Dotychczas nieuporządkowane położenia pierścieni cyklopentadienylowych stwierdzone były wyłącznie w jednoskośnych strukturach metalocenów. Jednak moje wysokotemperaturowe badania strukturalne rutenocenu i osmocenu (podrozdział 4.5) potwierdziły istnienie dla tych związków nieporządku w rombowej grupie przestrzennej *Fmmm*.

1.3 Konformacje metalocenów

Konformację metalocenów można zmierzyć kątem torsyjnym τ zawartym między najbliższymi atomami węgla przeciwnych pierścieni w cząsteczce, który wynosi 0° dla konformacji naprzeciwległej i 36° dla konformacji naprzemianległej (rysunek 2). Kąt τ dla konformacji skręconej (*ang. rotated*) przyjmuje wartości przejściowe pomiędzy konformacją naprzeciw- i naprzemianległą: w strukturze II ferrocenu kąt τ wynosi ±8° oraz ±9° dla dwóch niezależnych cząsteczek w asymetrycznej części komórki elementarnej oraz ich odbić w centrum inwersji. Do niedawna uważano również, że konformacja naprzemianległa pierścieni cyklopentadienylowych występuje jedynie w izostrukturalnych fazach metalocenów o symetrii jednoskośnej grupy przestrzennej $P2_1/n$. Moje badania w wysokiej temperaturze (podrozdział 4.5) ujawniły jednak istnienie konformacji naprzemianległych również w wysokotemperaturowych, rombowych strukturach rutenocenu i osmocenu.

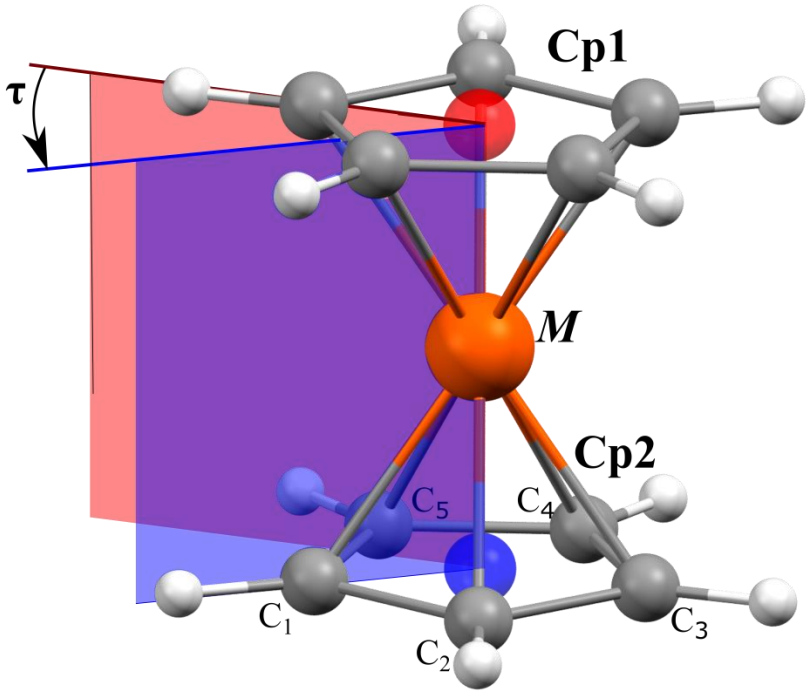

Rysunek 2. Kąt τ określający konformację pierścieni cyklopendtadienyclowych w cząsteczce metalocenu (τ = 0° konformacja naprzeciwległa, τ = 36° konformacja naprzemianległa).

1.4 Reguła 18-tu elektronów

Reguła 18-tu elektronów została pierwszy raz zaproponowana w 1921 roku przez Langumira,[10] w celu przewidywania stabilności kompleksów w chemii metaloorganicznej. Dotyczy ona jednak wyłącznie kompleksów metali przejściowych, które posiadają 9 orbitali walencyjnych (pięć orbitali *d* na powłoce *n*-1); trzy orbitale *p* na powłoce *n* i jeden orbital *s* na powłoce *n*), mogących pomieścić 18 elektronów. Te orbitale mogą połączyć się z orbitalami ligandów, w skutek czego powstają orbitale molekularne. Reguła 18-stu elektronów nie jest jednak sztywna i znane są przypadki, dla których atom centralny kompleksu nie posiada konfiguracji gazu szlachetnego. Wiele takich przykładów zostało już opisanych, np. nisko- spinowe kwadratowe kompleksy d^8 – $16e^-$, $V(CO)_6$ – $17e^-$, $CrCl_3(THF)_3$ – $15e^-$.[25–27] Ich cechą charakterystyczną jest wyższa reaktywność niż kompleksów 18 elektronowych. Wśród wyjątków dość liczną grupę stanowią metaloceny, dla których znane są kompleksy o niższej liczbie elektronów: VCp_2 – $15e^-$, $CrCp_2$ – $16\ e^-$. Wśród metalocenów spotkać można również przykłady kompleksów o wyższej liczbie elektronów niż 18: $CoCp_2$ – $19e^-$ i $NiCp_2$ – $20e^-$. Związki kompleksowe o liczbie elektronów wyższej niż 18 są jednak rzadko spotykane. Nadmiarowe elektrony w tego typu cząsteczkach znajdują się na molekularnym orbitalu antywiążącym. Kompleksy z większą niż 18 liczbą elektronów walencyjnych są, podobnie jak kompleksy z mniejszą niż 18 liczbą elektronów chętnie wchodzą w reakcje chemiczne.[28,29]

1.5 Oddziaływania M···HC

Wiązania węgiel-wodór od lat są przedstawiane w literaturze jako silne i słabo aktywne w reakcjach chemicznych.[30,31] Odkrycie struktur metaloorganicznych, w których skład wchodziły metale przejściowe, pokazało, że nawet słabo aktywne chemicznie grupy alkilowe mogą być zaangażowane w tworzenie oddziaływań z centralnym atomem metalu.[32] Wkrótce po rozwinięciu się metod analizy strukturalnej wyłoniono grupę związków, dla których odległość *M*···H była bardzo krótka (1.8-2.3 Å), a kąt *C-H*···*M* nie przekraczał 140°.[33–35] Takie oddziaływania często występują w strukturach kompleksów, dla których liczba elektronów jest mniejsza niż 18. Krótkie kontakty atomu metalu z wiązaniem C-H uznano za

oddziaływanie 3-centrowe, 2-elektronowe i nazwano je agostycznym.[36] Odkryto także grupę struktur w których odległość między atomem wodoru i metalu również była krótsza niż suma promieni van der Waalsa, lecz przekraczała wartość 2.3 Å, którą uznano za graniczną przy opisie oddziaływań agostycznych. Wiązania takie nazwano anagostycznymi (czyli nie-agostycznymi). Głównym aspektem różnicującym oddziaływania agostyczne i anagostyczne jest długość kontaktów, zauważono jednak, że w przypadku oddziaływań anagostycznych kąt *C-H···M* zawierał się między 110-170°.[33] Mniej rozwarty kąt *C-H···M* charakterystyczny dla oddziaływań agostycznych, jest związany z powinowactwem metalu do pary elektronowej tworzącej wiązanie C-H. Z kolei większy kąt *C-H···M*, jest charakterystyczny dla oddziaływań anagostycznych ze względu na powinowactwo metalu do atomu wodoru, na którym występuje cząstkowy ładunek dodatni. Oddziaływania anagostyczne tworzą kompleksy metali, dla których spełniona jest reguła 18-elektronów. Zarówno na podstawie rozważań teoretycznych Orlova i Scheinera[37] jak i wyników badań spektroskopowych IR oraz dyfraktometrycznych SCXRD,[38] którym poddane zostały pochodne metalocenów zawierające ugrupowania $M\mathrm{Cp}^{*}_{2}$ (gdzie *M*= Fe, Ru, Os; gwiazdka oznacza podstawienie pierścienia Cp), można wnioskować, że metale przejściowe są akceptorami protonu, w rozumieniu podobnym do tworzenia wiązań wodorowych w cząsteczkach organicznych.[39,40] Wolna para elektronowa na orbitalu *d* metalu przejściowego odpowiada wolnej parze elektronowej zlokalizowanej na orbitalu *sp*. Oddziaływanie tego typu, poza parą elektronową tworzącą wiązanie C-H, zaangażuje również wolną parę elektronową zlokalizowaną na orbitalu *d* metalu przejściowego. Wiązania te są zatem wiązaniami 3-centrowymi, 4-elektronowymi. Zostały one nazwane wiązaniami anagostycznymi w celu ich wyraźnego rozróżnienia od wiązań agostycznych.[41] Oddziaływania *M*···H-C występujące w strukturach III-$FeCp_2$, α- i β-$RuCp_2$ oraz α- i β-$OsCp_2$ są oddziaływaniami anagostycznymi.

1.6 Efekty wysokociśnieniowe

Ogólnie przyjmuje się, że efektem działania wysokiego ciśnienia na strukturę ciał stałych jest skrócenie odległości między atomami.[42–44] Kompresja odległości międzyatomowych może prowadzić do powstania nowych oddziaływań,[45–47] a nawet

wiązań chemicznych.[48] Zmniejszenie odległości międzycząsteczkowych wymusza często optymalizację kątów między atomami.[49–52] Zmiany kątów i odległości zarówno w cząsteczce, jak i w jej najbliższym otoczeniu mogą doprowadzić do przemiany fazowej, dzięki której cząsteczki przyjmą mniej naprężone położenia niż przed przemianą.[53–55] Bliższe położenia cząsteczek powodują powstawanie zawad sterycznych ograniczających ruch cząsteczek lub grup atomów, co w przypadku nieuporządkowanych struktur może prowadzić do ich uporządkowania.[56–58] Wysokie ciśnienie może również zmienić konformację. cząsteczek oraz prowadzić do ich reakcji chemicznych.[59,60] Najczęściej skracanie odległości międzycząsteczkowych prowadzi do skracania wszystkich parametrów komórki elementarnej. W niektórych przypadkach, w wysokim ciśnieniu następuje wydłużanie jednego parametru – jest to tzw. negatywna ściśliwość liniowa,[61,62] lub wydłużenie dwóch parametrów określane jako negatywna ściśliwość powierzchniowa.[63,64] Efekty te są jednak kompensowane przez silne zmiany pozostałych parametrów, tak że podstawowy warunek termodynamiki, efekt zmniejszania objętości próbki przy wzroście ciśnienia, jest zachowany.

2. Cel pracy

Głównym celem mojej rozprawy doktorskiej było zrozumienie czynników decydujących o konformacji cząsteczek metalocenów i uzupełnienie wiedzy o strukturach krystalicznych tych związków. Poszukiwałam związków pomiędzy fazą krystaliczną (odmianą polimorficzną metalocenu), rodzajem metalu centralnego w kompleksie, konformacją pierścieni cyklopentadienylowych oraz warunkami termodynamicznymi. Kolejnym celem była analiza oddziaływań w nowo otrzymanych fazach metalocenów oraz wyjaśnienie przyczyn obserwowanych przemian w warunkach wysokiego ciśnienia lub wysokiej temperatury.

Wyniki badań wykonanych w ramach mojej rozprawy doktorskiej zostały opublikowane w serii 5 artykułów naukowych (Załączniki 1-5):

Artykuł 1 Lattice-strain Coupled to Molecular Conformation and Disorder in Compressed Nickelocene
I. Moszczyńska, A. Katrusiak
The Journal of Physical Chemistry C 125 (28), 15670-15675, **2021**
DOI: 10.1021/acs.jpcc.1c04204

Artykuł 2 Pressure-Tuned Conformers and Their Populations in Ferrocene
I. Moszczyńska, D. Paliwoda, A. Katrusiak
The Journal of Physical Chemistry C 128 (45), 19392-19397, **2024**
DOI: 10.1021/acs.jpcc.4c05399

Artykuł 3 Competition between Hydrogen and Anagostic Bonds in Ruthenocene Phases under High Pressure
I. Moszczyńska, A. Katrusiak
The Journal of Physical Chemistry C 126 (10), 5028-5035, **2022**
DOI: 10.1021/acs.jpcc.1c10249

Artykuł 4 Giant Deformation between Osmocene Phases Induced by Anagostic Bonds Promoted under High Pressure
I. Moszczyńska, I. Gulaczyk, A. Katrusiak
The Journal of Physical Chemistry C 127 (38), 19250-19257, **2023**
DOI: 10.1021/acs.jpcc.3c04579

Artykuł 5 New Osmocene and Ruthenocene Phases Reveal the Common Conformational Bahavior Regulated by Anagostic Bonds in Prototypical Matallocenes
I. Moszczyńska, M. Szafrański, A. Katrusiak
The Journal of Physical Chemistry Letters, **2025**
DOI: 10.1021/acs.jpclett.5c00686

3. Metody badawcze

Wszystkie artykuły składające się na moją rozprawę doktorską zawierają część eksperymentalną, w której przedstawiłam szczegóły metodologiczne przeprowadzonych badań. W tej części mojej rozprawy zwięźle przedstawię najważniejsze techniki przeze mnie stosowane.

3.1 Kompresja i rekrystalizacja w komorze diamentowej

Badania wysokociśnieniowe prowadziłam z wykorzystaniem komory diamentowej typu Merrilla-Bassetta.[15] Komora ta zbudowana jest z dwóch przeciwległych kowadeł diamentowych osadzonych w podtrzymujących dyskach. Pomiędzy diamentami umieszczona jest uszczelka wykonana z twardej blachy o grubości ok 0.2 mm, w której znajduje się otwór stanowiący komorę ciśnieniową. Uszczelka zabezpiecza też kolety diamentów przed kontaktem i zniszczeniem. W otworze o średnicy 0.3-0.4 mm znajduje się badana próbka w otoczeniu cieczy hydrostatycznej. (rysunek 3a). Wysokie ciśnienie powstaje przy ściskaniu cieczy przez dokręcanie trzech śrub (rysunek 3b) i przenoszone jest z dużych powierzchni koron diamentów na małe powierzchnie ich koletów. Zadaniem cieczy jest przeniesienie ciśnienia z koletów diamentów do badanej próbki i zapewnienie warunków hydrostatycznych. Pomiary ciśnienia w komorze diamentowej wykonywałam metodą fluorescencji rubinu.[65] Rubin, który jest wskaźnikiem ciśnienia, umieszczany jest wraz z próbką w komorze pomiędzy diamentami. Pomiar przesunięcia linii R1 i R2 fluorescencji rubinu wykonywałam przy wykorzystaniu spektrofluorymetru Photon Control.[66] Tak przygotowaną komorę umieszczałam na główce goniometrycznej, umożliwiającej mocowanie na dyfraktometrze rentgenowskim, celem wykonania strukturalnego pomiaru dyfrakcyjnego. (rysunek 3c).

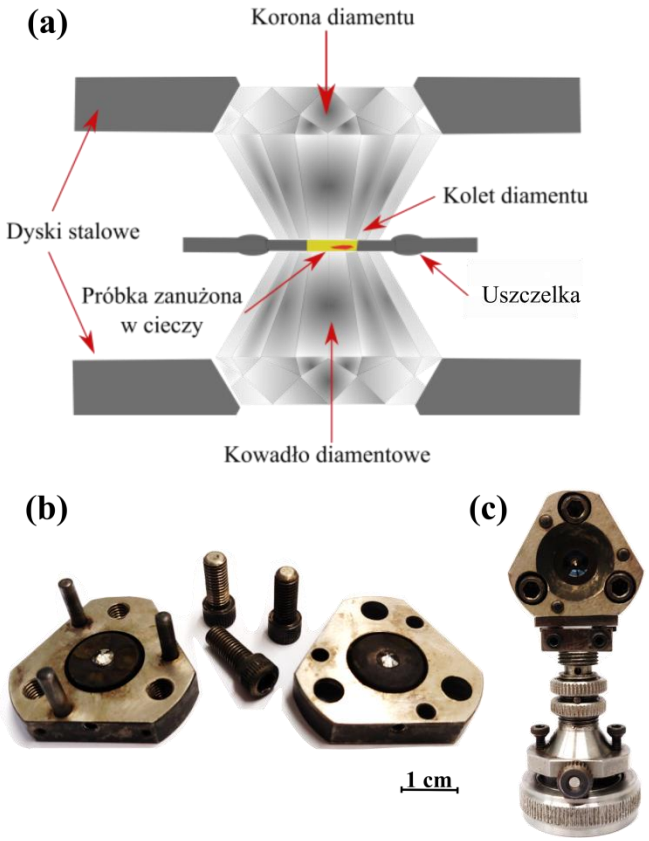

Rysunek 3. Komora diamentowa: (a) schematyczny rysunek przekroju wnętrza komory, (b) komora otwarta bez uszczelki, (c) komora zamknięta i osadzona na główce goniometrycznej. Przedstawiona skala dotyczy wyłącznie rysunku (b).

Próbki proszkowe ściskałam izotermicznie w cieczy hydrostatycznej MEW (mieszanina metanol:etanol:woda w stosunku objętościowym 16:3:1).[67] Monokryształy niklocenu ściskałam izotermicznie w oleju Daphne[68] i mieszaninie metanol:etanol (w stosunku objętościowym 4:1)[67] a krystały osmocenu i rutenocenu w mieszaninie MEW. Natomiast rekrystalizacje w warunkach wysokiego ciśnienia prowadziłam w dobrym rozpuszczalniku metalocenów – tetrahydrofuranie (THF).

Otrzymanie wysokociśnieniowych faz rutenocenu i osmocenu było możliwe dzięki zastosowaniu zarodkowanej rekrystalizacji w komorze. Metoda ta polegała na przekroczeniu limitu hydrostatyczności THF (2.24 GPa)[69] do około 4 GPa (tzn. powyżej ciśnienia przemiany fazowej), następnie dekompresji próbki do około 1 GPa i ogrzewaniu jej w celu rozpuszczenia wszystkich fragmentów kryształu próbki poza jednym, który stawał się zarodkiem krystalizacji dla fazy wysokociśnieniowej.

3.2 Wysokociśnieniowa rentgenowska dyfraktometria monokrystaliczna

Badania strukturalne wykonane były metodą monokrystalicznej dyfrakcji rentgenowskiej. Stosowałam procedury centrowania komory diamentowej na dyfraktometrze metodą cienia uszczelki i pomiaru dyfraktometrycznego przy optymalnym pozycjonowaniu komory.[70] Wszystkie wysokociśnieniowe pomiary strukturalne wykonałam na czterokołowych dyfraktometrach KUMA KM-4 CCD i Xcalibur CCD z wykorzystaniem promieniowania rentgenowskiego $MoK_{\bar{\alpha}}$ (λ=0.71073 Å). Poprawki na absorpcję próbki i komory bazujące na wyznaczeniu ścian kryształów oraz obrysowaniu uszczelki zostały dodane przy pomocy funkcji zaimplementowanych w programie CrysalisPro[71] podczas wstępnej obróbki danych pomiarowych. Do wyznaczenia i udokładnienia struktury wykorzystałam program Olex2,[72] który wykorzystuje programy z pakietu Shelx.[73]

3.3 Spektroskopia Ramana

Pomiary Ramana przeprowadziłam na próbkach polikrystalicznych w komorze diamentowej zaopatrzonej w syntetyczne diamenty klasy IIA o niskiej fluorescencji. Eksperymenty wykonałam przy użyciu promieniowania laserowego o długości fali wzbudzenia 785 nm i wielokanałowego detektora Photonic.

3.4 Obliczenia potencjału elektrostatycznego na powierzchni cząsteczek

Obliczenia potencjału elektrostatycznego na powierzchni cząsteczek różnych metalocenów dla konformacji naprzemianległej i naprzeciwległej wykonałam w programie Gaussian 16W metodą DFT. Do obliczeń zastosowano bazy: double-ζ LANL2DZ dla osmu, rutenu i żelaza, SDD powiązaną z pseudopotencjałem dla atomów węgla i D95 dla atomów wodoru.[74–76]

3.5 Wysokotemperaturowa dyfraktometria rentgenowska

Z uwagi na łatwość sublimacji metalocenów, wysokotemperaturowe pomiary rentgenowskie wykonywałam dla próbki zamkniętej w kapilarze. Umieszczałam w niej duży monokryształ oraz bagietkę szklaną, która z jednej strony dotykała

kryształu, na drugim końcu natomiast zatopiona była wraz z kapilarą. Bagietka została wykorzystana w celu wypełnienia przestrzeni kapilary, co miało doprowadzić do szybkiego osiągnięcia nasycenia par sublimującego kryształu i spowolnić jego utratę masy. Pomiary monokrystaliczne i proszkowe zostały wykonane na dyfraktometrach Xcalibur Atlas oraz Bruker D8 Quest z wykorzystaniem odpowiednio promieniowania rentgenowskiego MoKα i CuK_{α}. Kapilary ogrzewane były przy pomocy przystawek temperaturowych Oxford Cryostream Plus.

3.6 Skaningowa kalorymetria różnicowa

Pomiary kalorymetryczne zostały wykonane przy użyciu kalorymetru Q20000 dla próbki rutenocenu w zakresie temperatur od 100 K do 440 K i próbki osmocenu w zakresie temperatur od 100 K do 470 K. Zastosowana szybkość chłodzenia i ogrzewania próbki to 10 K/min. Do kalibracji urządzenia użyto wzorca indu, natomiast do skalibrowania ciepła właściwego użyto szafiru syntetycznego. Zmiana entropii wyliczona została z równania 1,

$$\Delta S = \int_A^B \frac{Cp(T) - Cp^0(T)}{T}\, dT \qquad \textbf{\textit{Równanie 1}}$$

w którym $Cp^0(T)$ jest ewolucją temperatury bazowej.

3.7 Krystalograficzna baza danych

Przy przeszukiwaniu bazy CSD (Cambridge Structural Database wersja 5.43/ 2021) użyłam zapytania zawierającego dwa dowolnie podstawione pierścienie cyklopentadienylowe połączone z atomem metalu przy pomocy wiązań o niezdefiniowanym typie. Ładunek na atomie centralnym został zdefiniowany dla każdego przeszukiwania bazy jako obojętny lub dodatni zależnie od konfiguracji elektronowej atomu centralnego. Kąt zgięcia cząsteczki θ zdefiniowany jako kąt zawarty między centroidem jednego pierścienia, jonem centralnym i centroidem drugiego pierścienia, nie był ograniczony (mógł się zawierać między 0 a 180°). Zdefiniowany został także kąt torsyjny τ określający konformację (Podrozdział 1.3, rysunek 2), kąt ten miał się zawierać między -36 a 36°. W rozprawie przedstawiłam wartość bezwzględną kąta τ (|τ|), ponieważ, dla analizy konformacji naprzemian-

i naprzeciwległej pierścieni znak kąta był nieznaczący. Ze zbioru wyników wyszukiwania usunięto struktury w których liczba koordynacyjna atomu centralnego była inna niż 10 oraz powtarzające się struktury metalocenów MCp$_2$. Pozostawienie wszystkich struktur metalocenów MCp$_2$ mogłoby zaburzyć statystykę otrzymanych wyników – na przykład liczba zdeponowanych struktur tylko dla ferrocenu wynosi 87. Do struktur o konformacji naprzeciwległej pierścieni cyklopentadienylowych zaklasyfikowałam te, dla których kąt torsyjny zawierał się w przedziale $0 \leq |\tau| \leq 1$, natomiast do struktur o konformacji naprzemianległej pierścieni te, dla których wartość kąta spełniała warunek $35 \leq |\tau| \leq 36$.

4. Wyniki i dyskusja

4.1 Sprzężenie naprężenia sieci z konformacją i nieporządkiem w niklocenie

W artykule 1 przedstawiłam moje badania kryształów niklocenu. W ciśnieniu atmosferycznym (0.1 MPa) i temperaturze otoczenia 296 K, NiCp$_2$ krystalizuje w jednoskośnej grupie przestrzennej $P2_1/n$ (faza I). Faza I jest izostrukturalna z fazą I ferrocenu i cząsteczki są również nieuporządkowane konformacyjnie. Przy obniżaniu temperatury poniżej 170 K konformacja cząsteczek niklocenu ulega stopniowemu porządkowaniu i pozostaje stabilna co najmniej do 90 K. Stwierdziłam, że w temperaturze 296 K wzrost ciśnienia powyżej 1.3 GPa również prowadzi do całkowitego uporządkowania struktury, w wyniku czego otrzymałam fazę I′, izostrukturalną z wysokociśnieniową fazą I′ ferrocenu. Podobnie jak obserwowano to w ferrocenie, zmianom nieuporządkowania konformacyjnego niklocenu towarzyszą anomalna ściśliwość i rozszerzalność termiczna kryształów. Następnie przeanalizowałam też zmiany rozkładu konformacji nieuporządkowanych cząsteczek fazy I prowadzące do uporządkowanej fazy I′.

Zależność pomiędzy kątami opisującymi nieporządek cząsteczki niklocenu i jej konformacje w fazie I przedstawia rysunek 4. Kąt φ, zawarty pomiędzy (atomem C_{1Cp1A}) – (centroidem Cp_c1) – (atomem C_{1Cp1B}) jest związany z kątem torsyjnym τ zależnością: $\tau=36°- \varphi$ (podrozdział 1.3, strona 4). Na podstawie moich badań

stwierdziłam znaczne zmiany kąta φ w strukturze niklocenu w zależności od ciśnienia i temperatury (rysunek 5).

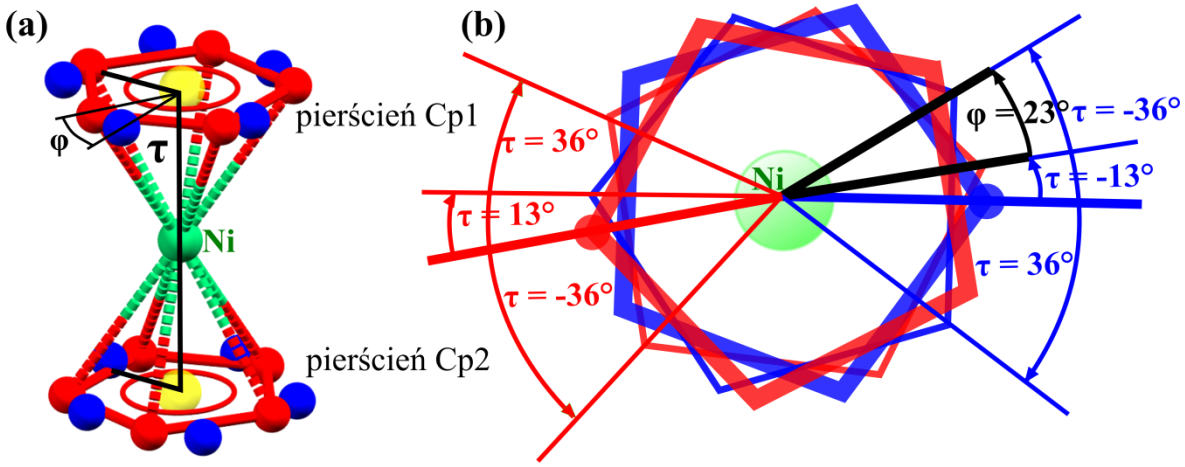

Rysunek 4. (a) Cząsteczka niklocenu fazy I (atomy wodoru zostały pominięte dla zwiększenia przejrzystości rysunku). Częściowo obsadzone pozycje A i B oznaczyłam kolorami niebieskim (bez wiązań) i czerwonym (z wiązaniami). (b) Cząsteczka niklocenu (0.1 MPa, 296 K) przedstawiona w rzucie wzdłuż pseudo 5-krotnej osi symetrii cząsteczki z zaznaczonym kątem torsyjnym τ pomiędzy pierścieniami (grubsze linie oznaczają bliższy, a cienkie dalszy pierścień).

Dotychczas nieporządek w strukturach metalocenów krystalizujących w grupie przestrzennej $P2_1/n$ opisywany był modelem, w którym cząsteczki występują wyłączenie w konformacji naprzemianległej. Wynikało to z położenia cząsteczek na centrum inwersji, ale było równoważne z powiązaniem nieporządku ze sztywnymi rotacjami całej cząsteczki.[23] W **artukule 1** wprowadziłam nowe podejście do nieporządku, dopuszczając niezależne rotacje pierścieni Cp1 i Cp2, co prowadzi do współistnienia różnych konformacji cząsteczek. Korelacja kąta φ (rysunek 5) oraz cząstkowych obsadzeń atomów (rysunek 6) dostarcza informacji o konformacjach występujących w strukturze w zależności od ciśnienia i temperatury. Kąt φ może zmieniać się od 0 do 72°. Dla wartości granicznych jest on powiązany z występowaniem struktury uporządkowanej w konformacji naprzemianległej (100% konformacji staggered). Gdy kąt φ wynosi 36°, struktura jest nieuporządkowana i składają się na nią konformery naprzemian- i naprzeciwległe, których udział procentowy wyliczyć można z równań 2 i 3**.** Dla pozostałych wartości kąta φ struktura jest nieuporządkowana i składa się z konformerów naprzemianległego i skręconych (równanie 3).

$$\%\ udział\ konformeru\ staggered = (SOF_A \times SOF_A + SOF_B \times SOF_B) \times 100\%$$

Równanie 2

$$\%\ udział\ konformeru\ eclipsed/rotated = SOF_A \times SOF_B \times 2 \times 100\%$$

Równanie 3

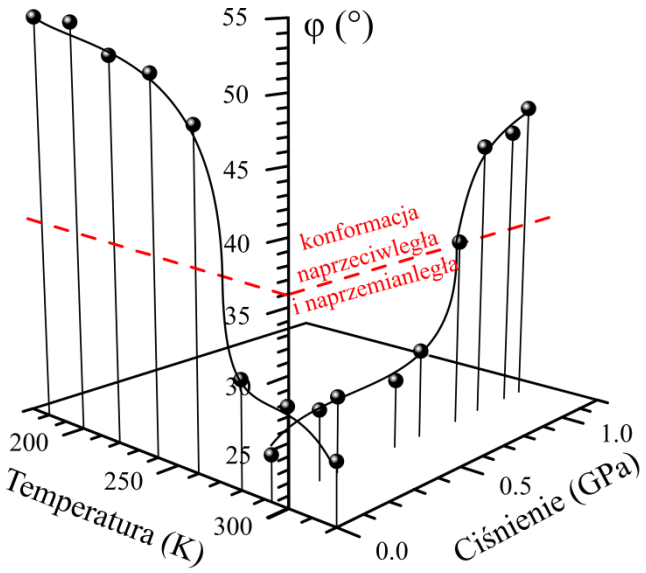

Rysunek 5. Zmierzona zależność kąta φ od ciśnienia i temperatury. Czerwona pozioma linia odpowiada wartości kąta φ równej 36°, gdy cząsteczka składa się z konformerów naprzemian- i naprzeciwległych.

Ciśnienie i temperatura, w których współistnieją konformacje naprzemian- i naprzeciwległa są również punktami maksymalizacji różnicy obsadzeń położeń A i B (rysunek 6).

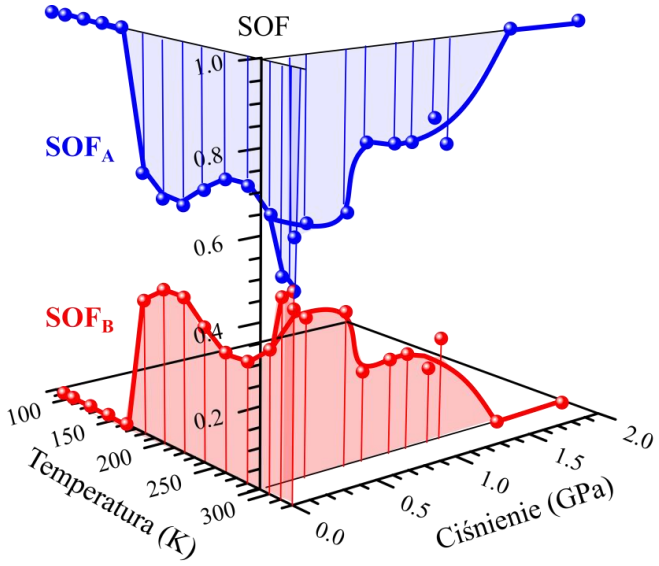

Rysunek 6. Współczynniki obsadzenia położeń A (SOF_A) i B (SOF_B) pierścieni cyklopentadienylowych niklocenu wykreślone w funkcji ciśnienia i temperatury.

W podsumowaniu, **Artykułu 1** przedstawiłam populacyjny model nieporządku konformacyjnego w fazie I niklocenu, gdzie populacje konformacji można wyznaczyć rozplatając (dekonwolując) funkcje opisujące nieporządek.

4.2 Ciśnieniowe zmiany konformacji w ferocenie

W **Artykule 2** omówiłam wyzwolone ciśnieniem zmiany konformacyjne cząsteczek ferrocenu w kryształach fazy I. Przedstawiłam model nieporządku fazy I zakładając niezależne rotacje pierścieni Cp1 i Cp2, co prowadzi do współistnienia konformerów skręconych oraz konformeru naprzemianległego.

Podobnie jak w przypadku niklocenu, w **Artykule 2** szczegółowo opisałam wywołane ciśnieniem zmiany parametrów takich jak: obsadzenie (współczynnik SOF), kąt nieporządku φ i skorelowany z nim kąt torsyjny τ. Okazało się, podobnie jak dla niklocenu, że również w fazie I ferrocenu największa różnica obsadzeń pozycji A i B pierścieni (SOF_A i SOF_B) występuje dla wartości kąta φ=36° (2.2 GPa, rysunek 7).

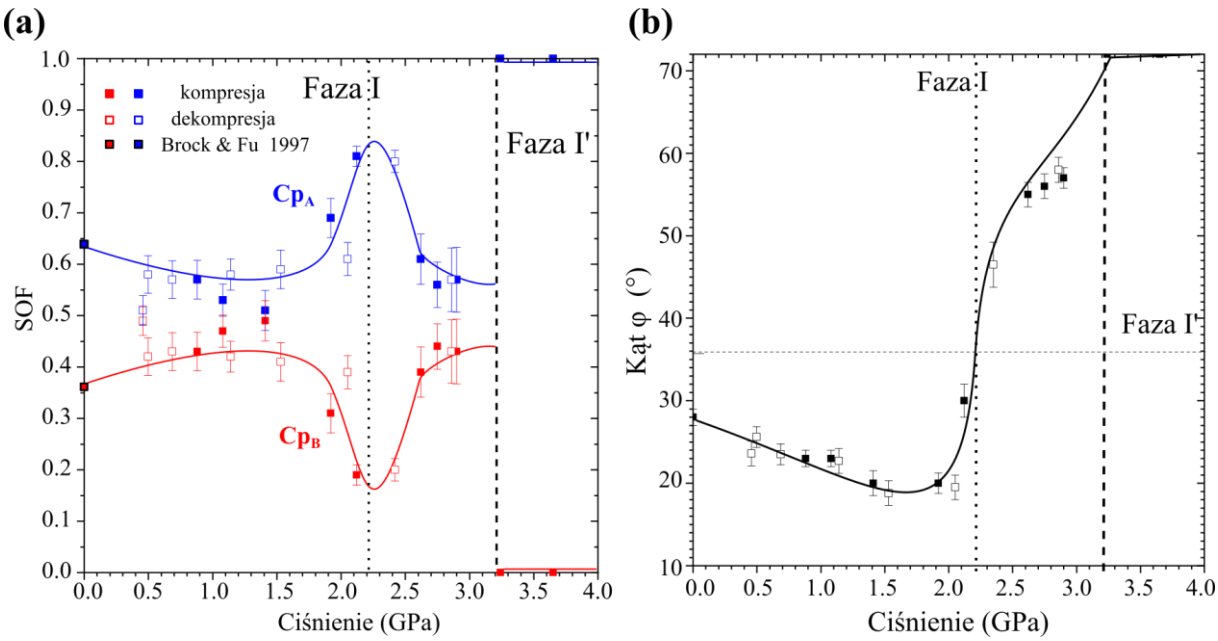

Rysunek 7. Zależność ciśnieniowa (a) współczynników SOF obsadzenia pozycji A i B pierścieni Cp i (b) kąta φ od ciśnienia dla fazy I ferrocenu.

Zaproponowany przeze mnie model nieporządku jest zastosowaniem wyników badań ferrocenu metodami nieelastycznego rozpraszania neutronów i spektroskopii Ramana do analizy konformacyjnej nieuporządkowanych cząsteczek. Model ten wyjaśnia dotychczas niespójną strukturalnie dielektryczną odpowiedź ferrocenu.[77,78] Uzyskane wyniki wskazują na występowanie momentów dipolowych cząsteczek ferrocenu, co nie było zgodne z, zakładaną w modelu sztywnych cząsteczek symetrią D_{5i}. Natomiast model giętki niezależnych pierścieni Cp1 i Cp2 dopuszcza przesunięcie pierścieni (zgięcie cząsteczki mierzone kątem θ, Cp_{c1}-Fe-Cp_{c2}), co generuje moment dipolowy.[77,78]

4.3 Współzawodnictwo wiązań CH···π i CH···M w rutenocenie

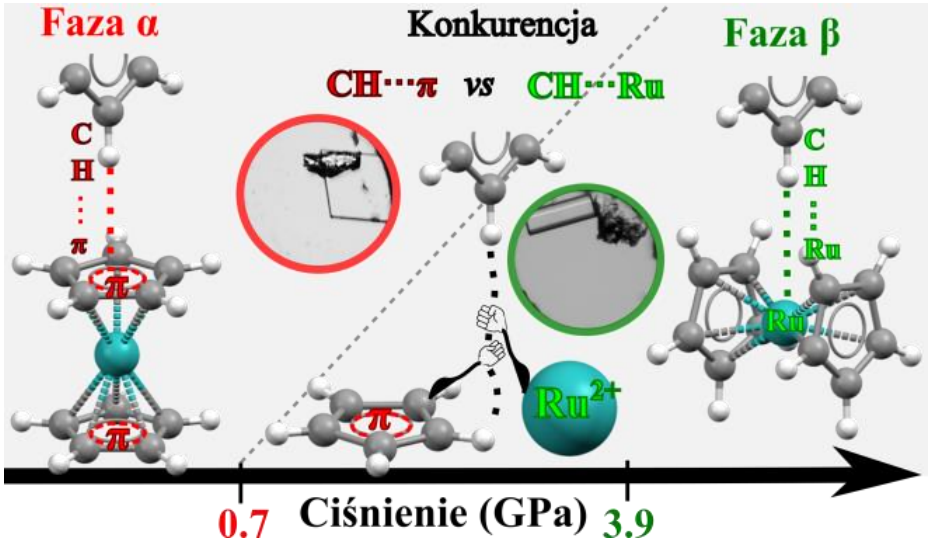

Rysunek 8. Graficzne przedstawienie najważniejszych aspektów **Artykułu 3**.

Dotychczas rutenocen i osmocen traktowano jako modelowe metaloceny przyjmujące w ciele stałym jedynie energetycznie uprzywilejowane konformacje naprzeciwległe. Założenie to opierano na wynikach badań w warunkach normalnych i niskich temperaturach. Rutenocen. α-$RuCp_2$ krystalizuje w rombowej grupie przestrzennej *Pnma*, a cząsteczki przyjmują konformację naprzeciwległą. Na podstawie pomiarów rentgenowskich na próbkach proszkowych, powyżej 3.9 GPa zaobserwowałam nowe refleksy (rysunek 9), które wskazały na przemianę do nowej fazy β. Podczas dekompresji poniżej 0.7 GPa refleksy pochodzące od fazy β zanikają. Z uwagi na destrukcyjny dla kryształu charakter przemiany musiałam przeprowadzić zarodkową rekrystalizacje *in situ* fazy β w komorze DAC. Dla otrzymanych tak monokryształów przeprowadziłam pomiary dyfraktometryczne i wyznaczyłam ich symetrię grupy przestrzennej *Pcmb* oraz strukturę.

Przemiana pomiędzy fazami α i ß wykazuje bardzo szeroką histerezę pomiędzy 0.7 i 3.9 GPa. Dzięki temu mogłam porównać obie fazy w tych samych warunkach ciśnienia i temperatury, dzięki kokrystalizacja dwóch faz w komorze diamentowej. Kryształy faz α i β można łatwo rozpoznać, gdyż znacząco różnią się one morfologią (rysunek 10).

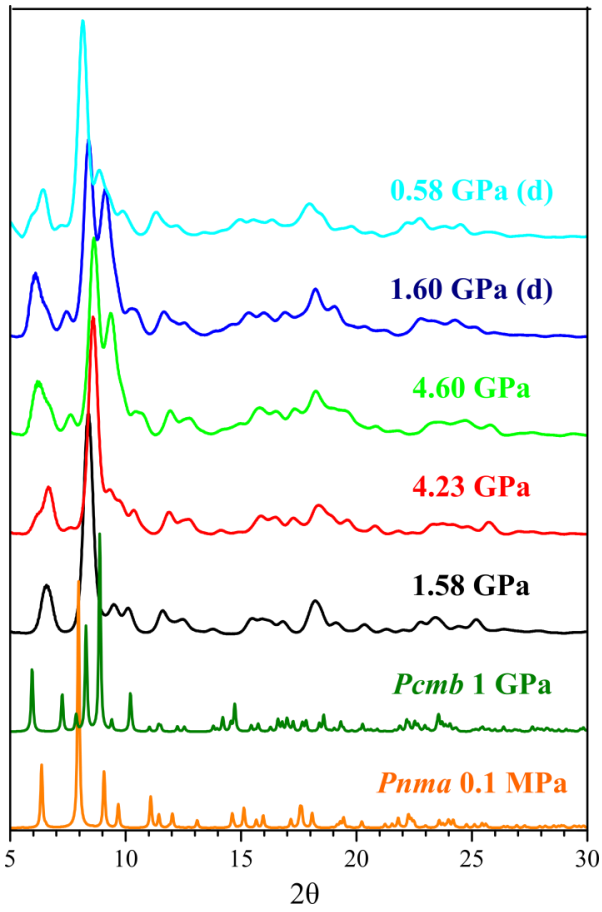

Rysunek 9. Dyfraktogramy proszkowe zarejestrowane dla próbek rutenocenu ściśniętych w komorze DAC w 1.58 GPa, 4.23 GPa, 4.60 GPa a następnie poddanych dekompresji do 1.60 GPa i 0.58 GPa. Wygenerowane w programie Mercury[79] na postawie pomiarów monokrystalicznych dyfraktogramy proszkowe fazy α (pomarańczowy) i fazy β (ciemnozielony) przedstawiłam dla porównania na dole zestawienia.

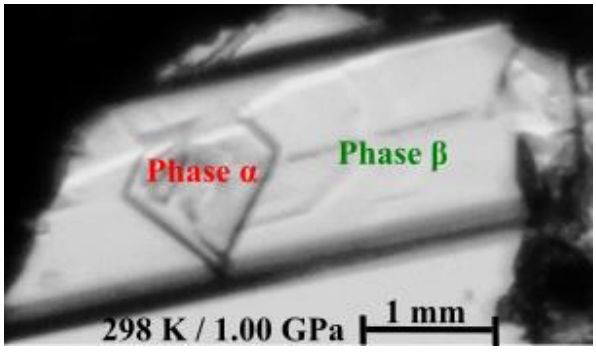

Rysunek 10. Kryształy $RuCp_2$ faz α (czerwony opis) i β (zielony) powstałe w trakcie zarodkowej krystalizacji w komorze diamentowej w ciśnieniu 1.00 GPa.

Fazy α i β wykazują szereg podobieństw: pierścienie cyklopentadienylowe ułożone są naprzeciwlegle, symetrię cząsteczek w krysztale opisuje grupa punktowa o symbolu

Schoenfliesa C_s, ale przybliżają one symetrię grupy D_{5h} (S_{10}), atomy rutenu znajdują się w pozycji szczególnej, na płaszczyźnie zwierciadlanej *m*, a pierścienie Cp są do tej płaszczyzny prostopadłe (rysunek 11).

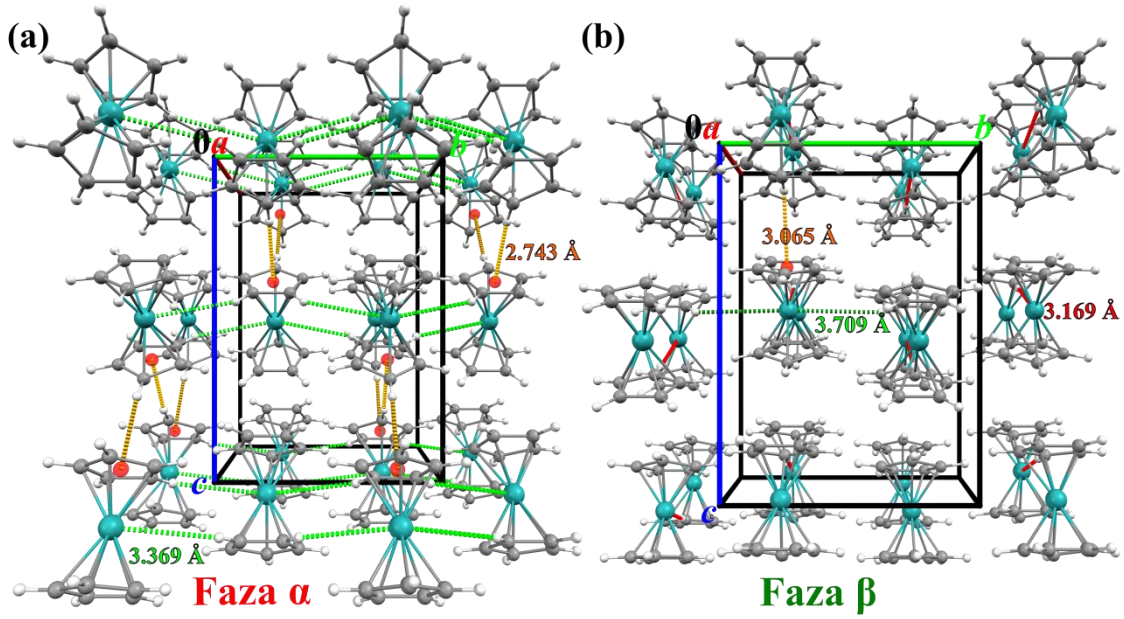

Rysunek 11. Autostereogramy[80] rutenocenu: (a) faza α w 0.13 GPa i (b) faza β w 1.00 GPa. Oba rzuty wzdłuż kierunku [100] przedstawiłam w tej samej skali. Kolor pomarańczowy oznacza kontakty CH···π, a zielony i czerwony kontakty CH···Ru.

Podobieństwa strukturalne faz α i β skutkują podobieństwami w ściśliwości liniowej. Najmniejsza ściśliwość liniowa obserwowana jest wzdłuż kierunku [z], co jest związane z położeniem cząsteczek rutenocenu, których pseudo 5-krotna oś symetrii odchylona jest od osi [z] o kąt ψ_α równy około 30°. Kąt ψ_α sprzyja tworzeniu oddziaływań CH···π. Podczas kompresji fazy α kąt ψ_α zmniejsza się monotonicznie, a podczas przemiany fazowej skokowo zmniejsza się o około 10° umożliwiając utworzenie nowych, krótkich oddziaływań anagostycznych CH···Ru (rysunek 12).

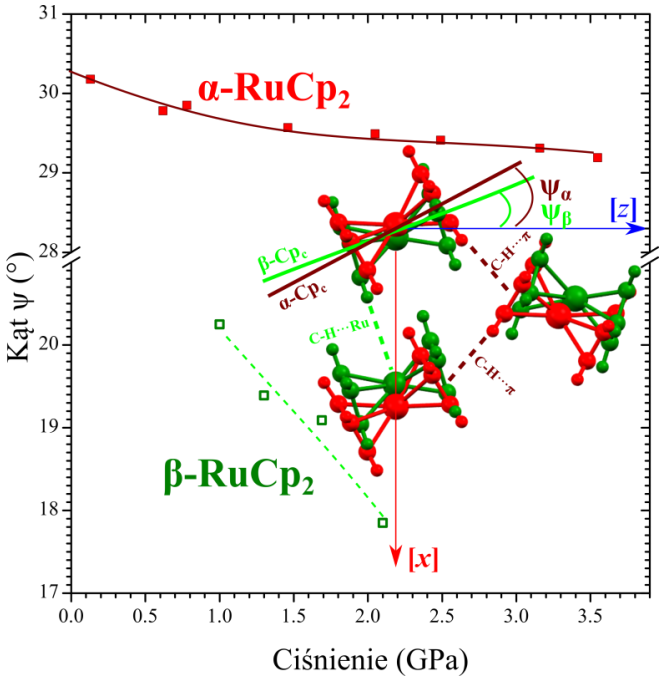

Rysunek 12. Kąty ψ_α (czerwony w fazie α) i ψ_β (zielony w fazie β) zawarte między pseudo 5-krotną osią symetrii cząsteczki rutenocenu, a osią [z] w fazie α i β. Rysunek strukturalny przedstawia nałożone cząsteczki w fazach α (czerwone) i β (zielone), wskazuje ich kąty ψ_α i ψ_β nachylenia do osi [z] oraz kontakty CH···π (czerwone) i CH···Ru (zielone). Wszystkie odchylenia standardowe są mniejsze niż symbole wykresu.

Rysunek 12 pokazuje jak niewielka zmiana kąta pochylenia cząsteczki w strukturze zmienia typ oddziaływań międzycząsteczkowych. Kąt ψ~30° kieruje atom wodoru do chmury elektronowej pierścienia Cp sąsiedniej cząsteczki. Zmiana kąta ψ, podczas przemiany fazowej ustawia inny atom wodoru tej cząsteczki w pozycji sprzyjającej utworzeniu oddziaływania anagostycznego z atomem rutenu. Szczegółowa analiza kontaktów (rysunek 13) wskazuje, że oddziaływania CH···π w głównej mierze stabilizują α-$RuCp_2$. Natomiast w stabilizacji fazy β rutenocenu główna rolę odgrywają oddziaływania CH···Ru, a kontakty CH···π stają się dłuższe i słabsze.

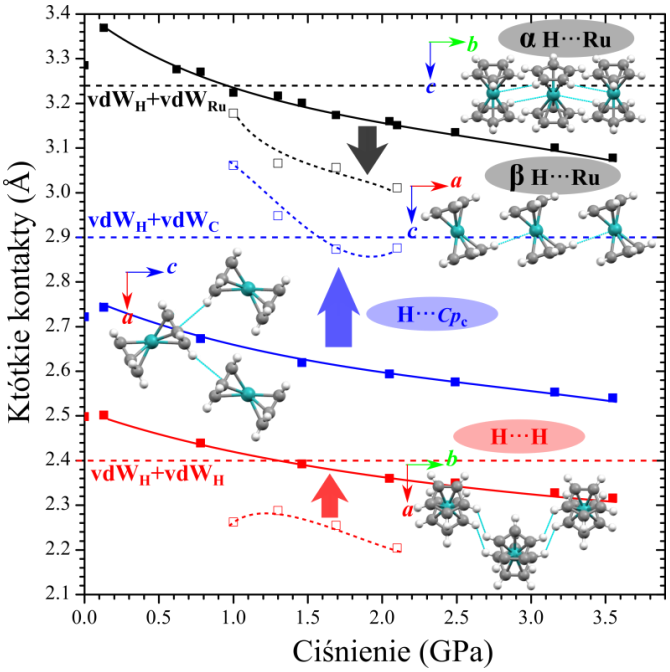

Rysunek 13. Krótkie kontakty w strukturach faz α i β rutenocenu: CH···Ru (kolor czarny), CH···π (niebieski) i CH···HC (czerwony). Kontakty CH···Ru w fazach α i β biegną w różnych kierunkach, stąd dwa wstawione rysunki faz α i β. Przerywane linie poziome wskazują sumy promieni van der Waalsa stosując wartości dla atomów: H (1.2 Å),[81] C (1.7 Å)[81] i Ru (2.05 Å).[82]

W fazie α istnieją wprawdzie kontakty CH···Ru zbliżone do sumy promieni van der Waalsa (rysunki 13 i 14), są one jednak inaczej zorientowane w przestrzeni niż dużo krótsze kontakty CH···Ru występujące w fazie β. W wyniku zmniejszenia odległości CH···Ru w fazie β wydłużeniu ulegają odległości między atomem rutenu i pozostałymi atomami wodoru znajdującymi się w jego sąsiedztwie.

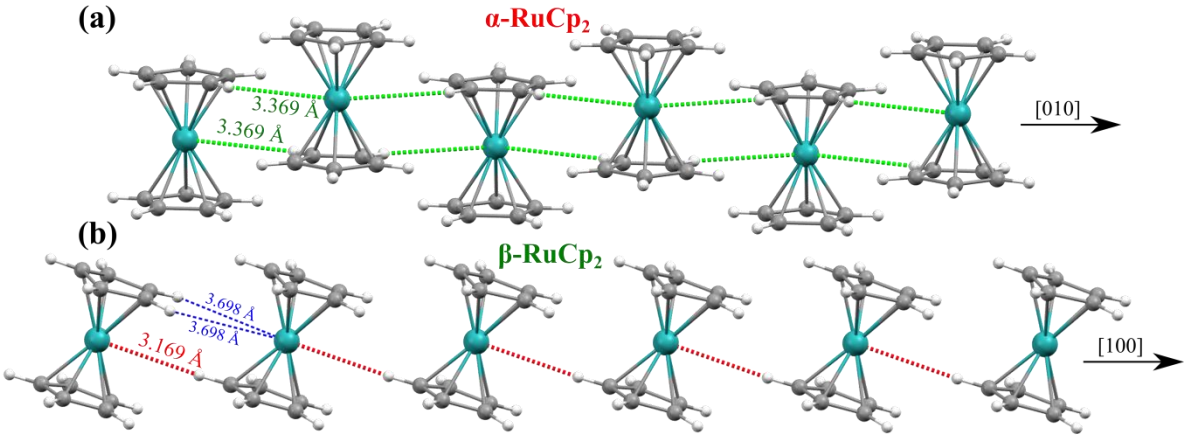

Rysunek 14. Najkrótsze oddziaływania CH···Ru (a) w fazie α biegnące wzdłuż kierunku [010] i (b) w fazie β, wzdłuż kierunku [100] Niebieskim kolorem na rysunku (b) oznaczono także odległości CH···Ru o 0.45 Å dłuższe niż suma promieni van der Waalsa.

4.4 Wiązania CH···M gigantycznie naprężają kryształ osmocenu

Według dostępnych wyników badań rutenocenu i osmocenu kryształy te w ciśnieniu atmosferycznym i temperaturach niskich i pokojowej są izostrukturalne. Zbliżona struktura sugerowała podobne zachowanie $RuCp_2$ i $OsCp_2$ pod wysokim ciśnieniem. Przeprowadzone przeze mnie badania ujawniły jednak różne przemiany strukturalne obu związków.

Osmocen w ciśnieniu 3.6 GPa przechodzi przemianę do fazy β. Podobnie jak w przypadku rutenocenu, przemiana ta jest destrukcyjna dla monokryształów (rysunek 15a-c). Monokryształy wysokociśnieniowej fazy β osmocenu otrzymałam metodą wysokociśnieniowego zarodkowania. Zarodkowanie to było możliwe dzięki znacznej histerezie przemiany rozciągającej się przy dekompresji do 0.3 GPa (rysunek 15d-f). Dlatego z ziaren fazy β otrzymanej powyżej 3.6 GPa mogłam w ciśnieniu niższym niż 2.24 GPa (temperatura krzepnięcia tetrahydrofuranu) metodą izochoryczną wyhodować monokryształ fazy β (podrozdział 3.1, strona 10).

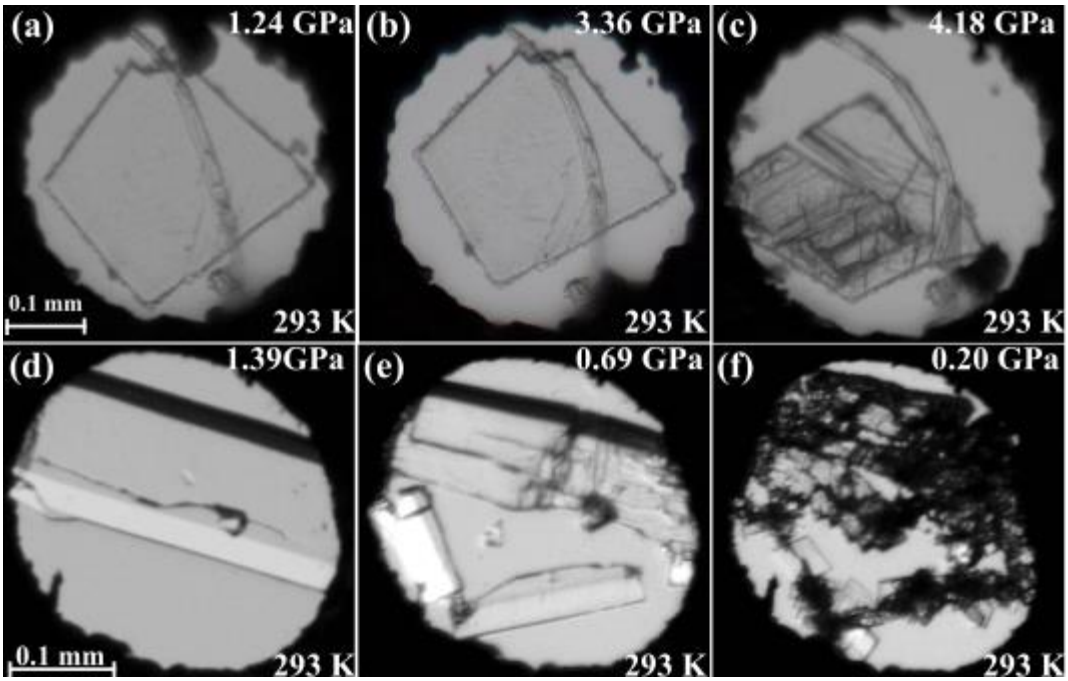

Rysunek 15. Uszkodzenia monokryształów osmocenu w wyniku przemiany fazowej zachodzące przy: (a-c) kompresji fazy α, oraz (d-f) dekompresji fazy β.

Wysokociśnieniowa przemiana fazowa osmocenu, ma szereg cech wspólnych z opisaną w **Artykule 3** przemianą rutenocenu: (i) izostrukturalność atmosferycznych faz α (grupa przestrzenna *Pnma*); (ii) duża histereza przemiany; i (iii) skrócenie kontaktów CH···*M* w wyniku przemiany fazowej. Natomiast faza β-$OsCp_2$ krystalizuje w grupie przestrzennej *Pcab*, innej niż wysokociśnieniowa grupa przestrzenna *Pcmb* fazy β-$RuCp_2$. Utrata płaszczyzny zwierciadlanej przechodzącej przez cząsteczkę w fazie β-$OsCp_2$ była zaskakująca, gdyż konformacja cząsteczki ulega zmianie jedynie o kąt $\tau = 0.33°$. Natomiast istotnie zmienia się ułożenie cząsteczek sąsiadujących, co prowadzi do powstania silnych oddziaływań anagostycznych. W fazie β-$RuCp_2$ atom metalu jest donorem elektronów dla jednego atomu wodoru (jeden z symetrycznie niezależnych kontaktów CH···Ru ulega znacznemu skróceniu kosztem wydłużenia pozostałych odległości CH···Ru). Natomiast w fazie β-$OsCp_2$ atom metalu staje się donorem elektronów dla czterech atomów wodoru (cztery symetrycznie niezależne kontakty CH···Os są krótsze niż suma promieni van der Waalsa, rysunek 16). Oddziaływania CH···*M* w metalocenach tworzą się w kierunku zapewniającym najlepszy dostęp do atomu centralnego – kąt γ zawarty pomiędzy kontaktem H···*M* i rzutem najbliższych wiązań C–H pierścieni Cp wynosi około 36° (rysunek 17).

Dostosowanie sposobu ułożenia cząsteczek w strukturze krystalicznej w taki sposób by możliwe było utworzenie czterech kontaktów spełniających powyższy warunek geometryczny wymaga obrotu cząsteczek, co łamie symetrię płaszczyzny zwierciadlanej (rysunek 17). Preferencja oddziaływań CH···*M* względem oddziaływań CH···π w warunkach wysokiego ciśnienia oraz warunek optymalnego dostępu grup CH do atomu osmu stanowi podstawę mechanizmu przemiany z fazy α do fazy β osmocenu.

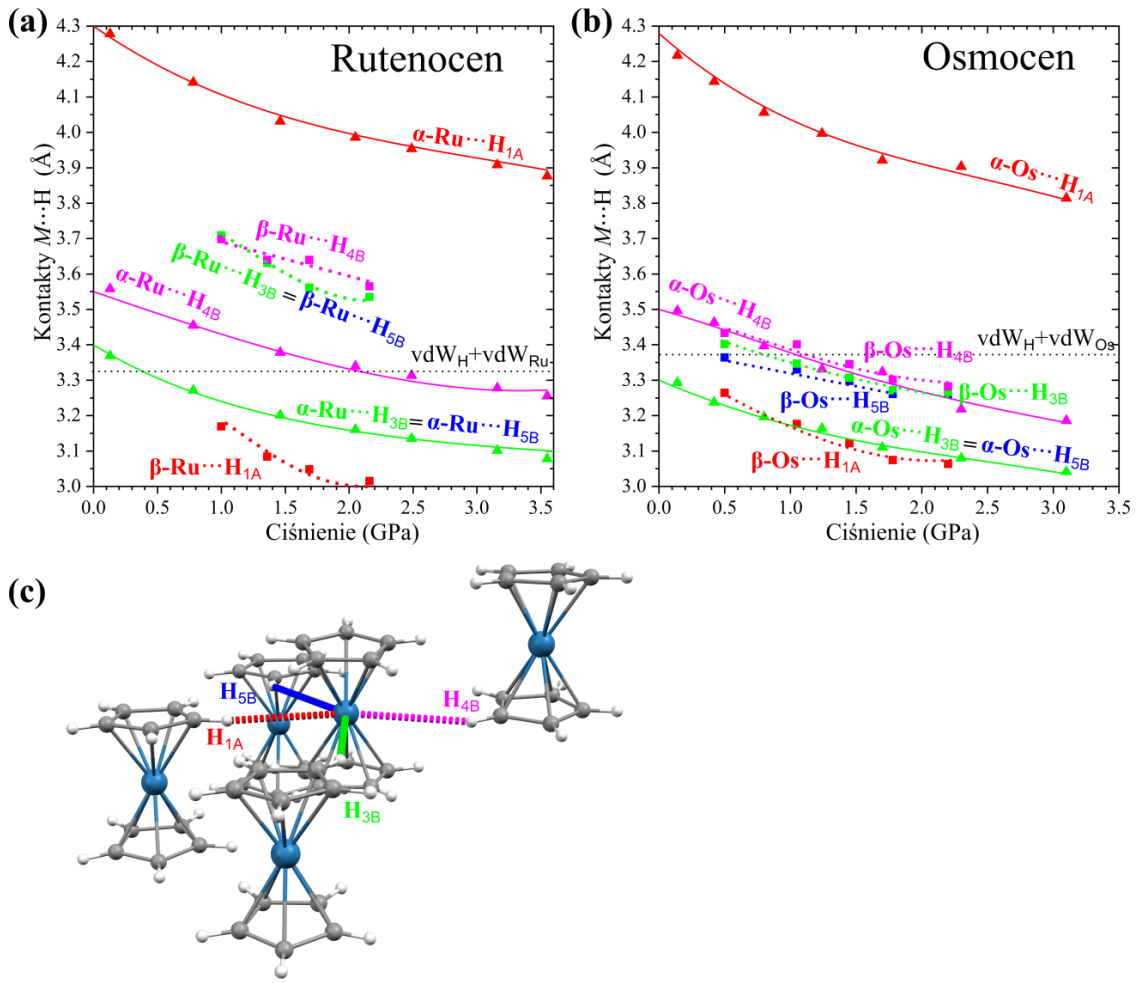

Rysunek 16. Zależność długości kontaktów CH···*M* od ciśnienia dla (a) rutenocenu i (b) osmocenu. Wartości dla faz α oznaczyłam trójkątami, a dla faz β kwadratami. Kropkowane poziome linie na wykresach oznaczają sumę promieni van der Waalsa (vdW_H=1.20Å wyznaczoną przez Bondiego[81] i vdW_{Os}=2.16Å, vdW_{Ru}=2.13Å wyznaczoną przez Hu[83]). Rysunek (c) przedstawia fragment struktury β-$OsCp_2$ w 1.05 GPa z zaznaczonymi oddziaływaniami anagtostycznymi CH···Os.

Najkrótsze kontakty w rutenocenie i osmocenie oraz ściśliwość tych kontaktów wykazują duże podobieństwo (rysunki 16 i 17), a ich najwyraźniejsze różnice

wynikają z powstania czterech krótkich wiązań CH···Os i jednego wiązania CH···Ru w kryształach faz β tych metalocenów.

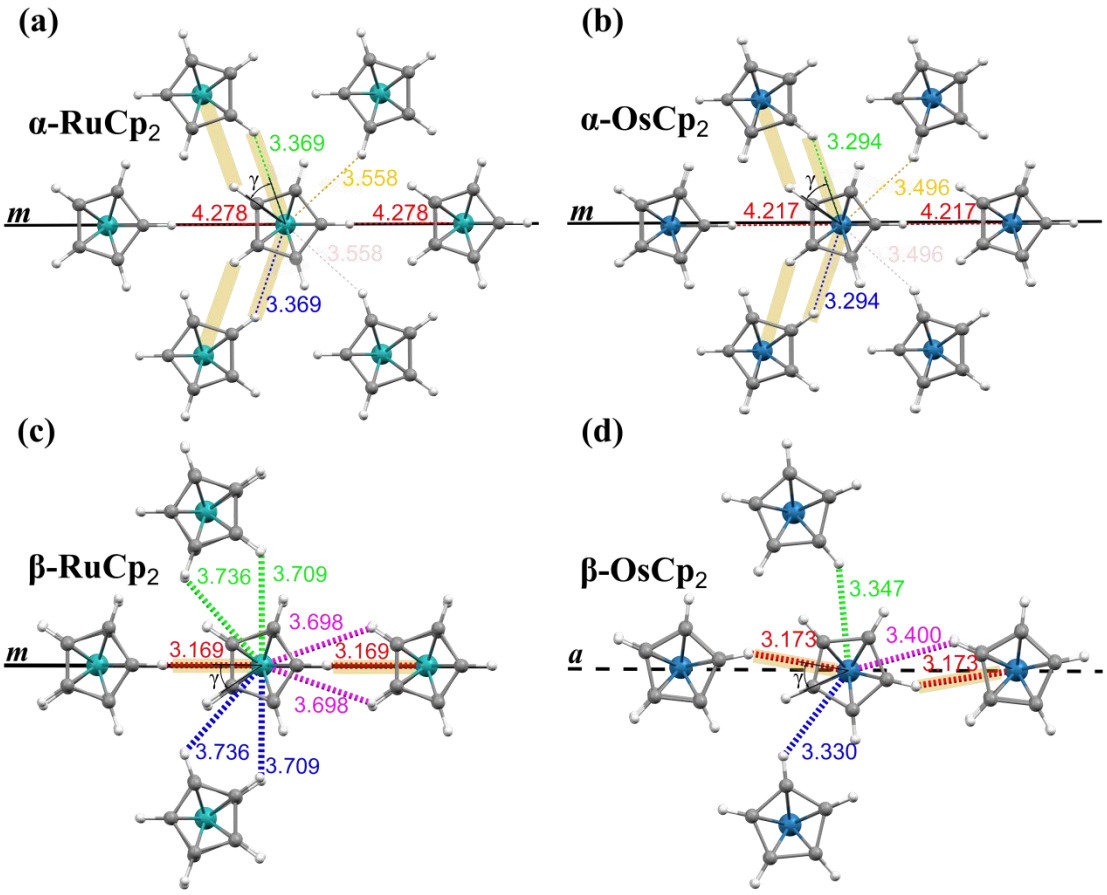

Rysunek 17. Kontakty anagostyczne CH···*M* w strukturach (a) α-$RuCp_2$, (b) α-$OsCp_2$, (c) β-$RuCp_2$ i (d) β-$OsCp_2$, w rzucie wzdłuż pseudo 5-krotnej osi symetrii cząsteczek. Płaszczyzny zwierciadlane *m* oznaczone są liniami ciągłymi, a płaszczyzna ślizgowa *a* linią przerywaną. Na rysunkach został oznaczony kąt γ =36°, związany z warunkiem geometrycznym tworzenia oddziaływań anagostycznych w cząsteczkach metalocenów.

W celu znalezienia przyczyny różnych przemian strukturalnych pod wysokim ciśnieniem dla rutenocenu i osmocenu przeprowadziłam obliczenia potencjału elektrostatycznego na powierzchni izolowanych cząsteczek $FeCp_2$, $RuCp_2$ i $OsCp_2$. Obliczenia wykonane zostały zarówno dla konformacji naprzemian- jaki i naprzeciwległej. Okazało się, że w metalocenach zawierających atom centralny z grupy 8 układu okresowego pierwiastków potencjał elektrostatyczny na powierzchni przy kationie centralnym jest ujemny (rysunek 18). Dla konformacji naprzemianległej ujemny potencjał jest rozproszony wokół jonu centralnego w formie sinusoidy, natomiast dla konformacji naprzeciwległej potencjał jest bardziej ujemny i koncentruje

się w pięciu miejscach, z których każde znajduje się pomiędzy czterema atomami węgla (dwoma z jednego i dwoma z drugiego pierścienia Cp). Taka konformacja naprzeciwległa eliminuje zawady steryczne i zwiększa powinowactwo do protonu przy tworzeniu kontaktów CH···*M*. Silniejsze i liczniejsze oddziaływania CH···*M* w strukturze osmocenu, w porównaniu z tymi z rutenocenu, są też konsekwencją wartości potencjału elektrostatycznego na powierzchni cząsteczek tych związków.

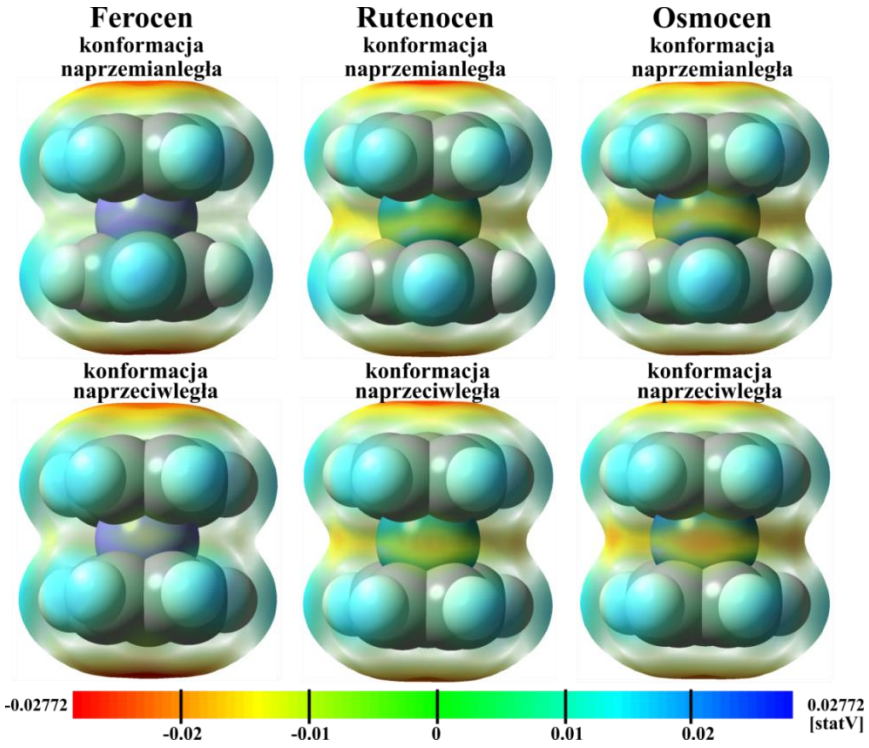

Rysunek 18. Potencjał elektrostatyczny na powierzchni cząsteczek ferrocenu, rutenocenu i osmocenu dla konformacji naprzemianleglej i naprzeciwległej, obliczony dla izolowanych cząsteczek metodą DFT.[65]

Zarejestrowane w ciśnieniu atmosferycznym 0.1 MPa i temperaturze 296 K widmo Ramana (400-1600 cm^{-1}) dla osmocenu jest analogiczne do tego rutenocenu.[84] Najintensywniejsze pasma są widoczne przy 356, 413, 1059 i 1097 cm^{-1} dla osmocenu i 332, 398, 1059 and 1097 cm^{-1} dla rutenocenu. Pasmo o najniższej liczbie falowej odpowiada rozciąganiu wiązań metal-pierścień Cp, drugie pasmo (ok. 400 cm^{-1}) jest związana z nachyleniem pierścienia, pasmo o średniej intensywności (ok. 1060 cm^{-1}) z wychylaniem wiązań C-H poza płaszczyznę pierścienia, podczas gdy pasmo o najwyższej liczbie falowej z rozciąganiem wiązań C-C.[85] Po przekroczeniu ciśnienia przemiany fazowej wzrasta intensywność pasma $\tilde{\nu}$ = 439 cm^{-1}, podczas gdy pasmo $\tilde{\nu} \approx 1060\ cm^{-1}$ traci na intensywności (rysunek 19). Efekt ten może być związany

z ograniczeniem ruchomości wiązań C-H poprzez zaangażowanie ich w tworzenie oddziaływań CH···*M*. Teorię tę wydaje się potwierdzać fakt, że zmiany te są bardzo wyraźne dla osmocenu, natomiast subtelne dla rutenocenu, co jest związane z czterokrotnie większą liczbą tworzonych kontaktów anagostycznych w β-$OsCp_2$ niż w β-$RuCp_2$.

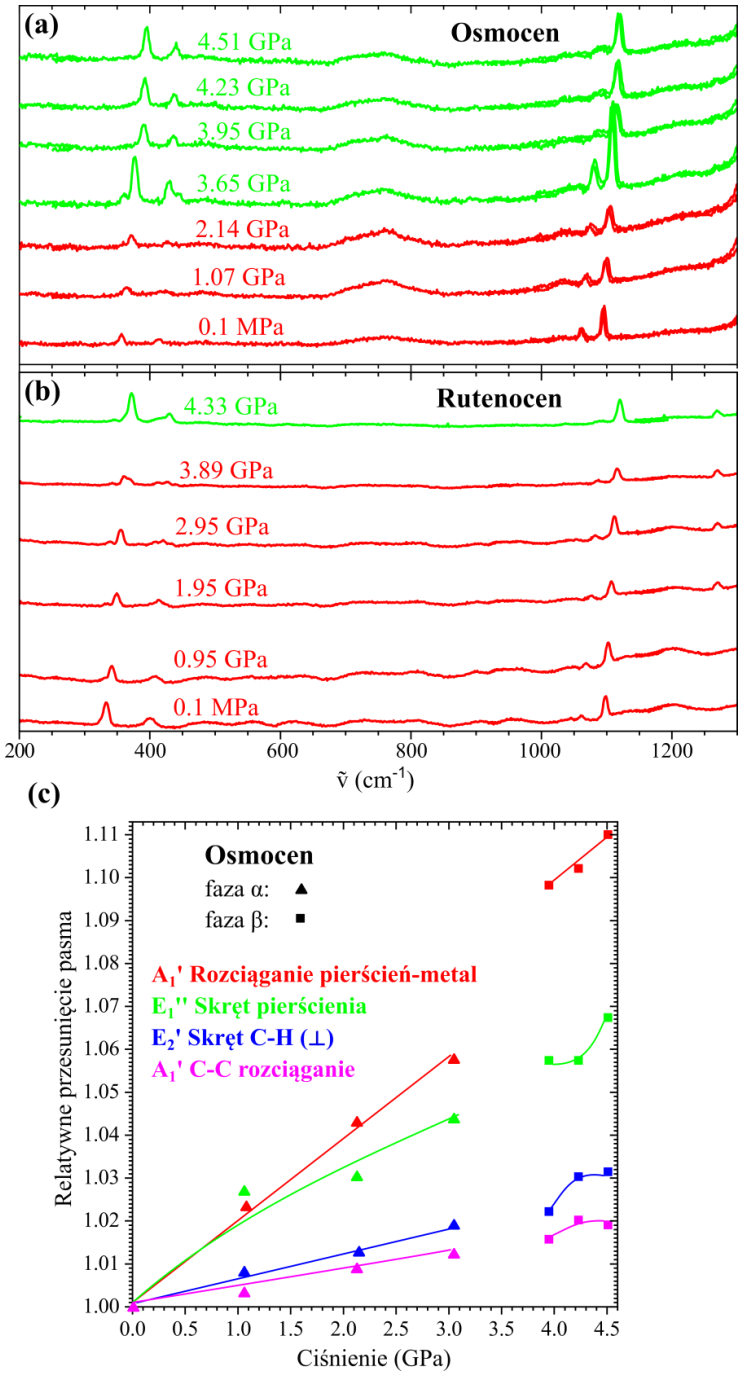

Rysunek 19. Widma Ramana dla (a) osmocenu i (b) rutenocenu. Kolorem czerwonym oznaczyłam fazę α, a kolorem zielonym fazę β. (c) Względne przesunięcia($\tilde{\nu}/\tilde{\nu}_0$) pasm widma Ramana osmocenu w funkcji ciśnienia.

Wszystkie pasma przesuwają się podczas kompresji w kierunku wyższych energii (rysunek 19c). Znacząca zmiana trendu w ciśnieniu przemiany widoczna jest jednak tylko dla pasma związanego z rozciąganiem wiązań metal-pierścień cyklopentadienylowy. Pozostałe sygnały są mniej wrażliwe na zmiany ciśnienia.

4.5 Nowe fazy osmocenu i rutenocenu ujawniają wspólne zachowanie konformacyjne regulowane wiązaniami anagostycznymi w prototypowych metalocenach

W serii analogicznych metalocenów o wspólnym wzorze MCp_2, rutenocen i osmocen wyróżniają się występowaniem jedynie w konformacji naprzeciwległej. Do niedawna sądzono też, że związki te występują jedynie w izostrukturalnych fazach α, które poddawano dotychczas badaniom jedynie w temperaturach od niskich do pokojowej. Wykonane przeze mnie badania DSC wykazały istnienie przemiany fazowej dla rutenocenu w 394.0 K i osmocenu w 421.5 K (rysunek 20). Kształt anomalii temperaturowej oraz brak histerezy dla przemian podczas chłodzenia i grzania (rysunek 21) wskazały, że są to przemiany drugiego rodzaju.

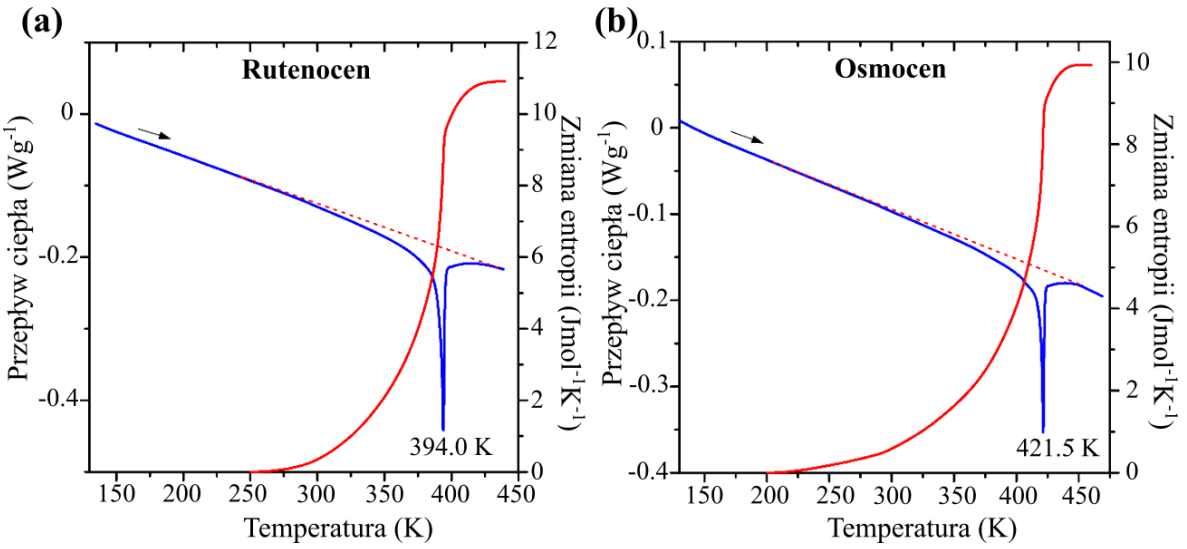

Rysunek 20. Sygnały DSC (niebieski) oraz zmiany entropii (czerwony) dla (a) rutenocenu i (b) osmocenu. Czerwone linie przerywane oznaczają przyjęte linie bazowe.

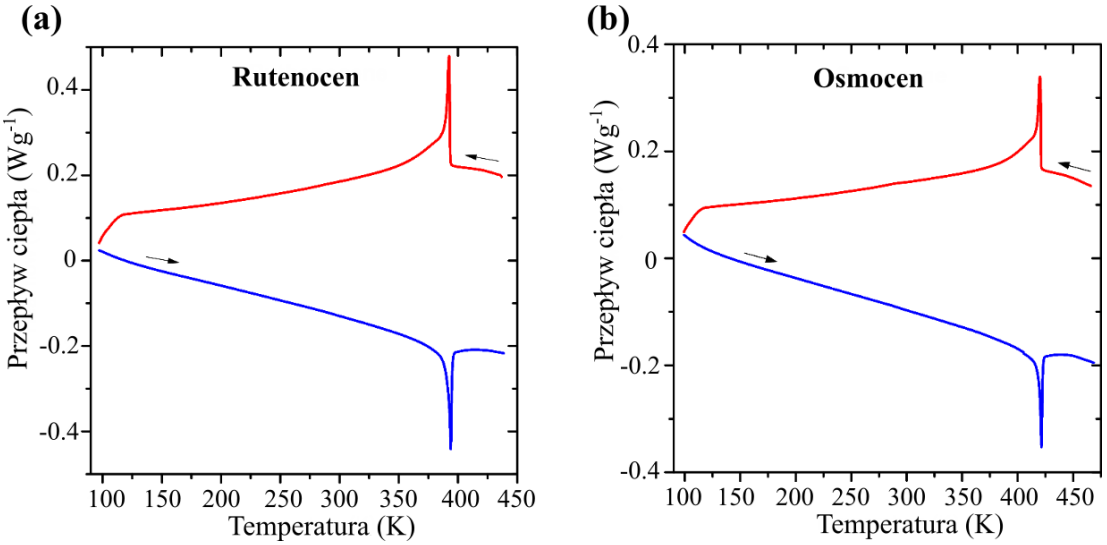

Rysunek 21. Sygnały DSC dla (a) rutenocenu i (b) osmocenu. Chłodzenie i grzanie próbki oznaczyłam kolorami niebieskim i czerwonym oraz strzałkami.

Rentgenowskie pomiary dyfraktometryczne kryształów $RuCp_2$ i $OsCp_2$ w wysokiej temperaturze pokazały, że ich nowe fazy γ (rysunek 22) są izostrukturalne. Posiadają symetrię grupy przestrzennej *Fmmm,* oraz że parametry komórki elementarnej faz α i γ są podobne (rysunek 23). Przemiana fazowa jest niemal niezauważalna dla parametru *a* komórki elementarnej osmocenu, podczas gdy rozszerzalność termiczna pozostałych parametrów dla rutenocenu i osmocenu jest wyraźnie anomalna i staje się ujemna. W wyniku przemian do faz γ, kationy metali Ru^{2+} i Os^{2+} przyjmują położenia na przecięciu trzech wzajemnie prostopadłych płaszczyzn zwierciadlanych.

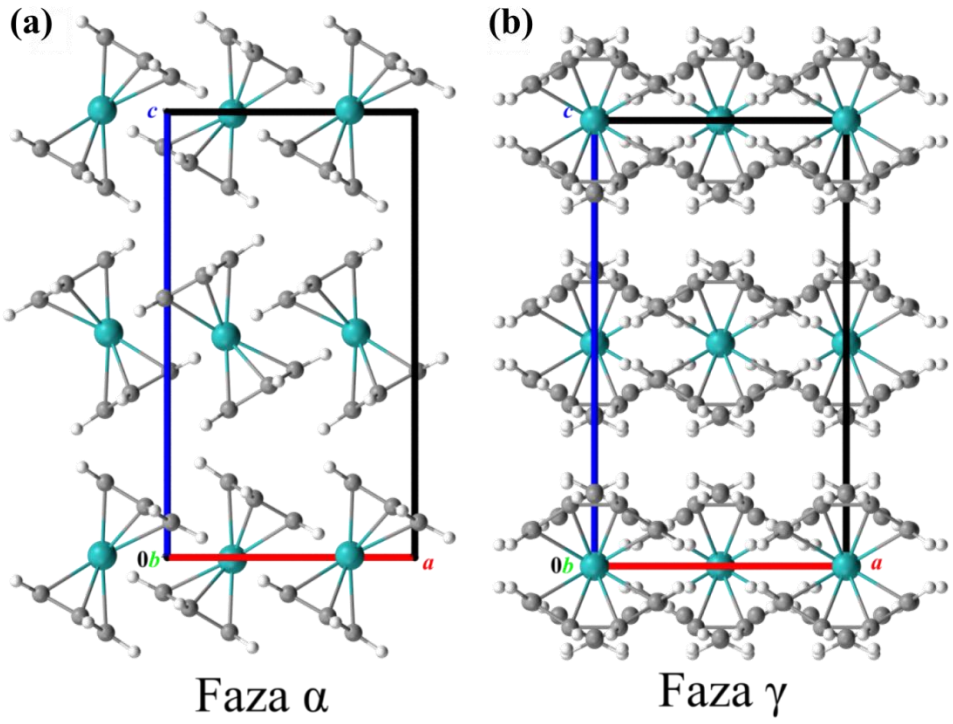

Rysunek 22. Struktury krystaliczne rutenocenu (a) w fazie α w 293 K i (b) w fazie γ w 395 K. Rzut fazy γ pokazuje nieporządek typu wahadłowego , ale pomija nieporządek obrotowy pierścieni w celu zwiększenia przejrzystości rysunku.

Fazy γ-$RuCp_2$ i γ-$OsCp_2$ są w podobny sposób nieuporządkowane ze współistnieniem dwóch składowych. Pierwsza składowe nieporządku polega na wychyleniu cząsteczek na obie strony płaszczyzny *m* prostopadłej do osi *x*, w sposób przypominający działanie huśtawki wagowej. Druga składowa to przeskoki pierścienia Cp o 36° wokół pseudo 5-krotnej osi symetrii cząsteczki.

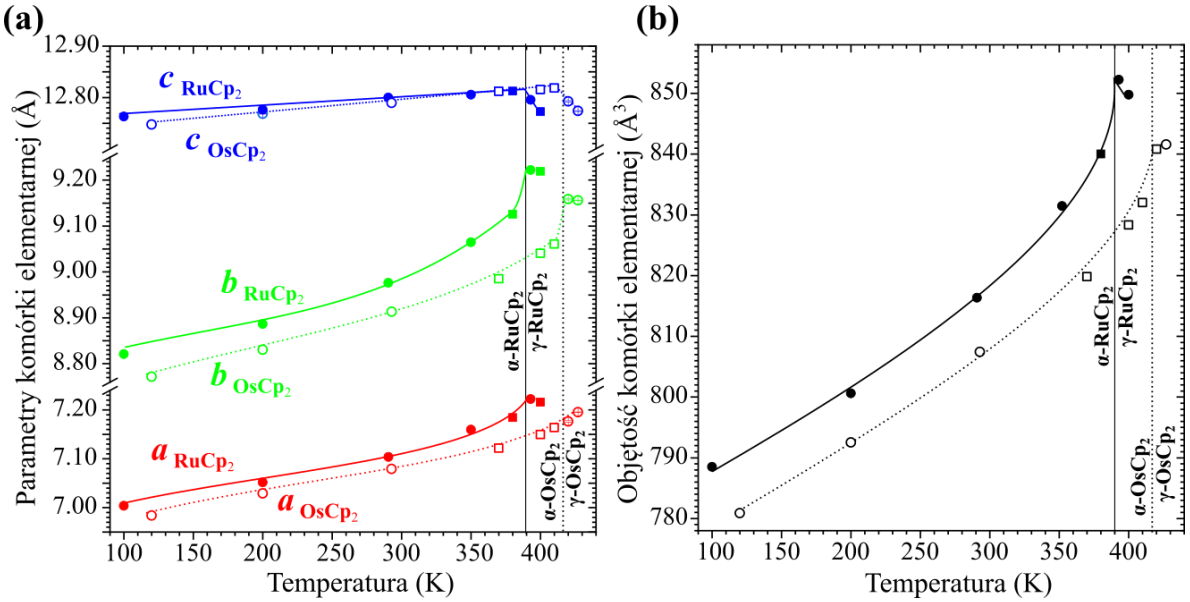

Rysunek 23. Zależność temperaturowa (a) parametrów komórek elementarnych $RuCp_2$ (pełne symbole, ciągłe linie) i $OsCp_2$ (puste symbole, kropkowane linie) oraz (b) objętości. Linie pionowe ciągłe i kropkowane oznaczają temperatury krytyczne przemian fazowych. Kwadraty i koła oznaczają odpowiednio dane uzyskane z pomiarów proszkowych i monokrystalicznych.

Każdy pierścień Cp w wyniku nieuporządkowania występuje w czterech pozycjach o jednakowym cząstkowym obsadzeniu równym 0.25 (rysunek 24). Dynamiczny nieporządek pierścieni Cp faz γ rutenocenu i osmocenu prowadzi do równych populacji konformerów naprzeciw- i naprzemianległych. Dostęp do kationu metalu przy tak nieuporządkowanej cząsteczce jest utrudniony, dlatego oddziaływania CH···*M* obecne w fazach α i β nie występują w fazach γ. Przemiana fazowa z fazy α do γ wydłuża odległości CH···*M* o ponad 0.2 Å (rysunek 24) znacząco powyżej sumy promieni van der Waalsa H i Ru (3.33 Å) oraz H i Os (3.36 Å).[81,83] Oddziaływania CH···*M* są rozmieszczone w przybliżeniu wzdłuż kierunku [010], który jest osią wychylenia cząsteczek w pierwszej składowej nieporządku (ruch huśtawki wagowej). Dlatego zwiększona odległość CH···*M* odpowiada największemu wydłużeniu parametru *b* komórki elementarnej w momencie zbliżania się do fazy γ (rysunek 23). Energia zerwania oddziaływań CH···*M*, związana z tym rozszerzalność termiczna kryształów oraz entropia związana z nieporządkiem, wszystko to przyczynia się do znacznej energii potrzebnej do przekształcenia rutenocenu i osmocenu w fazy γ. Wykres na rysunku 25 ilustruje zależność przejścia do faz nieuporządkowanych

z odległościami CH···*M* pokazując ich znaczącą rolę w kontrolowaniu konformacji molekularnej.

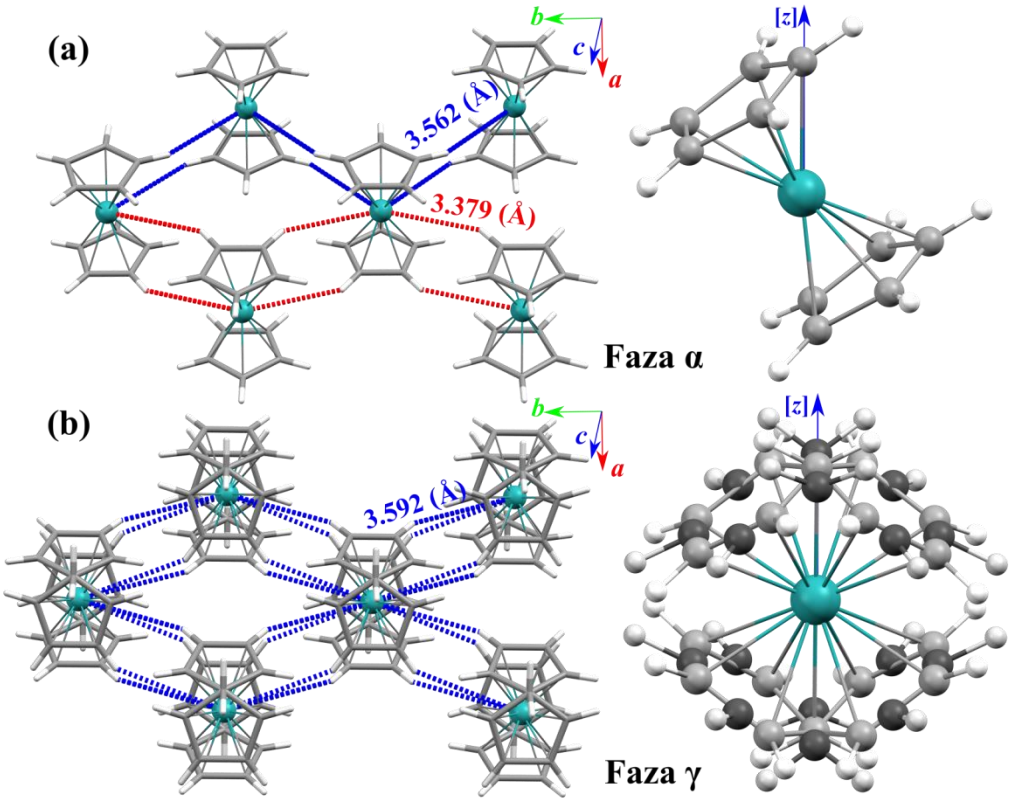

Rysunek 24. Autoseterogramy[80] rutenocenu w fazach α (a) i γ (b) oraz uporządkowana i nieuporządkowana cząsteczka pochylona względem osi [z]. Krótkie odległości CH···Ru przedstawiłam niebieskimi i czerwonymi liniami kropkowanymi, aby rozróżnić niezależne symetrycznie kontakty w fazie α.

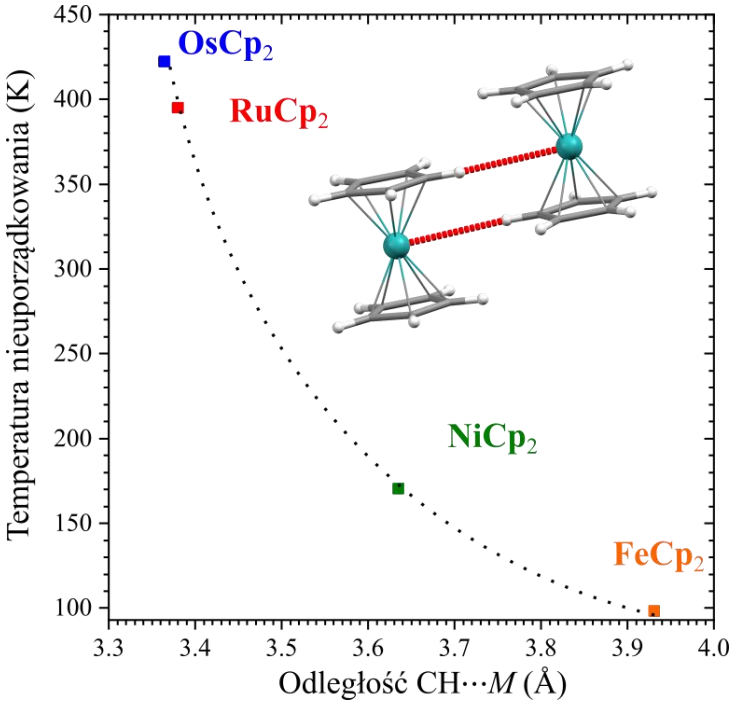

Rysunek 25. Temperatura wyzwalająca zaburzenie konformacyjne w prototypowych metalocenach w funkcji najkrótszej odległości CH···*M* mierzonej w warunkach atmosferycznych (293 K/0.1 MPa).

4.6 Metaloceny MCp_2 w krystalograficznej bazie danych

Jednym z celów moich badań była analiza konformacyjnych przemian fazowych metalocenów. W tabeli 1 zestawiłam częstość występowania konformacji naprzemian- i naprzeciwległej w strukturach zawierających ugrupowanie MCp^*_2 zdeponowanych w krystalograficznej bazie CSD. Związki kompleksowe o najwyższej trwałości spełniają regułę 18 elektronów walencyjnych. Dla cząsteczek metalocenów MCp_2, w których każdy z dwóch pierścieni cylopentadienylowych wnosi do kompleksu po 6 elektronów, reguła jest spełniona gdy atom centralny wnosi także 6 elektronów walencyjnych. Z uwagi na trwałość, liczba modeli struktur zdeponowanych w bazie CSD, zawierających ugrupowanie MCp^*_2, gdzie *M* to kation o 6 elektronach walencyjnych (Fe^{2+}, Ru^{2+} i Os^{2+}) jest znacząco wyższa niż liczba struktur zdeponowanych zawierających ugrupowanie MCp^*_2, gdzie *M* to kation o liczbie elektronów walencyjnych różnej od 6. Struktury zawierające cząsteczki metalocenów obojętnych elektrycznie o konfiguracji elektronowej atomu centralnego [Y] nd^6 (gdzie Y to atom helowca, a *n* to okres, w którym dany helowiec się znajduje) znacznie

częściej występują w konformacji naprzeciwległej niż naprzemianległej. Zarówno dla konfiguracji elektronowych atomów centralnych innych niż [Ar/Kr/Xe]d^6 jak i dodatniego ładunku cząsteczki metalocenu wzrastają populacje konformerów naprzemianległych (tabela 1, rysunek 26a).

Tabela 1. Konformery w strukturach zawierających cząsteczki metalocenów o wzorze ogólnym MCp$^*_2$ w bazie CSD (wersja 5.43). Jako konformery naprzemian- i naprzeciwległe przyjęłam cząsteczki metalocenów o kącie torsyjnym τ odpowiednio $35 \leq |\tau| \leq 36°$ i $0 \leq |\tau| \leq 1°$.

M	Konfiguracja elektronowa	Konformer naprzemianległy [%]	Konformer naprzeciwległy [%]	Ilość rekordów z bazy
V^{2+}	[Ar] d^3	40	7	15
Cr^{3+}	[Ar] d^3	34	2	53
Cr^{2+}	[Ar] d^4	26	9	54
Mn^{2+}	[Ar] d^5	31	2	36
Fe^{3+}	[Ar] d^5	18	9	897
Fe^{2+}	[Ar] d^6	3	**9**	23263
Ru^{2+}	[Kr] d^6	3	**11**	586
Os^{2+}	[Xe] d^6	0	**22**	37
Rh^{3+}	[Kr] d^6	10	8	48
Co^{3+}	[Ar] d^6	13	8	844
Co^{2+}	[Ar] d^7	11	7	200
Ni^{3+}	[Ar] d^7	30	5	20
Ni^{2+}	[Ar] d^8	20	10	49

Cp* - pierścień cyklopentadienylowy z dowolnymi podstawnikami

Wraz ze wzrostem liczby atomowej atomu centralnego ugrupowania MCp$^*_2$ w grupie 8 układu okresowego wzrasta dysproporcja pomiędzy konformacją naprzeciw- i naprzemianległą w strukturach zdeponowanych, na korzyść konformacji naprzeciwległej (tabela 1, rysunek 26). Do zaklasyfikowania konformacji MCp$^*_2$ jako naprzeciw- lub naprzemianległa, na rysunku 26 i w tabeli 1 zastosowałam hisogramy o krokach zliczeń 1°. Dwukrotne poszerzenie klasy histogramu spowodowałoby wzrost odsetek konformerów, np. dla konformeru naprzemianległego Fe^{2+}Cp$^*_2$ z 3% do 5%, a naprzeciwległego z 9% do 18%.

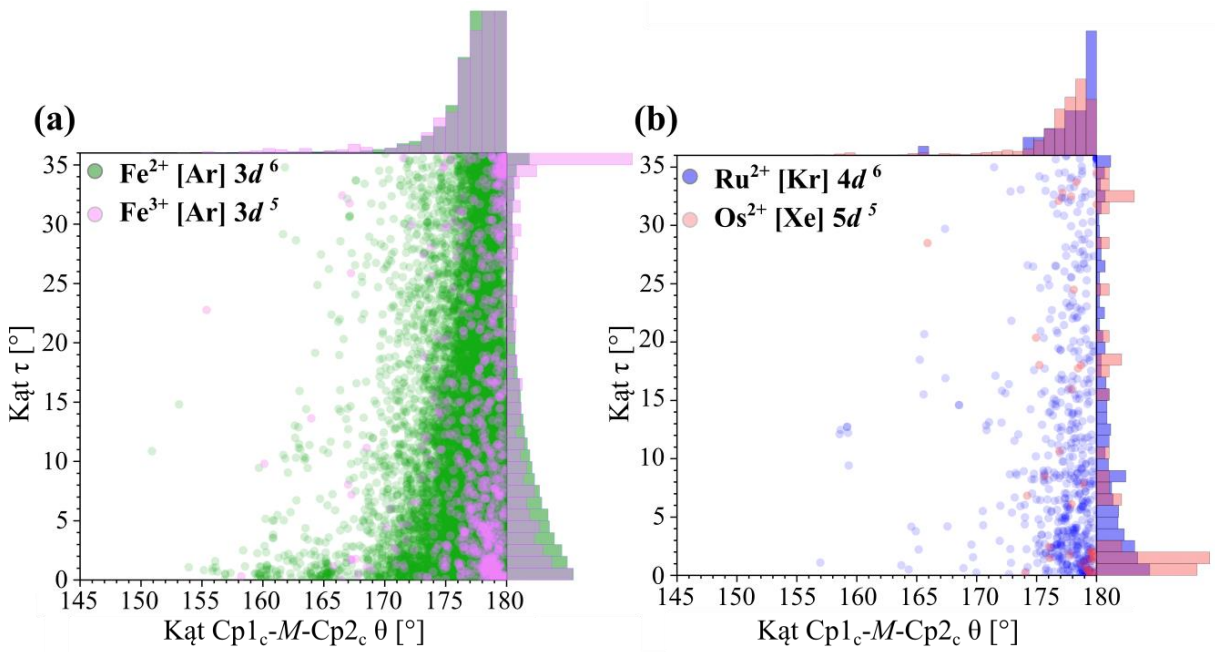

Rysunek 26. Statystyczny rozkład konformacji (τ) wykreślonych w funkcji kąta zgięcia cząsteczki ($Cp1_c$-*M*-$Cp2_c$) struktur MCp^*_2 zawierających (a) Fe^{2+} (zielony) i Fe^{3+} (różowy) oraz (b) Ru^{2+} (niebieski) i Os^{2+} (czerwony). Szczegóły dotyczące zdefiniowania kątów i restrykcji użytych w zapytaniu do bazy zostały opisane w części poświęconej metodom badawczym (Podrozdział 3.7, strona 12). Do zilustrowania częstości występowania danej konformacji zastosowałam hisogramy, o szerokości klasy 1°.

Przeszukałam bazę CSD również pod kątem nieporządku metalocenów. Wśród 17610 zdeponowanych struktur zawierających $FeCp^*_2$ 25% zostało zaklasyfikowanych jako struktury nieuporządkowane. Wynik ten wydaje się jednak nie odzwierciedlać rzeczywistości z uwagi na fakt, że pierwsze struktury ferrocenu I zostały zdeponowane w bazie jako uporządkowane, a klasyfikator nieporządku może dotyczyć również innych niż ugrupowanie MCp^*_2 części zdeponowanych struktur.

5. Wnioski o konformacyjnych fazach metalocenów

W mojej rozprawie doktorskiej pokazałam, że właściwości konformacyjne prostych metalocenów MCp_2 można usystematyzować i wyjaśnić na podstawie powinowactwa jonów metalu do protonu. Dla rutenocenu i osmocenu wiązania anagostyczne CH···*M* wyraźnie stabilizują konformację naprzeciwległą. W wysokim ciśnieniu oba te związki ulegają przejściu do fazy β, w której pomiędzy konformerami naprzeciwległymi powstają jeszcze silniejsze (krótsze) wiązania CH···*M*. Natomiast w wysokiej temperaturze oddziaływania te ulegają zerwaniu, co prowadzi do powstania nowych

faz γ rutenocenu i osmocenu o nieuporządkowanych konformacjach pierścieni cyklopentadienylowych. Nowo otrzymane fazy γ są pierwszymi polimorfami rutenocenu i osmocenu, w których nie występują wyłącznie konformery naprzeciwległe, ale 50% populacji stanowią konformery naprzemianległe. Tym samym oprócz ferrocenu, dotychczas uznawanego za jedyny metalocen ulegający przemianom konformacyjnym, również rutenocen i osmocen dołączyły do metalocenów o różnych konformacjach. Przedstawiłam także nowy sposób wyznaczania konformacji cząsteczek nieuporządkowanych metalocenów oparty na słabej korelacji położeń pierścieni Cp w cząsteczkach. Koncepcja ta dopuszcza występowanie różnych konformacji w jednej strukturze oraz występowanie konformerów niecentrosymetrycznych, pomimo położenia nieuporządkowanej cząsteczki na centrum inwersji. Przedstawiłam zależności temperaturowe i ciśnieniowe tak „rozplecionych", w matematycznej terminologii, funkcji konformacji i obsadzenia nieuporządkowanych położeń. Ta analiza konformacyjna pokazała, że wpływ ciśnienia i temperatury na struktury metalocenów jest znacznie bardziej złożony niż zakładano, a powielane w podręcznikach obrazki cząsteczek o symetrii D_{5d} i D_{5h} (S_{10}) są znacznym uproszczeniem, wykluczającym powiązanie struktury cząsteczek metalocenów z właściwościami kryształów. Nowe podejście do rozważań nad nieuporządkowaniem pierścieni cyklopentadienylowych stanowi także strukturalne wyjaśnienie obserwowanej wcześniej dielektrycznej odpowiedzi ferrocenu w fazie I.

Od odkrycia ferrocenu i pokrewnych metalocenów oraz następnie burzliwych badań strukturalnych, kalorymetrycznych, spektroskopowych i innych minęło ponad 70 lat. W tym czasie chemia metalocenów i metaloorganiczna przeżyła i nadal przeżywa dynamiczny rozkwit (rysunek 27a). W tym kontekście brak pełnych informacji o podstawowych związkach modelowych jest zadziwiający. Sam fakt, że przeoczono dwie fazy ferrocenu: wysokociśnieniową fazę I′ i modulowaną fazę I″ ilustruje „skalę zaniedbań". Do 2013 roku poznano trzy odmiany polimorficzne ferrocenu, oraz po jednej rutenocenu i osmocenu, później w naszym Zakładzie odkryto sześć kolejnych faz ferrocenu, rutenocenu i osmocenu (rysunek 27b). Uzyskane informacje

strukturalne i konformacyjne są kluczowe dla zrozumienia właściwości i interpretacji wyników otrzymanych dla podobnych związków.

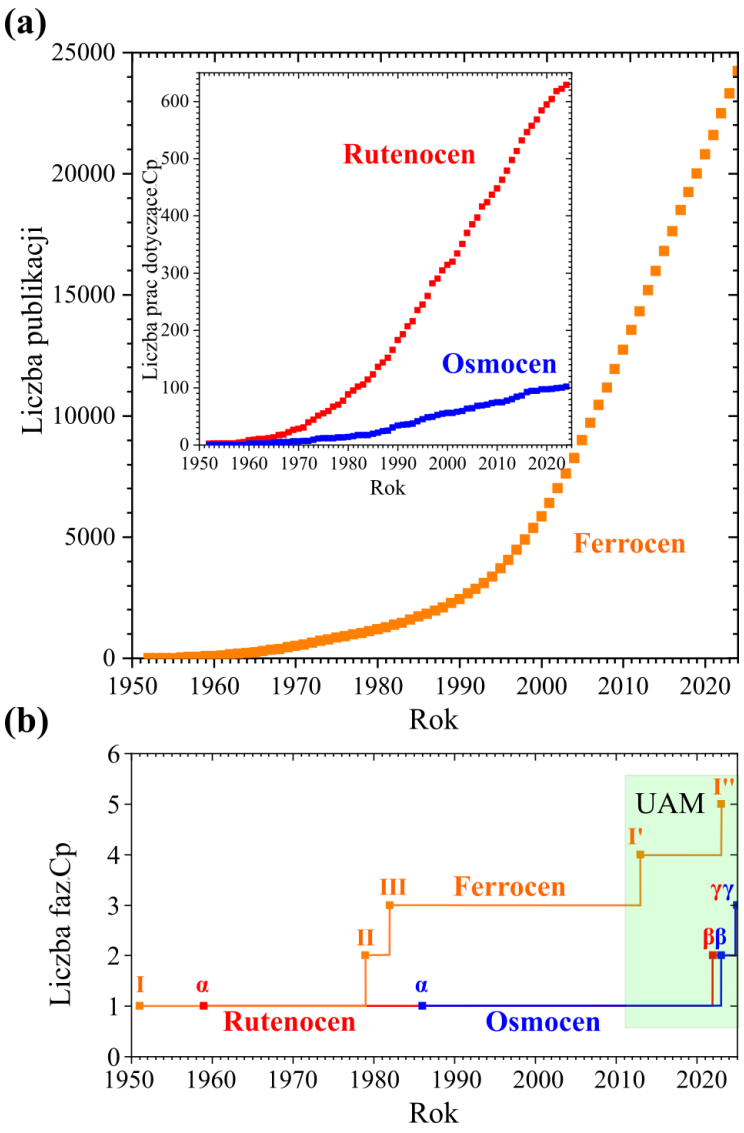

Rysunek 27. (a) Kumulanty liczb prac opublikowanych od 1951 do 2024 ze słowem **ferrocen** (pomarańczowy), **rutenocen** (czerwony) i **osmocen** (niebieski) zawartym w tytule, streszczeniu lub słowach kluczowych, na podstawie bazy SCOPUS. (b) Liczba odkrytych odmian polimorficznych ferrocenu (pomarańczowy), rutenocenu (czerwony) i osmocenu (niebieski) w funkcji czasu.

Podsumowując, mój wkład w poszerzenie zakresu wiedzy dotyczącej podstawowych metalocenów obejmuje: (i) odkrycie w ciśnieniu 1.3 GPa izostrukturalnej przemiany $NiCp_2$ eliminującej nieporządek cząsteczki; (ii) analizę konformacyjną nieuporządkowanej fazy I-$NiCp_2$ w warunkach wysokiego ciśnienia i niskiej temperatury; (iii) analizę konformacyjną nieuporządkowanej fazy I-$FeCp_2$

w warunkach wysokiego ciśnienia; (iv) otrzymanie i wyznaczenie struktury nowej, wysokociśnieniowej fazy β-$RuCp_2$; (v) otrzymanie i wyznaczenie struktury nowej, wysokociśnieniowej fazy β-$OsCp_2$; (vi) otrzymanie i wyznaczenie nowej wysokotemperaturowej fazy γ-$RuCp_2$; (vii) otrzymanie i wyznaczenie nowej wysokotemperaturowej fazy γ-$OsCp_2$; (viii) wyznaczenie wspólnego mechanizmu przemian konformacyjnych, opartego na powinowactwie atomu centralnego metalocenu do tworzenia oddziaływań CH···*M* (osiągnięcia te podsumowałam na rysunku 28).

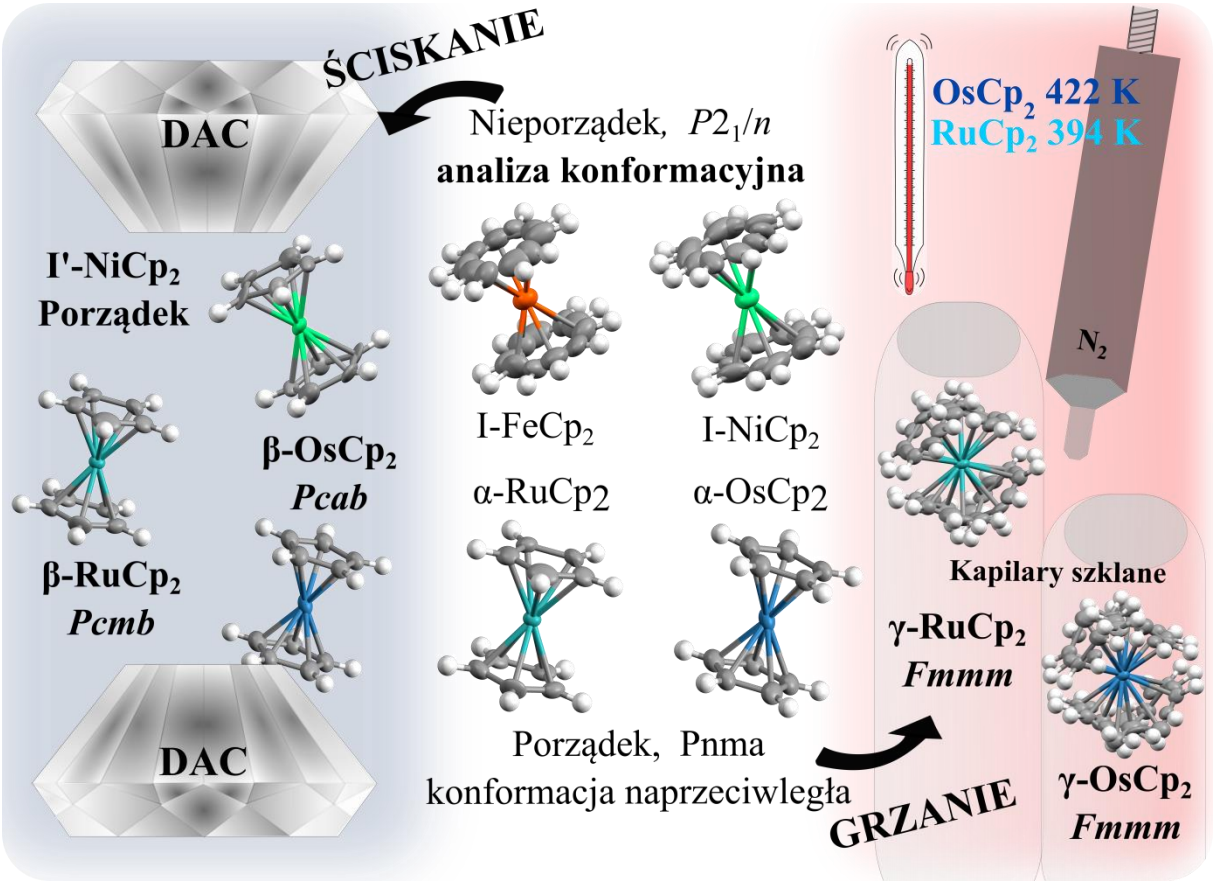

Rysunek 28. Podsumowanie osiągnięć uzyskanych w trakcie realizacji pracy doktorskiej.

6. Referencje

(1) Kealy, T. J.; Pauson, P. L. A New Type of Organo-Iron Compound. *Nature* **1951**, *168* (4285), 1039–1040. DOI: 10.1038/1681039b0.

(2) Dunitz, J. D.; Orgel, L. E.; Rich, A. The Crystal Structure of Ferrocene. *Acta Crystallogr.* **1956**, *9* (4), 373–375. DOI: 10.1107/S0365110X56001091.

(3) Seiler, P.; Dunitz, J. D. The Structure of Nickelocene at Room Temperature and at 101 K. *Acta Crystallogr. Sect. B Struct. Crystallogr. Cryst. Chem.* **1980**, *36* (10), 2255–2260. DOI: 10.1107/S0567740880008539.

(4) Hardgrove, G. L.; Templeton, D. H. The Crystal Structure of Ruthenocene. *Acta Crystallogr.* **1959**, *12* (1), 28–32. DOI: 10.1107/S0365110X59000081.

(5) Boeyens, J. C. A.; Levendis, D. C.; Bruce, M. I.; Williams, M. L. Crystal Structure of Osmocene, Os(η-C_5H_5)$_2$. *J. Crystallogr. Spectrosc. Res.* **1986**, *16* (4), 519–524. DOI: 10.1007/BF01161040.

(6) Antipin, M. Y.; Lobkovskii, E. B.; Semenenko, K. N.; Soloveichik, G. L.; Struchkov, Y. T. X-Ray Structural Study of Vanadocene. *J. Struct. Chem.* **1979**, *20* (5), 810–811. DOI: 10.1007/BF00746790.

(7) Flower, K. R.; Hitchcock, P. B. Crystal and Molecular Structure of Chromocene (η^5-C_5H_5)$_2$Cr. *J. Organomet. Chem.* **1996**, *507* (1–2), 275–277. DOI: 10.1016/0022-328X(95)05747-D.

(8) Antipin, M. Y.; Boese, R.; Augart, N.; Schmid, G. Redetermination of the Cobaltocene Crystal Structure at 100 K and 297 K: Comparison with Ferrocene and Nickelocene. *Struct. Chem.* **1993**, *4* (2), 91–101. DOI: 10.1007/BF00677370.

(9) Jaenschke, A.; Paap, J.; Behrens, U. Structures of Polar Magnesium Organyls: Synthesis and Structure of Base Adducts of Bis(Cyclopentadienyl)Magnesium. *Z. fur Anorg. und Allg. Chemie* **2008**, *634* (3), 461–469. DOI: 10.1002/zaac.200700445.

(10) Langmuir, I. Types of Valence. *Science* **1921**, *54* (1386), 59–67. DOI: 10.1126/science.54.1386.59.

(11) Mitchell, P. R.; Parish, R. V. The Eighteen Electron Rule. *J. Chem. Educ.* **1969**, *46* (12), 811. DOI: 10.1021/ed046p811.

(12) Seiler, P.; Dunitz, J. D. The Structure of Triclinic Ferrocene at 101, 123 and 148 K. *Acta Crystallogr. Sect. B Struct. Crystallogr. Cryst. Chem.* **1979**, *35* (9), 2020–2032. DOI: 10.1107/s0567740879008384.

(13) Seiler, P.; Dunitz, J. D. Low-Temperature Crystallization of Orthorhombic Ferrocene: Structure Analysis at 98 K. *Acta Crystallogr. Sect. B Struct. Crystallogr. Cryst. Chem.* **1982**, *38* (6), 1741–1745. DOI: 10.1107/S0567740882007080.

(14) Seeman, J. I.; Cantrill, S. Wrong but Seminal. *Nat. Chem.* **2016**, *8* (3), 193–200. DOI: 10.1038/nchem.2455.

(15) Werner, H. At Least 60 Years of Ferrocene: The Discovery and Rediscovery of the Sandwich Complexes. *Angew. Chemie* **2012**, *51* (25), 6052–6058. DOI: 10.1002/anie.201201598.

(16) Cotton, F. A., Wilkinson, G., Murillo, C. A., Bochmann, M. *Advanced Inorganic Chemistry*; John Wiley & Sons, **1999**.

(17) Eliel, E. L.; Wilen, S. H.; Mander, L. N. *Stereochemistry of Organic Compounds*; John Wiley & Sons: New York, **1994**.

(18) Lee, J. D. *Concise Inorganic Chemistry*; Blackwell Science: Oxford, **1996**.

(19) Paliwoda, D.; Kowalska, K.; Hanfland, M.; Katrusiak, A. U-Turn Compression to a New Isostructural Ferrocene Phase. *J. Phys. Chem. Lett.* **2013**, *4* (23), 4032–4037. DOI: 10.1021/jz402254b.

(20) Paliwoda, D.; Hanfland, M.; Katrusiak, A. Pressure-Enhanced Environment Effects in Ferrocene Phases. *J. Phys. Chem. C* **2019**, *123* (42), 25719–25723. DOI: 10.1021/acs.jpcc.9b07512.

(21) Katrusiak, A.; Rusek, M.; Dušek, M.; Petříček, V.; Szafrański, M. Dipole-Moment Modulation in New Incommensurate Ferrocene. *J. Phys. Chem. Lett.* **2023**, *14* (13), 3111–3119. DOI: 10.1021/acs.jpclett.3c00215.

(22) Takusagawa, F.; Koetzle, T. F. A Neutron Diffraction Study of the Crystal Structure of Ferrocene. *Acta Crystallogr. Sect. B Struct. Crystallogr. Cryst. Chem.* **1979**, *35* (5), 1074–1081. DOI: 10.1107/S0567740879005604.

(23) Brock, C. P.; Fu, Y. Rigid-Body Disorder Models for the High-Temperature Phase of Ferrocene. *Acta Crystallogr. Sect. B Struct. Sci.* **1997**, *53* (6), 928–938. DOI: 10.1107/S0108768197005132.

(24) Calvarin, G.; Weigel, D. Mise En Évidence et Étude, Par Diffraction Des Rayons X Sur Poudre, d'une Transition Ordre–Désordre Pour Le Nickelocène $Ni(C_5H_5)_2$ *J. Appl. Crystallogr.* **1976**, *9* (3), 212–215. DOI: 10.1107/S0021889876010984.

(25) Mason, W. R.; Gray, H. B. Electronic Structures of Square-Planar Complexes. *J. Am. Chem. Soc.* **1968**, *90* (21), 5721–5729. DOI: 10.1021/ja01023a012.

(26) Cotton, A. F.; Duraj, S. A.; Powell, G. L.; Roth, W. J. Comparative Structural Studies of the First Row Early Transition Metal(III) Chloride Tetrahydrofuran Solvates. *Inorganica Chim. Acta* **1986**, *113* (1), 81–85. DOI: 10.1016/S0020-1693(00)86863-2.

(27) Bellard, S.; Rubinson, K. A.; Sheldrick, G. M. Crystal and Molecular Structure of Vanadium Hexacarbonyl. *Acta Crystallogr. Sect. B Struct. Crystallogr. Cryst. Chem.* **1979**, *35* (2), 271–274. DOI: 10.1107/S0567740879003332.

(28) Abernethy, C. D.; Cowley A. H.; Jones, R. A. Reaction of Nickelocene with 1,3-Dimesitylimidazolium Chloride. *J. Organomet. Chem.* **2000**, *596* (1–2), 3–5. DOI: 10.1016/S0022-328X(99)00557-4.

(29) Pasynkiewicz, S.; Pietrzykowski, A.; Bukowska, L.; Słupecki, K.; Jerzykiewicz, L. B.; Urbańczyk-Lipkowska, Z. Reactions of Nickelocene with Diphenylmethyl- and Triphenylmethyllithium. *J. Organomet. Chem.* **2000**, *604* (2), 241–247. DOI: 10.1016/S0022-328X(00)00275-8.

(30) Walsh, A. D. The Properties of Bonds Involving Carbon. *Discuss. Faraday Soc.* **1947**, *2*, 18-25. DOI: 10.1039/df9470200018.

(31) McKean, D. C. Individual CH Bond Strengths in Simple Organic Compounds: Effects of Conformation and Substitution. *Chem. Soc. Rev.* **1978**, *7* (3), 399-422. DOI: 10.1039/cs9780700399.

(32) Parkin, G.; Bunel, E.; Burger, B. J.; Trimmer, M. S.; Van Asselt, A.; Bercaw, J. E. Alpha- and Beta-Migratory Insertion and Elimination Processes for Alkyl Complexes of Permethyl-Scandocene and Permethyltantalocene. *J. Mol. Catal.* **1987**, *41* (1–2), 21–39. DOI: 10.1016/0304-5102(87)80017-2.

(33) Brookhart, M.; Green, M. L. H.; Parkin, G. Agostic Interactions in Transition Metal Compounds. *Proc. Natl. Acad. Sci.* **2007**, *104* (17), 6908–6914. DOI: 10.1073/pnas.0610747104.

(34) Trofimenko, S. Molybdenum Complexes with Noninert-Gas Configuration. *Inorganic* **1970**, *9* (11), 2493–2499.DOI: 10.1021/ic50093a023

(35) La- Placa, S. J.; Ibers, J. A. Five-Coordinated d^6 Coplex: Structure of Dichlorotris(Triphenylphosphine)Ruthenium (II). **1965**, *4* (6), 778–783. DOI: 10.1021/ic50028a002

(36) Brookhart, M.; Green, M. L. H. Carbon-Hydrogen-Transition Metal Bonds. *J. Organomet. Chem.* **1983**, *250* (1), 395–408. DOI: 10.1016/0022-328X(83)85065-7.

(37) Orlova, G.; Scheiner, S. Inter- and Intramolecular Hydrogen Bonds with Transition Metal Atoms in Metallocenes of the Iron Subgroup. *Organometallics* **1998**, *17* (20), 4362–4367. DOI: 10.1021/om9804881.

(38) Shubina, E. S.; Belkova, N. V.; Epstein, L. M. Novel Types of Hydrogen Bonding with Transition Metal π-Complexes and Hydrides. *J. Organomet. Chem.* **1997**, *536–537*, 17–29. DOI: 10.1016/S0022-328X(96)06791-5.

(39) Epstein, L. M.; Shubina, E. S. New Types of Hydrogen Bonding in Organometallic Chemistry. *Coord. Chem. Rev.* **2002**, *231* (1–2), 165–181. DOI: 10.1016/S0010-8545(02)00118-2.

(40) Borissova, A. O.; Antipin, M. Y.; Perekalin, D. S.; Lyssenko, K. A. Crucial Role of Ru···H Interactions in the Crystal Packing of Ruthenocene and Its Derivatives. *CrystEngComm* **2008**, *10* (7), 827–832. DOI: 10.1039/b716776h.

(41) Sundquist, W. I.; Bancroft, D. P.; Lippard, S. J. Synthesis, Characterization, and Biological Activity of Cis,-Diammineplatinum(II) Complexes of the DNA Intercalates 9-Aminoacridine and Chloroquine. *J. Am. Chem. Soc.* **1990**, *112* (4), 1590–1596. DOI: 10.1021/ja00160a044.

(42) Patyk-Kaźmierczak, E.; Warren, M. R.; Allan, D. R.; Katrusiak, A. Intermolecular Contacts in Compressed α- D- Mannose. *Cryst. Growth Des.* **2016**, *16* (12), 6885–6890. DOI: 10.1021/acs.cgd.6b01062.

(43) Paliwoda, D.; Szafrański, M.; Hanfland, M.; Katrusiak, A. A Giant 2-Dimensional Dielectric Response in a Compressed Hydrogen-Bonded Hybrid Organic-Inorganic Salt. *J. Mater. Chem. C* **2018**, *6* (28), 7689–7699. DOI: 10.1039/c8tc02464b.

(44) Anioła, M.; Katrusiak, A. Pressure-Preferred Symmetric Reactions of 4,4′-Bipyridine Hydrobromide. *CrystEngComm* **2016**, *18* (18), 3223–3228. DOI: 10.1039/c6ce00356g.

(45) Anioła, M.; Kwaśna, K.; Cai, W.; Katrusiak, A. High-Pressure Crystallizations of Meta-Dichlorobenzene and Dibromobenzene and Their Solid Solutions. *Cryst. Growth Des.* **2016**, *16* (11), 6304–6309. DOI: 10.1021/acs.cgd.6b00905.

(46) Podsiadło, M.; Olejniczak, A.; Katrusiak, A. Structure-Property Relations and Polymorphism in Compressed Methylamines. *Cryst. Growth Des.* **2017**, *17* (4), 2218–2222. DOI: 10.1021/acs.cgd.7b00203.

(47) Podsiadło, M.; Olejniczak, A.; Katrusiak, A. Halogen···halogen Contra C–H···halogen Interactions. *CrystEngComm* **2014**, *16* (35), 8279–8285. DOI: 10.1039/C4CE00241E.

(48) Półrolniczak, A.; Sobczak, S.; Katrusiak, A. Solid-State Associative Reactions and the Coordination Compression Mechanism. *Inorg. Chem.* **2018**, *57* (15), 8942–8950. DOI: 10.1021/acs.inorgchem.8b00913.

(49) Zielinski, W.; Katrusiak, A. Pressure-Induced Preference for Solvation of 5,6-Dimethylbenzimidazole. *CrystEngComm* **2016**, *18* (18), 3211–3215. DOI: 10.1039/c6ce00419a.

(50) Roszak, K.; Katrusiak, A. High-Pressure and Temperature Dependence of the Spontaneous Resolution of 1,1′-Binaphthyl Enantiomers. *Phys. Chem. Chem. Phys.* **2018**, *20* (7), 5305–5311. DOI: 10.1039/c7cp07234a.

(51) Zieliński, W.; Katrusiak, A. Hydrogen Bonds NH···N in Compressed Benzimidazole Polymorphs. *Cryst. Growth Des.* **2013**, *13* (2), 696–700. DOI: 10.1021/cg301374z.

(52) Roszak, K.; Katrusiek, A.; Katrusiak, A. High-Pressure Preference for the Low Z′ Polymorph of a Molecular Crystal. *Cryst. Growth Des.* **2016**, *16* (7), 3947–3953. DOI: 10.1021/acs.cgd.6b00521.

(53) Olejniczak, A.; Katrusiak, A.; Podsiadlo, M.; Katrusiak, A. Stochastic Hydration of a High-Nitrogen-Content Molecular Compound Recrystallized under Pressure. *IUCrJ* **2022**, *9*, 49–54. DOI: 10.1107/S2052252521010381.

(54) Olejniczak, A.; Katrusiak, A.; Szafrański, M. Ten Polymorphs of $NH^{+}\cdots N$ Hydrogen-Bonded 1,4-Diazabicyclo[2.2.2]Octane Complexes: Supramolecular Origin of Giant Anisotropic Dielectric Response in Polymorph V. *Cryst. Growth Des.* **2010**, *10* (8), 3537–3546. DOI: 10.1021/cg100455w.

(55) Rajewski, K. W.; Andrzejewski, M.; Katrusiak, A. Competition between Halogen and Hydrogen Bonds in Triiodoimidazole Polymorphs. *Cryst. Growth Des.* **2016**, *16* (7), 3869–3874. DOI: 10.1021/acs.cgd.6b00436.

(56) Rajewski, K. W.; Bukalska, I.; Katrusiak, A. Pressure-Induced High-to-Low Z ′ Phase Transition of a Conformationally Disordered Molecular Crystal. *Cryst. Growth Des.* **2018**, *18* (5), 3187–3192. DOI: 10.1021/acs.cgd.8b00282.

(57) Paliwoda, D.; Kowalska, K.; Hanfland, M.; Katrusiak, A. U-Turn Compression to a New Isostructural Ferrocene Phase. *J. Phys. Chem. Lett.* **2013**, *4* (23), 4032–4037. DOI: 10.1021/jz402254b.

(58) Bellin, C.; Mafety, A.; Narayana, C.; Giura, P.; Rousse, G.; Itié, J. P.; Polian, A.; Saitta, A. M.; Shukla, A. Disorder-Order Phase Transition at High Pressure in Ammonium Fluoride. *Phys. Rev. B* **2017**, *96* (9), 3–9. DOI: 10.1103/PhysRevB.96.094110.

(59) Dong, X.; Oganov, A. R.; Goncharov, A. F.; Stavrou, E.; Lobanov, S.; Saleh, G.; Qian, G. R.; Zhu, Q.; Gatti, C.; Deringer, V. L.; Dronskowski, R.; Zhou, X. F.; Prakapenka, V. B.; Konôpková, Z.; Popov, I. A.; Boldyrev, A. I.; Wang, H. T. A Stable Compound of Helium and Sodium at High Pressure. *Nat. Chem.* **2017**, *9* (5), 440–445. DOI: 10.1038/nchem.2716.

(60) Zhang, W.; Oganov, A. R.; Goncharov, A. F.; Zhu, Q.; Boulfelfel, S. E.; Lyakhov, A. O.; Stavrou, E.; Somayazulu, M.; Prakapenka, V. B.; Konôpková, Z. Unexpected Stable Stoichiometries of Sodium Chlorides. *Science* **2013**, *342* (6165), 1502–1505. DOI: 10.1126/science.1244989.

(61) Bhattacharyya, S.; Sobczak, S.; Półrolniczak, A.; Roy, S.; Samanta, D.; Katrusiak, A.; Maji, T. K. Dynamic Resolution of Piezosensitivity in Single Crystals of π-Conjugated Molecules. *Chem. - A Eur. J.* **2019**, *25* (24), 6092–6097. DOI: 10.1002/chem.201900054.

(62) Sobczak, S.; Półrolniczak, A.; Ratajczyk, P.; Cai, W.; Gładysiak, A.; Nikolayenko, V. I.; Castell, D. C.; Barbour, L. J.; Katrusiak, A. Large Negative Linear Compressibility of a Porous Molecular Co-Crystal. *Chem. Commun.* **2020**, *56* (31), 4324–4327. DOI: 10.1039/d0cc00461h.

(63) Cai, W.; Gładysiak, A.; Anioła, M.; Smith, V. J.; Barbour, L. J.; Katrusiak, A. Giant Negative Area Compressibility Tunable in a Soft Porous Framework Material. *J. Am. Chem. Soc.* **2015**, *137* (29), 9296–9301. DOI: 10.1021/jacs.5b03280.

(64) Hodgson, S. A.; Adamson, J.; Hunt, S. J.; Cliffe, M. J.; Cairns, A. B.; Thompson, A. L.; Tucker, M. J.; Funnell, N. P.; Goodwin, A. L. Negative Area Compressibility in Silver(i) Tricyanomethanide. *Chem. Commun.* **2014**, *50* (40), 5264–5266. DOI: 10.1039/c3cc47032f.

(65) Piermarini, G. J.; Block, S.; Barnett, J. D.; Forman, R. A. Calibration of the Pressure Dependence of the R 1 Ruby Fluorescence Line to 195 Kbar. *J. Appl. Phys.* **1975**, *46* (6), 2774–2780. DOI: 10.1063/1.321957.

(66) Moszczyńska, I.; Gulaczyk, I.; Katrusiak, A. Giant Deformation between Osmocene Phases Induced by Anagostic Bonds Promoted under High Pressure. *J. Phys. Chem. C* **2023**, *127* (38), 19250–19257. DOI: 10.1021/acs.jpcc.3c04579.

(67) Angel, R. J.; Bujak, M.; Zhao, J.; Gatta, G. D.; Jacobsen, S. D. Effective Hydrostatic Limits of Pressure Media for High-Pressure Crystallographic Studies. *J. Appl. Crystallogr.* **2007**, *40* (1), 26–32. DOI: 10.1107/S0021889806045523.

(68) Staško, D.; Prchal, J.; Klicpera, M.; Aoki, S.; Murata, K. Pressure Media for High Pressure Experiments, Daphne Oil 7000 Series. *High Press. Res.* **2020**, *40* (4), 525–536. DOI: 10.1080/08957959.2020.1825706.

(69) Dziubek, K. F.; Jęczmiński, D.; Katrusiak, A. Pressure-Generated Hydrogen Bonds and the Role of Subtle Molecular Features in Tetrahydrofuran. *J. Phys. Chem. Lett.* **2010**, *1* (5), 844–849. DOI: 10.1021/jz9003894.

(70) Budzianowski, A.; Katrusiak, A. High-Pressure Crystallography. *High-Pressure Crystallogr.* **2004**, No. February. DOI: 10.1007/978-1-4020-2102-2.

(71) Agilent. CrysAlisPro Software System. Technol. UK Ltd. Yarnton: Oxford, UK **2014**.

(72) Dolomanov, O. V.; Bourhis, L. J.; Gildea, R. J.; Howard, J. A. K.; Puschmann, H. OLEX2 : A Complete Structure Solution, Refinement and Analysis Program. *J. Appl. Crystallogr.* **2009**, *42* (2), 339–341. DOI: 10.1107/S0021889808042726.

(73) Sheldrick, G. M. Crystal Structure Refinement with SHELXL. *Acta Crystallogr. Sect. C Struct. Chem.* **2015**, *71* (Md), 3–8. DOI: 10.1107/S2053229614024218.

(74) Frisch, M. J.; Trucks, G. W.; Schlegel, H. B.; Scuseria, G. E.; Robb, M. A.; Cheeseman, J. R.; Scalmani, G.; Barone, V.; Petersson, G. A.; Nakatsuji, H.; Li, X.; Caricato, M.; Marenich, A. V.; Bloino, J.; Janesko, B. G.; Gomperts, R.; Mennucci, B.; Hratch, D. J. Gaussian 16, Revision C.01. Wallingford CT **2016**.

(75) Schuchardt, K. L.; Didier, B. T.; Elsethagen, T.; Sun, L.; Gurumoorthi, V.; Chase, J.; Li, J.; Windus, T. L. Basis Set Exchange: A Community Database for Computational Sciences. *J. Chem. Inf. Model.* **2007**, *47* (3), 1045–1052. DOI: 10.1021/ci600510j.

(76) Feller, D. The Role of Databases in Support of Computational Chemistry Calculations. *J. Comput. Chem.* **1996**, *17* (13), 1571–1586. DOI: 10.1002/(SICI)1096-987X(199610)17:13<1571::AID-JCC9>3.0.CO;2-P.

(77) Katrusiak, A.; Rusek, M.; Dušek, M.; Petříček, V.; Szafrański, M. Dipole-Moment Modulation in New Incommensurate Ferrocene. *J. Phys. Chem. Lett.* **2023**, *14* (13), 3111–3119. DOI: 10.1021/acs.jpclett.3c00215.

(78) Bermúdez-García, J. M.; Yáñez-Vilar, S.; Castro-García, S.; Señarís-Rodríguez, M. A.; Sánchez-Andújar, M. New Properties in Old Systems: Cooperative Electric Order in Ferrocene and Ammonia-Borane. *RSC Adv.* **2015**, *5* (102), 83818–83824. DOI: 10.1039/c5ra12506e.

(79) Macrae, C. F.; Sovago, I.; Cottrell, S. J.; Galek, P. T. A.; McCabe, P.; Pidcock, E.; Platings, M.; Shields, G. P.; Stevens, J. S.; Towler, M.; Wood, P. A. Mercury 4.0 : From Visualization to Analysis, Design and Prediction. *J. Appl. Crystallogr.* **2020**, *53* (1), 226–235. DOI: 10.1107/S1600576719014092.

(80) Katrusiak, A. Crystallographic Autostereograms. *J. Mol. Graph. Model.* **2001**, *19* (3–4), 363–367. DOI: 10.1016/S1093-3263(00)00085-1.

(81) Bondi, A. Van Der Waals Volumes and Radii. *J. Phys. Chem.* **1964**, *68* (3), 441–451.

DOI: 10.1021/j100785a001.

(82) Batsanov, S. S. Van Der Waals Radii of Elements. *Inorg. Mater.* **2001**, *37* (9), 871–885. DOI: 10.1023/A:1011625728803.

(83) Hu, S. Z.; Zhou, Z. H.; Robertson, B. E. Consistent Approaches to van Der Waals Radii for the Metallic Elements. *Z. fur Krist.* **2009**, *224* (8), 375–383. DOI: 10.1524/zkri.2009.1158.

(84) Kimel'fel'd, Y. M.; Smirnova, E. M.; Aleksanyan, V. T. The Vibrational Spectra of Molecular Crystals of Ferrocene, Ruthenocene, Osmocene and Nickelocene. *J. Mol. Struct.* **1973**, *19* (C), 329–346. DOI: 10.1016/0022-2860(73)85275-5.

(85) Parker, S. F.; Butler, I. R. Synthesis, Computational Studies, Inelastic Neutron Scattering, Infrared and Raman Spectroscopy of Ruthenocene. *Eur. J. Inorg. Chem.* **2019**, *2019* (8), 1142–1146. DOI: 10.1002/ejic.201800914.

ZAŁĄCZNIKI- KOPIE PUBLIKACJI NAUKOWYCH WCHODZĄCYCH W ZAKRES ROZPRAWY DOKTORSKIEJ

Artykuł 1

Ida Moszczyńska, Andrzej Katrusiak

Lattice-strain Coupled to Molecular Conformation and Disorder in Compressed Nickelocene
***J. Phys. Chem C,* 2021, *125 (28),* 15670-15675**

THE JOURNAL OF PHYSICAL CHEMISTRY C
A JOURNAL OF THE AMERICAN CHEMICAL SOCIETY

pubs.acs.org/JPCC

Article

Lattice-Strain Coupled to Molecular Conformation and Disorder in Compressed Nickelocene

Ida Moszczyńska and Andrzej Katrusiak*

Cite This: J. Phys. Chem. C 2021, 125, 15670−15675

Read Online

ACCESS | Metrics & More | Article Recommendations | Supporting Information

ABSTRACT: Isothermal compression of nickelocene ($NiCp_2$, where Cp denotes cyclopentadienyl ring $C_5H_5^-$) to 1.3 GPa leads to the ordered phase I′, highly isostructural with that obtained at 0.1 MPa by isobaric cooling to 170 K and with phase I′ of ferrocene ($FeCp_2$) above 3.24 GPa. However, the gradual ordering of Cp rings in $NiCp_2$ and its anomalous crystal strain considerably differs from that in $FeCp_2$. The disorder in $NiCp_2$ molecules can be represented as various combinations of achiral staggered and eclipsed conformers, as well as *R*-/*S*-rotamers, which are differently stabilized by the crystal environment. The anomalous lattice strain has been correlated with the molecular conformation, represented as the convolution of disordered Cp rings. The coincidence of the phase transition at 1.3 GPa/296 K with the monoclinic angle assuming 90° value does not occur on lowering temperature at 170 K/0.1 MPa, which is due to a weaker coupling between the lattice strain and the molecular disorder. Compared to $FeCp_2$, the energetic preference in $NiCp_2$ for the eclipsed conformation is lower and the stronger crystal field, favoring the staggered conformation. Therefore, phase I′ of $NiCp_2$ is stable below 170 K, while at 300 K $NiCp_2$ transforms to phase I′ at much lower pressure than $FeCp_2$.

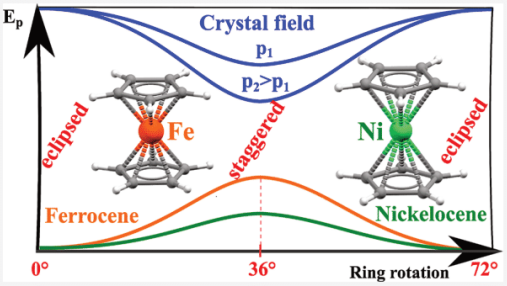

INTRODUCTION

Nickelocene ($NiCp_2$) and ferrocene ($FeCp_2$) are analogous sister sandwich compounds of similar properties and isostructural crystals at ambient conditions.[1,2] These are prototypic compounds for a wide family of metallocenes. At ambient conditions the crystals of $NiCp_2$ and $FeCp_2$ are monoclinic, of space group symmetry $P2_1/n$. Their crystal lattices are nearly identical, cations Ni^{2+} and Fe^{2+} lie on special positions, and the Cp rings are orientationally disordered. However, there are some differences in the disorder of Cp rings: in nickelocene two partly occupied sites are clearly distinguished (Figure 1), whereas for ferrocene two or three closer sites were postulated.[3,4] On lowering temperature, the conformation ordering in $FeCp_2$ occurs at the transition to triclinic phase II, and the next reconstructive transition to orthorhombic phase III leads to the D_{5h}-symmetric eclipsed conformers,[5,6] while in $NiCp_2$ the Cp rings order gradually, between 240 and 170 K,[7] into the D_{5d}-symmetric staggered conformers, within the same crystal lattice.[8] Braga and Grepioni suggested that this low-temperature behavior of nickelocene arises from a short intermolecular distance H···H and their repulsion, which results in the negative thermal expansion of the crystal along its [*y*] axis.[9] In another study on nickelocene and ferrocene, the hindering of rotations of the Cp rings was associated with short H···H intermolecular contacts, too.[10] Electron-diffraction studies on gaseous nickelocene revealed that Cp rings vibrate with larger amplitudes than in ferrocene.[11] More recently, the energetic characteristics of the conformational dynamics in $NiCp_2$ and $FeCp_2$ were studied by quasielastic neutron scattering.[12] Presently, we have investigated the crystal strain and molecular conformations in $NiCp_2$ as a function of pressure and temperature and we have compared them to those in $FeCp_2$.

The high-pressure ordered structure of ferrocene above 3.24 GPa[13] was labeled as phase I′. It was established that the transition between ferrocene phases I and I′ coincides with the 90° opening of monoclinic angle β (of the lattice symmetry described by space group $P2_1/n$). The coincidence of the β value of 90° with the discontinuous strain in ferrocene at the critical pressure of the isostructural transition to phase I′, although the system remains monoclinic, is remarkable. Another aim of this study was to check if the coincidence of the orthogonal lattice with the transition point is specific for ferrocene, or if it is a more general requirement and it occurs in nickelocene, too. For the equivalent descriptions of the crystal structures in space group $P2_1/a$, often used in the literature,[8,14] the monoclinic β angles are 121.42(6)° in nickelocene and 121.02° in ferrocene (at ambient conditions); for this choice of

Received: May 12, 2021
Revised: June 19, 2021
Published: July 9, 2021

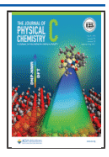

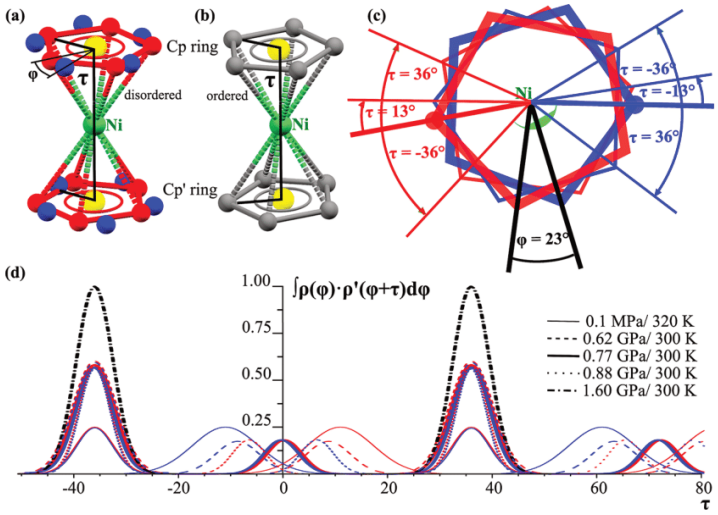

Figure 1. Nickelocene molecule (H atoms skipped for clarity): (a) in disordered phase I, with the partly occupied sites of Cp rings (marked red and blue) displaced in one plane by angle $\varphi = 23°$ at 0.1 MPa/296 K; (b) staggered D_{5h}-symmetric ordered conformer above 1.3 GPa/296 K in phase I′; (c) the molecule viewed down its D_5 axis, with indicated torsion angle τ between the Cp rings (closer, thick lines; further, thin lines), as well as angle φ between two partly occupied sites of one disordered Cp ring. (d) Pressure-induced evolution of conformers, represented as the convolution of electron-density distribution ρ (in ring Cp) and ρ' (in ring Cp′), scaled to 1 for the fully ordered rings displaced by angle $\tau = 36°$ (cf. Figures S1 and S2 in the Supporting Information).

the unit cell, the transition between ferrocene phases I and I′ occurs at angle β equal to 124.16(1)°. Therefore, we have chosen space group $P2_1/n$ for describing the symmetry of ferrocene and nickelocene phases I and I′.

METHODS

For high-pressure experiments we used a Merrill−Bassett diamond-anvil cell (DAC) modified by mounting the diamonds directly on the steel disks with conical windows.[15] Two hydrostatic media, Daphne oil 7474 and the methanol/ethanol (4:1) mixture, were used for isothermally compressing the sample to 3.43 and 3.7 GPa, respectively. The $NiCp_2$ single crystal was mounted in the DAC in the glovebox filled with argon, in order to secure dry and oxygen-free atmosphere. The pressure inside the DAC was calibrated by the ruby fluorescence method,[16] with a Photon Control spectrometer with enhanced resolution affording the 0.02 GPa accuracy. Each time after increasing pressure, the single-crystal X-ray diffraction data were measured with diffractometer Excalibur EOS or KUMA KM-4 CCD, both employing the MoKα radiation. Data collections and their reductions were performed with program CrysAlisPro from Oxford Diffraction. The DAC absorption, sample shadowing by the gasket, and the sample absorption were corrected,[17,18] and the diamond reflections were eliminated. The crystal structure at ambient conditions was solved by direct methods of Shelxs and refined by full-matrix least-squares on F^2 by Shelxl,[19] operated through Olex 2.[20] Then this structure was used as a starting model for higher-pressure experiments. The Cp rings (two partially occupied in phase I and one ordered in phase I′) were constrained to an ideal pentagon with H atoms at 0.93 Å from their C atoms. Analogous procedures were applied for low-temperature measurements, but the single crystal was mounted on a nylon loop and an Oxford Cryostream attachment and the Excalibur EOS diffractometer were used. The site occupation factor (SOF) for the Cp ring disordered in two positions 1 and 2 was constrained by the condition SOF1 + SOF2 = 1. The crystallographic data of $NiCp_2$ phases are summarized in Table S1 in the Supporting Information. Experimental and structural details have been deposited in the Cambridge Crystallographic Database Centre as supporting publications with numbers CCDC 2080130−2080157. Their copies can be obtained free of change from www.ccdc.cam.ac.uk.

RESULTS AND DISCUSSION

Molecular Conformation. The phase transitions in $FeCp_2$ clearly show that they are coupled to the conformational transformations of molecules.[2,5,6,13,21] The conformational disorder has been connected with the thermal expansion of nickelocene crystals,[7,8,22] too. However, there are inconsistencies in the energetic description of conformational preferences of the isolated $NiCp_2$ molecule and of the molecule in the crystal. It was established, by electron diffraction in the gas phase,[23] that the eclipsed conformation of an isolated molecule of nickelocene is more favored, by ΔE_p of about 4 kJ·mol^{-1}, than the staggered conformation.[11,23] On the other hand, the energetic preference for the eclipsed conformation of $NiCp_2$ molecules was described as twice smaller than that in ferrocene,[22] determined by theoretical calculations as 4 kJ·mol^{-1}. This E_p preference for the eclipsed conformation of $FeCp_2$ molecules agrees well with the value 3.8 ± 1.3 kJ·mol^{-1} measured by electron diffraction in the gas phase.[24] Incoherent quasi-elastic neutron scattering experiments on solid samples show that the activation energy of Cp ring reorientation in nickelocene equals 6.3 kJ·mol^{-1},[25] while in ferrocene average activation energy equals 9.6 kJ·mol^{-1}.[12] The lower activation energy of the Cp rotations in $NiCp_2$ is consistent with its pressure value of transition to phase I′, measured in our present study, about twice lower than that in $FeCp_2$.[13]

At ambient conditions in nickelocene, the distribution of disordered atoms in the Cp rings corresponds to the superposition of three conformations: the staggered con-

https://doi.org/10.1021/acs.jpcc.1c04204
J. Phys. Chem. C 2021, 125, 15670−15675

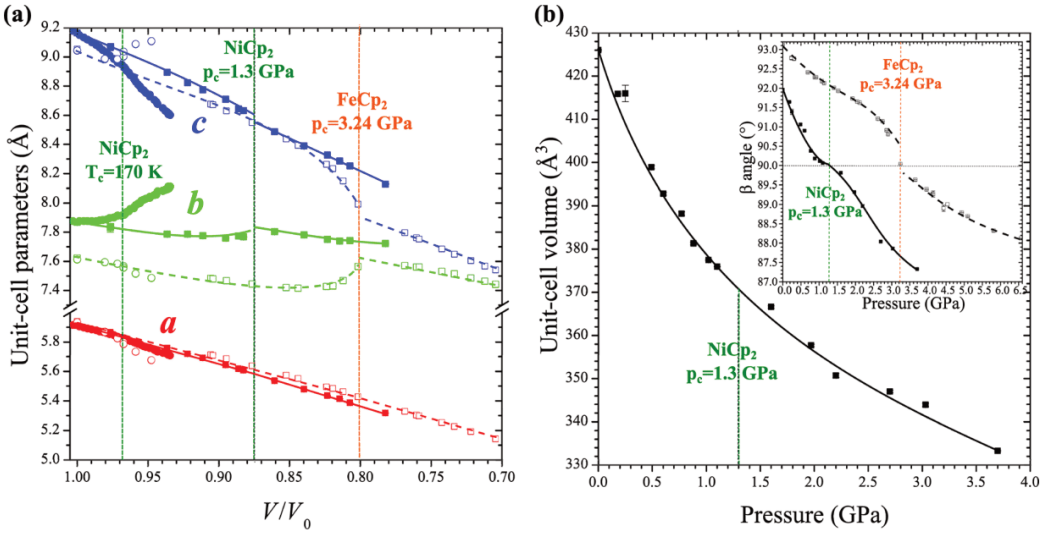

Figure 2. (a) Unit-cell parameters of nickelocene (full symbols, this work and ref 7) and ferrocene (empty symbols, refs 2, 13, and 24) as a function of relative volume. Squares and cycles refer to the pressure and temperature changes. (b) Volume compression of nickelocene; the inset compares the pressure dependence of angle β for nickelocene (full symbols) and ferrocene (empty symbols). Where not indicated, the estimated standard deviations are smaller than the plotted symbols.

formation (with angle $\tau = 36°$) as well as the *R*- and *S*-rotamers with the Cp rings twisted by angle $\tau = \pm 13°$, respectively, and populated as shown in Figure 1. A similar model was described for ferrocene but with the φ and τ angles equal to 25° and ±11°, respectively.[3,12] The dynamics of intramolecular disorder in $NiCp_2$ and $FeCp_2$ crystals was extensively studied by IR and Raman spectroscopy and quasi-elastic neutron spectroscopy.[22,26] In those studies both the activation energies of internal rotations and the reorientations of rigid molecules in the crystal field were considered.

Lattice Strain. The pressure dependence of unit-cell dimensions of $NiCp_2$ is anomalous around 1.3 GPa (Figure 2). These anomalies are less pronounced than those in $FeCp_2$ (cf. Figures S3 and S4 in the Supporting Information). As shown below, the anomalous lattice strain in $NiCp_2$ correlates with the ordering of Cp rings in the structure (Figure 1). According to the literature[7,8,22] and to our structural high-pressure determinations based on single-crystal X-ray diffraction measurements, the $NiCp_2$ molecules are conformationally disordered at ambient conditions. The disorder gradually disappears with increasing pressure, and it is fully eliminated about 1.3 GPa (Figure S5 in the Supporting Information). This magnitude of pressure coincides with a small downward kink in compression of unit-cell parameter *c*, a small upward kink in parameter *b*, and a subtle decrease in compressibility of parameter *a* ($\beta_a = (1/a)\cdot da/dp$ is 0.049 GPa^{-1} below 1.3 GPa and above it decreases to 0.016 GPa^{-1}). Although the kinks in the compression of *b* and *c* are small, they are analogous in shape and curvature to the more apparent anomalies in ferrocene. For example, on approaching the transition by increasing pressure, the anomalies in *b* are concave and those in *c* are convex.

The anomaly in the pressure dependence of monoclinic angle β of nickelocene at 1.3 GPa coincides with the right angle (90°). Below 1.3 GPa function $\beta(p)$ is concave and above 1.3 GPa this function is convex, so the transition through 90° coincides with the concave-to-convex inflection point. The analogous transition between phases I and I′ in ferrocene at 3.24 GPa is accompanied by an inflection point in function $\beta(p)$ coinciding with the right angle, too. However, in ferrocene at 90° there is a clear discontinuity in $\beta(p)$, not detected in nickelocene, and the curvature of function $\beta(p)$ changes from convex to concave in the sequence opposite to that in nickelocene.

The pressure dependence of angle β in nickelocene can be compared to its temperature dependence, plotted in Figure 3 (cf. Figure S6 in Supporting Information). The pressure and temperature dependences of β follow the inverse relationship

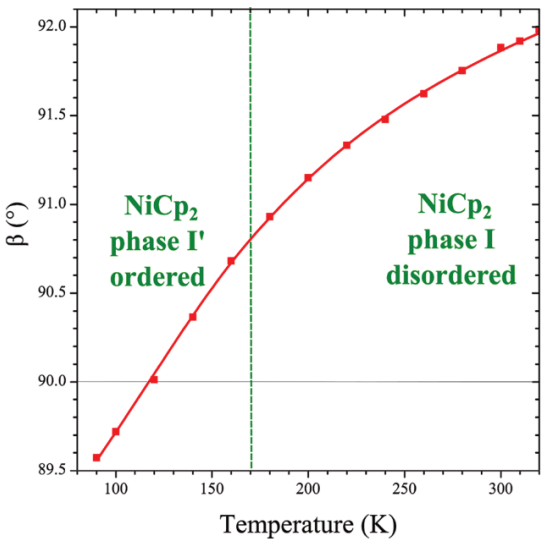

Figure 3. Monoclinic angle β in nickelocene plotted as a function of temperature. The vertical dashed line indicates the temperature of full ordering of the Cp rings (cf. Figure S6 in Supporting Information).

https://doi.org/10.1021/acs.jpcc.1c04204
J. Phys. Chem. C 2021, 125, 15670−15675

rule:[27] the cooling and compression reduce the β values. Indeed, between 320 and 90 K the β angle decreases from 91.98° to 89.57°; a similar change in β is induced by the pressure of about 2 GPa. In both cooled and compressed structures the β angle passes through the value of 90°, but in the $\beta(p)$ function it corresponds to the clearly marked inflection point, which is hardly visible for $\beta(T)$. Another significant difference is that $\beta(T)$ crosses the 90° value at 120 K, well below the temperature when the Cp rings order; in other words the β(120 K) = 90° does not correspond to the transition between phases I and I′ (Figure 3). Thus, the $\beta(T)$ function in nickelocene cannot be straightforwardly connected with the order−disorder transition, which is apparent for the $\beta(p)$ functions for both nickelocene and ferrocene.

Molecular Disorder. At 320 K/0.1 MPa the disorder of $NiCp_2$ molecules can be described as a coexistence of the staggered conformation (torsion angle τ = 36°; see Figure 1) with two rotamers with τ equal to either +11° or −11°. The staggered conformation is populated in 50%, rotamer *R* in 25%, and rotamer *S* in 25%, when each of the Cp rings is disordered in two equally occupied sites (cf. Figure 1). With increasing pressure, the population of the staggered conformation gradually increases and at 1.3 GPa it riches the full occupation, while the rotamers gradually disappear (Figure 4).

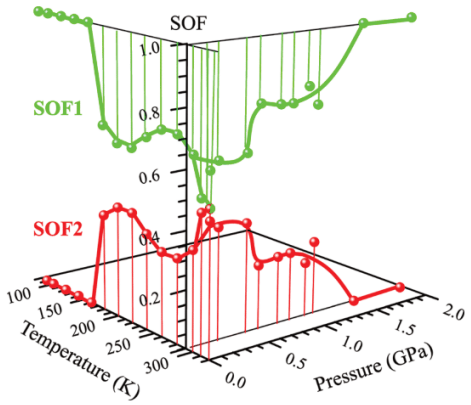

Figure 4. Site-occupation factors (SOF's) of the Cp ring in nickelocene plotted as a function of temperature and pressure. The prevailing SOF1 (green, close to the average ring position in ferrocene phases I and I′) and SOF2 become equal to 0.5 at 320 K/0.1 MPa.

When the Cp rings gradually order, the angular displacement of the disordered sites, measured by angle φ, increases from 23.5° at 0.1 MPa to 45.5° at 1.1 GPa (Figure 5). It means that at about 0.77 GPa there is about 40% of the eclipsed conformers and no *R*- or *S*-rotamers. At still higher pressure the *R*- and *S*-rotamers are formed again (when angle φ exceeds 36°). Our analysis of intermolecular contacts (cf. the Figures S7 and S8 in Supporting Information) shows that there is a steric hindrance due to the interactions between atoms H3A of neighboring molecules, culminating with the closest distance of 2.279 Å at 0.77 GPa. Nickelocene displays analogous behavior as a function of temperature, when on cooling to 270 K angle φ assumes 36° for the SOF1 = 0.7 and SOF2 = 0.3, corresponding to the mixture of staggered and eclipsed conformers. At still lower temperature the φ angle becomes larger than 36° (like above 0.77 GPa) and the conformations of rotamers are assumed again (Figure 5).

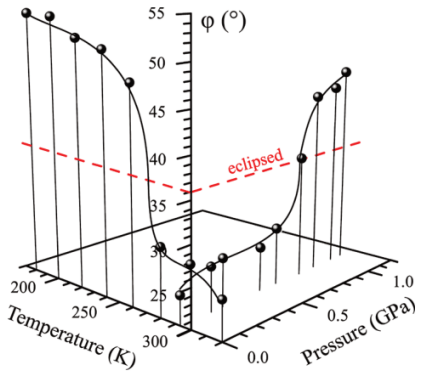

Figure 5. Pressure and temperature dependence of angle φ (cf. Figure 1) measuring the displacement between the sites of the disordered Cp ring in nickelocene. The red dashed line indicates the φ angle value of 36° when the molecule is composed of the staggered and eclipsed conformers between Cp rings disordered in ratio SOF1/SOF2. (cf. Figure S9 in Supporting Information).

Molecular Orientation. At 300 K and 0.1 MPa the two sites of one disordered Cp ring are not exactly parallel to each other, but they are inclined by about 1°. This inclination angle significantly increases with pressure to 13° at 1.1 GPa, which results from the increased interactions with the crystal environment differentiating two disordered orientations. The crystal packing forces and the orientation of ordered $NiCp_2$ molecules are interdependent, in a very similar way to those in the crystal of ferrocene phases I and I′.

In order to understand the strain differences between nickelocene and ferrocene, we have investigated the molecular orientations with respect to the crystal lattice as a function of pressure (Figure S10 in the Supporting Information). For this purpose we have applied four angles, three of them for measuring the orientation of the molecular C_5-axis with respect to crystal directions *x*, *y*, and *z*; these angles have been denoted as ψ_x, ψ_y, and ψ_z, respectively. The fourth angle, denoted χ, measures the orientation of the Cp ring, here defined as the torsion angle between atom C1, the Cp ring centroid, atoms Ni and Ni′ at *x*, *y* + 1, *z*.

The χ angle can be calculated in several ways. For nickelocene we have chosen the average of two disordered sites for each atom. This method of calculating χ has been used because we intended to compare the structure of nickelocene with ferrocene, where disordered atomic sites are closely located and in most experiments one average atomic position is reported.[13,21] This method of calculation gives for nickelocene the χ values scattered by about ±5° about 30° for the pressure range below 1.3 GPa, but above 1.3 GPa they are consistent and increase from 31° at 1.5 GPa to 33.5° at 3.7 GPa. The strongest changes in the orientation of $NiCp_2$ molecules take place in the pressure range of phase I. Then at about 1.3 GPa the changes of angles ψ_x, ψ_y, ψ_z, and χ are stepwise, and under still higher pressure within phase I′ all these angles become similar to those in $FeCp_2$ phase I′. In both $NiCp_2$ and $FeCp_2$ the strongest changes occurred in angles χ and ψ_y. These analogies can be interpreted as the indication of the similarly significant role of close-packing and molecular-environment effects in $NiCp_2$ and $FeCp_2$. Furthermore, the different orientations of the C_5 axes of the disordered sites affect the

https://doi.org/10.1021/acs.jpcc.1c04204
J. Phys. Chem. C 2021, 125, 15670−15675

convolution of conformers, for which ideally superimposed axes were assumed.

Phase Diagram. The $p-T$ phase diagram of nickelocene outlined in Figure 6, within the investigated range of pressure

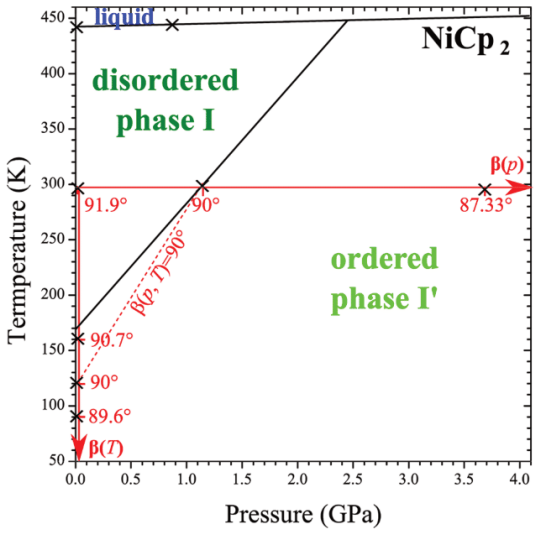

Figure 6. Phase diagram of nickelocene based on the isobaric study at 0.1 MPa between 90 and 320 K, isothermal compression at 296 K up to 3.5 GPa, and optical observations of the crystal melting in a heated DAC. Selected measurements and observation points are marked with crosses, and the pressure boundaries are estimated between these points. Red lines and values indicate the changes of monoclinic angle β as a function of temperature and pressure.

and temperature, contains two solid-state regions denoted as disordered phase I and ordered phase I′. Both they are analogous to phases I and I′ of ferrocene.[13] Like in ferrocene, the boundary between these phases has been associated with the anomalies in the lattice strain, which coincide with the full ordering of the Cp rings. In this $p-T$ phase diagram also selected values of the monoclinic angle β have been indicated for the isothermal compression $\beta(296\ \mathrm{K}, p)$ and isobaric cooling $\beta(T, 0.1\ \mathrm{MPa})$, shown in Figures 2 and 3. It appears that the line tracing the right angle $\beta(T,p) = 90°$ coincides with the boundary between phases I and I′, but at 0.1 MPa angle β becomes equal to 90° at 120 K, i.e., about 50 K below the boundary. It suggests that below 296 K and 1.3 GPa the isostructural transition between phases I and I′ can become diffused and the characteristic features of the transition can be separated.

The liquid−solid transition boundary for nickelocene has been based on the microscopic observations of the crystal melting in the DAC. The ambient-pressure melting points of $NiCp_2$ and $FeCp_2$ are very similar, 444 and 445 K, respectively.

CONCLUSIONS

At 296 K, above 1.3 GPa the crystal structure of nickelocene gradually orders. The disordered and ordered regions of the phase diagram of nickelocene are separated by a zone of anomalous thermal expansion and compression. The ordered and disordered regions have been assigned as phases I and I′. Phase I′ of nickelocene is isostructural to the ordered ferrocene phase I′ above 3.24 GPa. Many structural features of phase I′ of these two compounds are nearly identical. However, there are several distinct features of nickelocene and ferrocene in their disordered phase I: (i) the unit-cell parameter b in nickelocene is around 0.2 Å longer than in ferrocene, and its anomalous negative linear compressibility before the transition to phase I′ is manifested weaker in $NiCp_2$ than in $FeCp_2$; (ii) at 0.1 MPa the intramolecular Cp···Cp distance in nickelocene (3.584 Å) is longer than that in ferrocene (3.274 Å); (iii) the shortest intermolecular H···H contacts in nickelocene (2.29 Å) are shorter compared to ferrocene (2.40 Å). All these structural features are consistent with the lower energy difference between the eclipsed and staggered conformers and with the pressure needed to eliminate nonstaggered conformers in the crystal of nickelocene over twice lower than in ferrocene. The weaker intramolecular energetic preference for the eclipsed conformation and the stronger crystal field favoring the staggered conformation combine in nickelocene and strongly promote the fully ordered phase I′ below 170 K. By the way of contrast, the stronger preference for the eclipsed conformation and weaker crystal field in ferrocene phase I are the reasons for the transitions leading to phase III with eclipsed conformers in low temperature. Increased pressure enhances the crystal field favoring the staggered conformers, which at 296 K fully prevails above 3.24 GPa in ferrocene, compared to 1.3 GPa in nickelocene, consistent with its lower preference for the eclipsed conformation. The pressure-induced isostructural transition between nickelocene phases I and I′ is associated with the monoclinic angle β passing through 90°; however this is not the case when phase I′ is entered by lowering the temperature below 170 K. This lack of coincidence between the transition temperature and the right angle β may be due to weak intermolecular interactions at 0.1 MPa, resulting in weak coupling between the conformational disorder and the crystal strain. Further studies are clearly needed for better understanding the coincidence of the disorder decay and monoclinic angle β assuming 90° under high pressure and the departure from this coincidence in the cooled sample at 0.1 MPa. Our study clearly shows that the stronger effect of the crystal field and weaker preference of the $NiCp_2$ molecules for the eclipsed conformation result in the stabilized staggered conformers in the crystal contacted at 170 K. In ferrocene, due to its stronger preference for eclipsed conformers and weaker centrosymmetric crystal field, a sequence of phase transitions lead to phase III with the eclipsed molecules. Both nickelocene and ferrocene crystals display unique features due to the coupling between the lattice strain with the disorder and molecular conformation. The effects of molecular conformation on the phase transformations are quite common, and such phenomena are important for the properties of various materials.[28−31]

ASSOCIATED CONTENT

Supporting Information

The Supporting Information is available free of charge at https://pubs.acs.org/doi/10.1021/acs.jpcc.1c04204.

Crystallographic data, projection of nickelocene molecule with indicated τ-conformation and φ-disordered-sites displacement angles, distribution of electron density at pressure, compression of unit-cell parameters, monoclinic β angle changes as a function of pressure for nickelocene and ferrocene, order parameter plot, atomic displacement parameters, τ and φ correlation, description of molecule orientation, H3···H3 shortest

https://doi.org/10.1021/acs.jpcc.1c04204
J. Phys. Chem. C 2021, 125, 15670−15675

contacts analysis, site-occupation factors analysis, φ angle analysis, monoclinic $\beta(T)$ in nickelocene based on data from ref 7, populations of staggered and eclipsed conformers for the disorder displacement angle $\varphi = 36°$ (PDF)

AUTHOR INFORMATION

Corresponding Author

Andrzej Katrusiak − *Department of Materials Chemistry, Faculty of Chemistry, Adam Mickiewicz University, 61-614 Poznań, Poland;* orcid.org/0000-0002-1439-7278; Phone: +48 61 829 1590; Email: katran@amu.edu.pl

Author

Ida Moszczyńska − *Department of Materials Chemistry, Faculty of Chemistry, Adam Mickiewicz University, 61-614 Poznań, Poland;* orcid.org/0000-0002-0791-2278

Complete contact information is available at: https://pubs.acs.org/10.1021/acs.jpcc.1c04204

Author Contributions

The manuscript was written through contributions of all authors. All authors have given approval to the final version of the manuscript.

Notes

The authors declare no competing financial interest.

ACKNOWLEDGMENTS

This study was supported by the Polish Ministry of Higher Education.

REFERENCES

(1) Pfab, W.; Fischer, E. O. Zur Kristallstruktur Der Di-cyclo-pentadienyl-verbindungen Des Zweiwertigen Eisens, Kobalts Und Nickels. *Z. Anorg. Allg. Chem.* **1953**, *274*, 316−322.

(2) Calvarin, G.; Berar, J. F. Etude Par Diffraction Des Rayons X Sur Poudre de La Transition Ordre−Désordre Du Ferrocène $Fe(C_5H_5)_2$. *J. Appl. Crystallogr.* **1975**, *8*, 380−385.

(3) Brock, C. P.; Fu, Y. Rigid-Body Disorder Models for the High-Temperature Phase of Ferrocene. *Acta Crystallogr., Sect. B: Struct. Sci.* **1997**, *53*, 928−938.

(4) Takusagawa, F.; Koetzle, T. F. A Neutron Diffraction Study of the Crystal Structure of Ferrocene. *Acta Crystallogr., Sect. B: Struct. Crystallogr. Cryst. Chem.* **1979**, *35*, 1074−1081.

(5) Seiler, P.; Dunitz, J. D. The Structure of Triclinic Ferrocene at 101, 123 and 148 K. *Acta Crystallogr., Sect. B: Struct. Crystallogr. Cryst. Chem.* **1979**, *35*, 2020−2032.

(6) Seiler, P.; Dunitz, J. D. Low-Temperature Crystallization of Orthorhombic Ferrocene: Structure Analysis at 98 K. *Acta Crystallogr., Sect. B: Struct. Crystallogr. Cryst. Chem.* **1982**, *38*, 1741−1745.

(7) Calvarin, G.; Weigel, D. Mise En Évidence et Étude, Par Diffraction Des Rayons X Sur Poudre, d'une Transition Ordre−Désordre Pour Le Nickelocène $Ni(C_5H_5)_2$. *J. Appl. Crystallogr.* **1976**, *9*, 212−215.

(8) Seiler, P.; Dunitz, J. D. The Structure of Nickelocene at Room Temperature and at 101 K. *Acta Crystallogr., Sect. B: Struct. Crystallogr. Cryst. Chem.* **1980**, *36*, 2255−2260.

(9) Braga, D.; Grepioni, F. Crystal Construction and Molecular Interplay in Solid Ferrocene, Nickelocene, and Ruthenocene. *Organometallics* **1992**, *11*, 711−718.

(10) Levendis, D. C.; Boeyens, J. C. A. Analysis of the Molecular Conformation and Rotational Disorder in Crystalline Ferrocene and Nickelocene. *J. Crystallogr. Spectrosc. Res.* **1985**, *15*, 1−17.

(11) Hedberg, L.; Hedberg, K. Molecular Structure of Dicyclo-pentadienylnickel $(C_5H_5)_2Ni$. *J. Chem. Phys.* **1970**, *53*, 1228−1234.

(12) Appel, M.; Frick, B.; Spehr, T. L.; Stühn, B. Molecular Ring Rotation in Solid Ferrocene Revisited. *J. Chem. Phys.* **2015**, *142*, 114503.

(13) Paliwoda, D.; Kowalska, K.; Hanfland, M.; Katrusiak, A. U-Turn Compression to a New Isostructural Ferrocene Phase. *J. Phys. Chem. Lett.* **2013**, *4*, 4032−4037.

(14) Dunitz, J. D.; Orgel, L. E.; Rich, A. The Crystal Structure of Ferrocene. *Acta Crystallogr.* **1956**, *9*, 373−375.

(15) Merrill, L.; Bassett, W. A. Miniature Diamond Anvil Pressure Cell for Single Crystal X-ray Diffraction Studies. *Rev. Sci. Instrum.* **1974**, *45*, 290−294.

(16) Piermarini, G. J.; Block, S.; Barnett, J. D.; Forman, R. A. Calibration of the Pressure Dependence of the R 1 Ruby Fluorescence Line to 195 Kbar. *J. Appl. Phys.* **1975**, *46*, 2774−2780.

(17) Katrusiak, A. Shadowing and Absorption Corrections of Single-Crystal High-Pressure Data. *Z. Kristallogr. - Cryst. Mater.* **2004**, *219*, 461−467.

(18) Budzianowski, A.; Katrusiak, A. High-Pressure Crystallographic Experiments with a CCD-Detector. In *High-Pressure Crystallography*; Springer: Dordrecht, The Netherlands, 2004; DOI: 10.1007/978-1-4020-2102-2_7.

(19) Sheldrick, G. M. Crystal Structure Refinement with SHELXL. *Acta Crystallogr., Sect. C: Struct. Chem.* **2015**, *71*, 3−8.

(20) Dolomanov, O. V.; Bourhis, L. J.; Gildea, R. J.; Howard, J. A. K.; Puschmann, H. OLEX2 : A Complete Structure Solution, Refinement and Analysis Program. *J. Appl. Crystallogr.* **2009**, *42*, 339−341.

(21) Paliwoda, D.; Hanfland, M.; Katrusiak, A. Pressure-Enhanced Environment Effects in Ferrocene Phases. *J. Phys. Chem. C* **2019**, *123*, 25719−25723.

(22) Chhor, K.; Lucazeau, G.; Sourisseau, C. Vibrational Study of the Dynamic Disorder in Nickelocene and Ferrocene Crystals. *J. Raman Spectrosc.* **1981**, *11*, 183−198.

(23) Ronova, I. A.; Bochvar, D. A.; Chistjakov, A. L.; Struchkov, Y. T.; Alekseev, N. V. Electron Diffraction Study in the Vapour Phase of the Molecular Structure of Dicyclopentadienylnickel. *J. Organomet. Chem.* **1969**, *18*, 337−344.

(24) Haaland, A.; Nilsson, J. E.; Olson, T.; Norin, T. The Determination of Barriers to Internal Rotation by Means of Electron Diffraction. Ferrocene and Ruthenocene. *Acta Chem. Scand.* **1968**, *22*, 2653−2670.

(25) Sourisseau, C.; Lucazeau, G.; Dianoux, A. J.; Poinsignon, C. Neutron Scattering Study of the Reorientational Motions in $Ni(C_5H_5)_2$. *Mol. Phys.* **1983**, *48*, 367−377.

(26) Gardner, A. B.; Howard, S.; Waddington, T. C.; Richardson, R. M.; Tomkinson, J. The Dynamics of Ring Rotation in Ferrocene, Nickelocene and Ruthenocene by Incoherent Quadi-Elastic Neutron Scattering. *Chem. Phys.* **1981**, *57*, 453−460.

(27) Hazen, R. M.; Finger, L. W. *Comparative Crystal Chemistry. Temperature, Pressure, Composition and Variation of the Crystal Structure*; John Wiley: New York, 1982.

(28) Cailleau, H.; Baudour, J. L.; Meinnel, J.; Dworkin, A.; Moussa, F.; Zeyen, C. M. E. Double-Well Potentials and Structural Phase Transitions in Polyphenyls. *Faraday Discuss. Chem. Soc.* **1980**, *69*, 7−18.

(29) Cai, W.; Katrusiak, A. Conformationally Assisted Negative Area Compression in Methyl Benzoate. *J. Phys. Chem. C* **2013**, *117*, 21460−21465.

(30) Byrn, S. R.; Curtin, D. Y.; Paul, I. C. The X-Ray Crystal Structures of the Yellow and White Forms of Dimethyl 3,6-Dichloro-2,5-Dihydroxyterephthalate and a Study of the Conversion of the Yellow Form to the White Form in the Solid State. *J. Am. Chem. Soc.* **1972**, *94* (3), 890−898.

(31) Nangia, A. Conformational Polymorphism in Organic Crystals. *Acc. Chem. Res.* **2008**, *41*, 595−604.

Artykuł 2

Ida Moszczyńska, Damian Paliwoda, Andrzej Katrusiak

Pressure-Tuned Conformers and Their Populations in Ferrocene
***J. Phys. Chem. C*, 2024, *128 (45)*, 19392-19397**

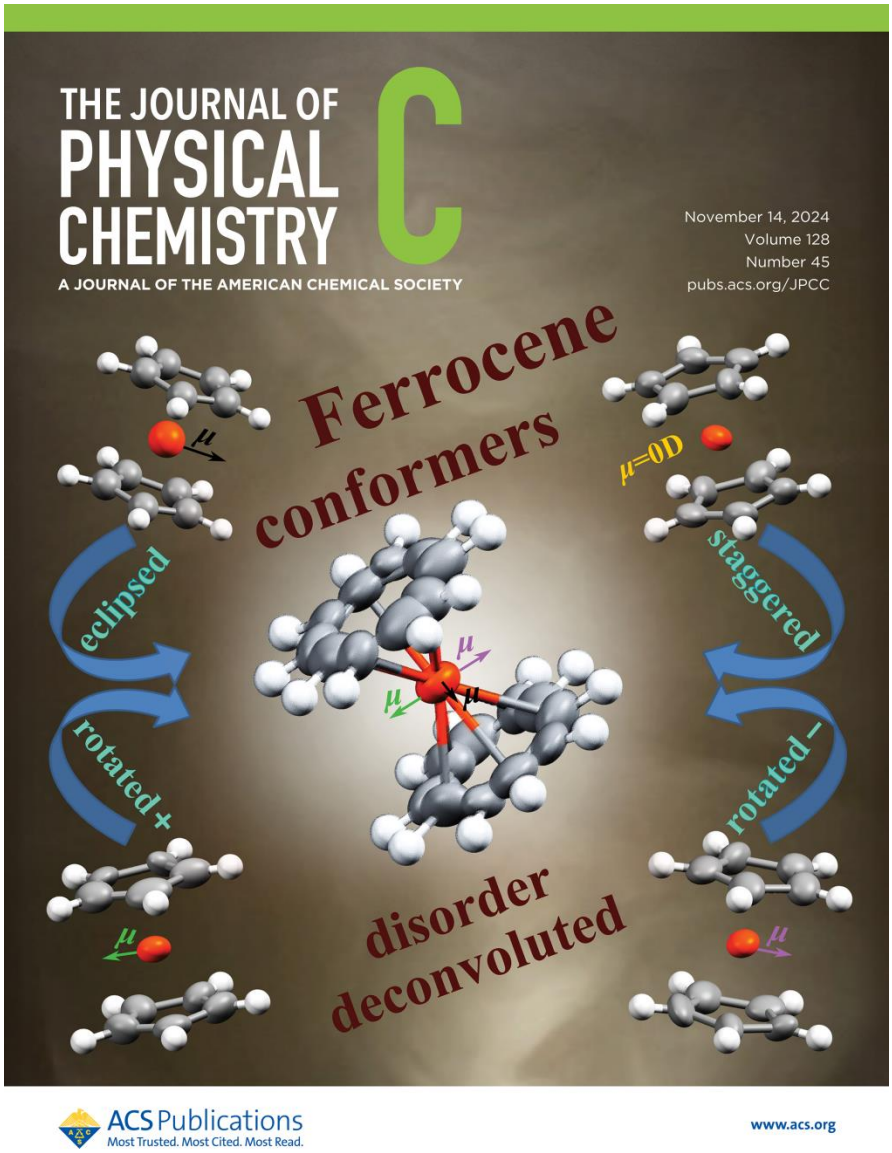

THE JOURNAL OF PHYSICAL CHEMISTRY C
A JOURNAL OF THE AMERICAN CHEMICAL SOCIETY

pubs.acs.org/JPCC
Article

Pressure-Tuned Conformers and Their Populations in Ferrocene

Ida Moszczyńska, Damian Paliwoda, and Andrzej Katrusiak*

Cite This: J. Phys. Chem. C 2024, 128, 19392−19397
Read Online

ACCESS | Metrics & More | Article Recommendations | Supporting Information

ABSTRACT: In ferrocene ($FeCp_2$, Cp is $C_5H_5^-$), the dynamically disordered cyclopentadienyl rings (Cp) result in a distribution of staggered, rotated (axially chiral), and eclipsed conformations, strongly affected by pressure. Under normal conditions, about 54% of the molecules are staggered, 23% are rotated left, and 23% are rotated right, whereas at 2.2 GPa, the population of staggered conformers is 69% and that of eclipsed ones is 31%, while the rotated conformers are absent. The monotonic compression of phase I at 293 K gradually modifies the disorder angle between the Cp-ring sites about the pseudo-D_5 axis and site-occupation factors (SOFs). In the population of rotated conformers, the twisting angle gradually changes between ±8° at 0.1 MPa, ±13° at 1.5 GPa, 0° (the eclipsed conformer) at 2.2 GPa, and 36° (the staggered conformer) at 3.24 GPa when phase I isostructurally transforms to the ordered phase I′, built exclusively of the staggered conformers. The structural models of ferrocene phase I have been refined *de novo* on high-pressure synchrotron X-ray diffraction data, and the molecular conformation has been described as a convolution of the sites of disordered Cp rings. The disordered Cp-ring sites are displaced, which generates a molecular dipole moment for the rotated and eclipsed conformers, consistent with the dielectric response of the ferrocene crystals.

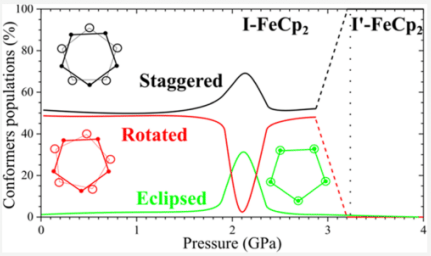

INTRODUCTION

Ferrocene ($FeCp_2$, where Cp denotes the cyclopentadienyl ring), since its discovery in 1951,[1] is the prototypic compound for a large family of sandwich complexes. Five different crystalline phases of $FeCp_2$ have been reported so far. At ambient pressure, monoclinic phase I, of space group $P2_1/n$ and disordered Cp rings, is present at room temperature until its melting point at 445 K. Below 178 K, the crystal transforms to modulated phase I″, and subsequently, below 164 K, it transforms to the ordered phase II, of triclinic space group $P\bar{1}$.[2,3] In phase II, two independent $FeCp_2$ molecules are present in the rotated conformation, with the torsion angle (τ) between the atoms of Cp rings equal to −8.7 and 9.0°.[3] In the structure of orthorhombic phase III determined at 98 K, the molecules assume the eclipsed conformation τ = 0°.[4] Later, it was established that phase III can be heated up to 275 K, well above the transition temperature between phases I and II.[5] Thus, phases I″ and II are metastable with respect to phase III.[2] Under high pressure, above 3.24 GPa, phase I isostructurally transforms to phase I′ with the molecules fully ordered.[6] All structural phase transitions of ferrocene crystals, revealed so far, involve molecular conformational changes as well as order−disorder transformations. In phase I, the disordered molecules are located on the inversion centers. This combination of the disorder and the crystal symmetry can be interpreted either as the result of intramolecular twisting of the Cp rings, leading to the conformation disordering (soft-molecule model, hereafter denoted as SM), or as the orientational disorder of rigid molecules (rigid-molecule model, denoted as RM), illustrated in Figure 1. Both of

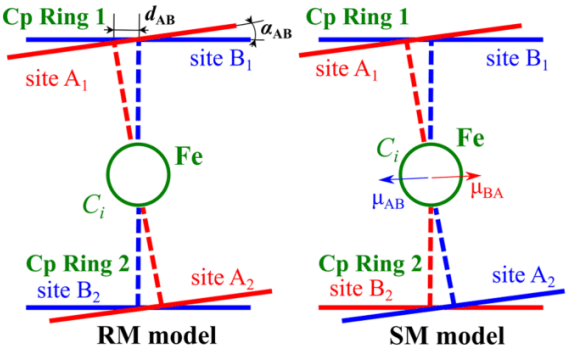

Figure 1. Schematic illustration of the rigid-molecule (RM) and soft-molecule (SM) models of ferrocene. Ring Cp_1 is disordered in sites A_1 and B_1, which are symmetry C_i-related to ring-Cp_2 sites A_2 and B_2, respectively. The RM model (left) allows the centrosymmetric staggered conformers A_1/A_2 (red) and B_1/B_2 (blue) only, while for the SM model (right), also, the noncentric polar conformers A_1/B_2 (red) and B_1/A_2 (blue) are possible. The instantaneous conformers in the RM and SM models are marked in red and blue, respectively. The inclination of rings and the displacement of their centroids are exaggerated for clarity (at 0.1 MPa, the inclination is about 2°).

Received: August 10, 2024
Revised: September 24, 2024
Accepted: September 26, 2024
Published: October 2, 2024

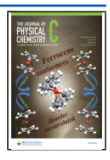

https://doi.org/10.1021/acs.jpcc.4c05399
J. Phys. Chem. C 2024, 128, 19392−19397

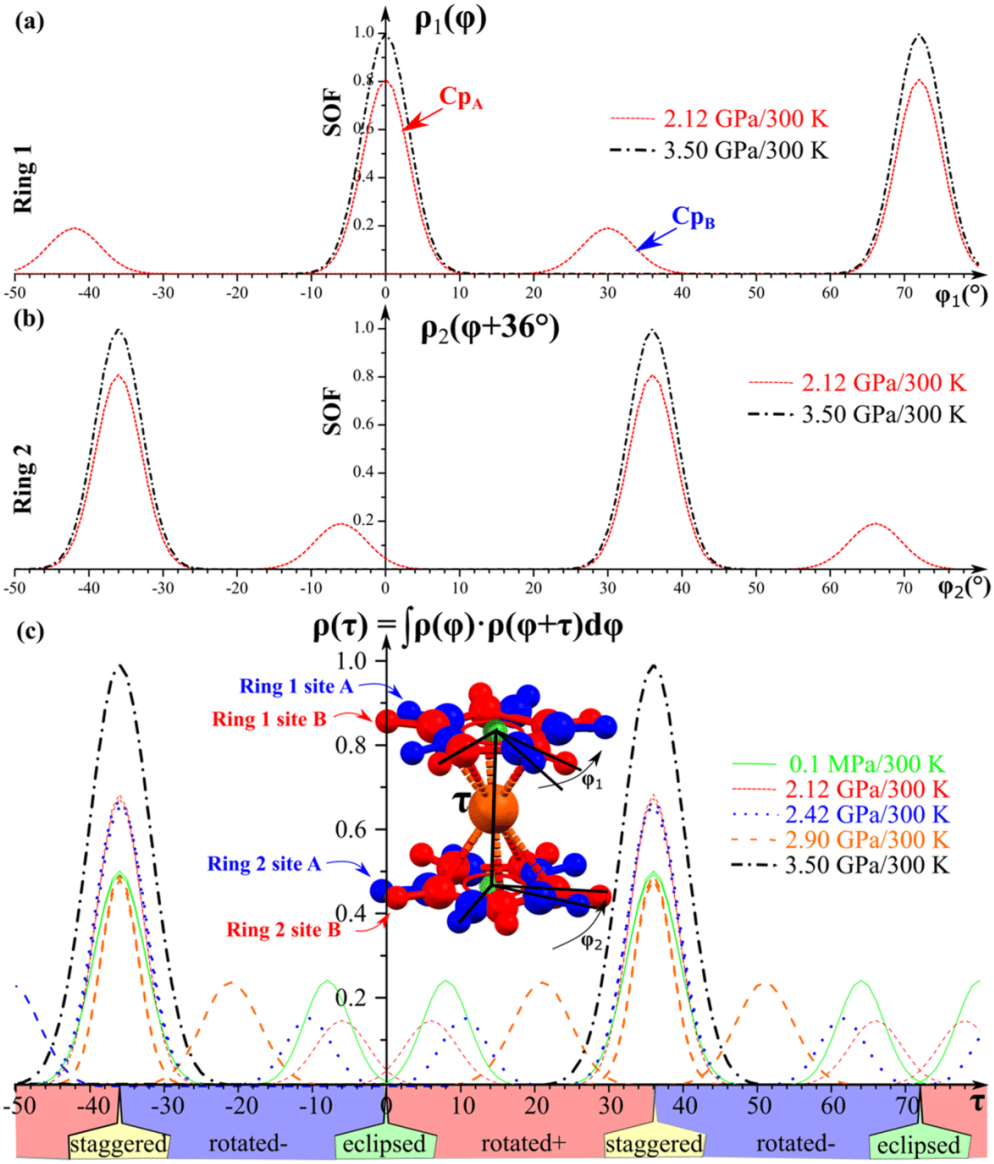

Figure 2. (a) Distribution of atomic density $\rho_1(\varphi)$ as a function of angle φ in ring 1 and (b) $\rho_2(\varphi + 36°)$ in ring 2 and (c) convolution $\rho(\tau)$ of these densities for selected experimentally investigated pressure values. Angle φ measures the displacements of disordered sites A and B in the Cp rings, while τ is the angular displacement of atomic densities between rings 1 and 2, and it corresponds to the torsion angle describing the conformation of the molecule. The achiral conformers staggered and eclipsed, as well as axially chiral rotated conformers, are indicated in (c).

these models can be associated with the static and dynamic disordering. The RM model implies the staggered conformation of all molecules located on the inversion centers. However, when the SM model is applied to the structure of phase I, also, other conformers are possible due to the sites of disordered Cp rings, which are not C_i-related. Appel et al.[7] established by the inelastic neutron scattering that the dynamic SM transformations prevail in phase I. Of all five known ferrocene phases, the ordered staggered conformation is exclusively present in the ordered phase I′, above 3.24 GPa. The staggered conformation is about 3.8 ± 1.3 kJ/mol less favored than the eclipsed conformation, as established by the electron diffraction.[8,9] While the molecular conformation is unequivocally determined in ordered phases I′, II, and III, there were doubts concerning the conformation of disordered molecules of phase I. In the initial structural studies of phase I in 1950,[10,11] the model implying the staggered conformers was applied. The later studies of phase I showed that the Cp rings are disordered, either in two or three sites.[12,13] For the disordered models, the location of $FeCp_2$ molecules on the C_i-symmetric position was interpreted as the implication of a molecular staggered conformation. In 2022, Kuzmin et al. repeated the measurements at low temperature and high pressure[14] and described the disorder of Cp rings, but they

https://doi.org/10.1021/acs.jpcc.4c05399
J. Phys. Chem. C 2024, 128, 19392−19397

considered the staggered conformers only. However, in the staggered D_{5d}-symmetric conformation, the ferrocene molecules are centrosymmetric and have no electric dipoles, which is inconsistent with clear dipole polarizability contributing to the electric permittivity of ferrocene phase I (Figure 1).[2,15] It was recently shown for nickelocene, isostructural to the disordered ferrocene phase I, that the disorder of Cp rings can lead to a combination of several conformers apart from the dominant staggered conformation. This distribution of conformations can be obtained by convoluting the position of disordered cyclopentadienyl ring 1, denoted as Cp_1, represented as the function of atomic density distribution $\rho_1(\varphi)$, with the analogue function $\rho_2(\varphi)$ representing the atomic density distribution in cyclopentadienyl ring 2, Cp_2. The convolution function $\int \rho_1(\varphi)\rho_2(\varphi-\tau)d\varphi$ showed that the overall conformation of nickelocene phase I consists of the staggered, rotated-right, rotated-left, and eclipsed contributions. Conformers rotated and eclipsed are not centrosymmetric and can display molecular dipoles. The distribution of these conformations clearly evolves within the pressure and temperature range of nickelocene phase I. These results prompted us to perform the analogous conformational analysis for the disordered structural models of ferrocene refined *de novo* on the recently measured high-pressure X-ray diffraction data.[6,16] These first high-pressure X-ray diffraction data measured for any metallocene were used for refining a simple structural model where the atomic displacement parameters (ADPs) accounted for the molecular disorder. In our present study, we refined the structural model with the Cp rings disordered in two positions, which reveals the distribution of molecular conformations (Figure 2) and their pressure dependence within phase I.

Ferrocene is so far the only known metallocene that crystallizes in five conformational phases, with the molecules disordered (phase I), staggered (phase I′), disordered and modulated (phase I″), rotated (phase II), and eclipsed (phase III). The accurate description of the molecular conformation−structure coupling is important not only for ferrocene itself but also for better understanding the transformations of all metallocenes[12,17,18] and other conformationally flexible compounds in general.

EXPERIMENTAL SECTION

High-pressure experiments have been performed at the ID09 synchrotron beamline of the European Synchrotron Research Facility (ESRF) in Grenoble, as described previously.[6,16] The highly parallel monochromatic X-ray beam (E = 30 keV, λ = 0.413 Å) was focused to 15 × 10 μm^2. The ferrocene single crystal was mounted in a membrane-driven high-pressure cell, with conical windows of 64° opening angle, and then filled with helium as the hydrostatic medium. The disordered structures of ferrocene were refined *de novo* by using the program Shelxl[19] implemented in software Olex2.[20] In the structural model, two partly occupied sites (labeled A and B) of the Cp ring were assumed, and each site of the Cp ring was freely refined with the only condition $SOF_A + SOF_B = 1$, where SOF_A and SOF_B are the site-occupation factors of sites A and B, respectively; the H atoms were located at idealized positions (C−H distance: 0.95 Å) and their isotropic displacement parameter μ_{iso} = 1.2 μ_{eq} of their carriers. This procedure of refining the disordered $FeCp_2$ structure is analogous to that applied in our previous analysis of nickelocene.[21] The structural models have been deposited in the Cambridge Structural Database with the CCDC numbers 2357927−2357943 and can be obtained free of charge on request from www.ccdc.cam.ac.uk.

RESULTS AND DISCUSSION

At ambient conditions, the crystal structure of ferrocene phase I is disordered, with the Cp ring assuming two sites A and B populated by 64 and 36%, respectively. The disordered sites A and B of Cp ring 1 are located in two planes inclined by a small angle α_{AB} of 2(1)° at 296 K/0.1 MPa; the centroids of sites A and B are displaced by a d_{AB} of about 0.1 Å (Figure 1). In this structure, half of the $FeCp_2$ molecule is symmetry-independent, so when assuming that the centroids and ring planes of these ring sites superimpose (i.e., α_{AB} = 0° and d_{AB} = 0 Å), the disorder can be described by two parameters: SOF_A (equal to $[1\text{-}SOF_B]$) and angle φ (measuring the rotation between the Cp-ring sites A and B in ring 1 about the average molecular pseudo-D_5 symmetry axis, equal to φ +36° in ring 2). Owing to the molecular symmetry in the crystal, the inversion center at the Fe cation, the disorder angle φ (Figure 2), and the SOF parameter of the disordered rings 1 and 2 are interdependent. The density distribution in Cp ring 1 is described by the function $\rho_1(\varphi)$ and that of ring 2 is described by the function $\rho_2(\varphi + 36°)$, as illustrated in Figure 2.

The dynamic rotations of rings 1 and 2 between their sites A and B in the SM model imply that several molecular conformers can coexist in the crystal. The average molecular conformation $\rho(\tau)$ is the convolution of the atomic density distributions in rings 1 and 2 (Figure 2). At 296 K, the three most populated conformations are staggered at 54% and rotated with angle τ equal to either +8 or −8°, each 23% populated. The rotated conformers are axially chiral, while the staggered conformer is achiral. The disorder angle φ in ferrocene is smaller compared to that in nickelocene, 13° at ambient conditions. The compression of ferrocene up to about 1.5 GPa weakly affects this disorder and conformation of the mixed components (A_1/B_2 and B_2/A_1), but on approaching 2.0 GPa, the φ angle starts to increase, and at about 2.2 GPa, it crosses the value of 36°, corresponding to the eclipsed conformation. At the same time, the SOF_B component assumes the lowest value of 0.19 (Figure 3), which minimizes the eclipsed conformation contribution to about 31% and increases the population of staggered conformers to about 69%. For nickelocene, the φ angle assumes 36° at 0.77 GPa and the population of eclipsed conformers is somewhat higher, at about 40%.[21]

The lowest SOF value corresponding to the reduced contribution of the eclipsed conformation (Figure 4) is consistent with the crystal environment favoring the staggered conformation in phases I and I′.

The anomaly of SOF(p) at 2.2 GPa correlates with the strongly anomalous changes of unit-cell parameter b and monoclinic β angle. Above 2.2 GPa, the compressibility of parameter b becomes negative, while the decrease of angle β starts to become steeper (Figure 5). The unit-cell parameters a and c are less sensitive to the SOF changes (*cf.* Figures S1 and S2 in the Supporting Information).

As mentioned at the beginning of the discussion, the centroids of the independently refined sites of the disordered Cp ring do not superimpose. Therefore, it was pointed out that the detailed description of the disorder in ferrocene phase I requires additional parameters, such as the inclination angle between the Cp-ring sites (α_{AB}, *cf.* Figure S3 in the Supporting

https://doi.org/10.1021/acs.jpcc.4c05399
J. Phys. Chem. C 2024, 128, 19392−19397

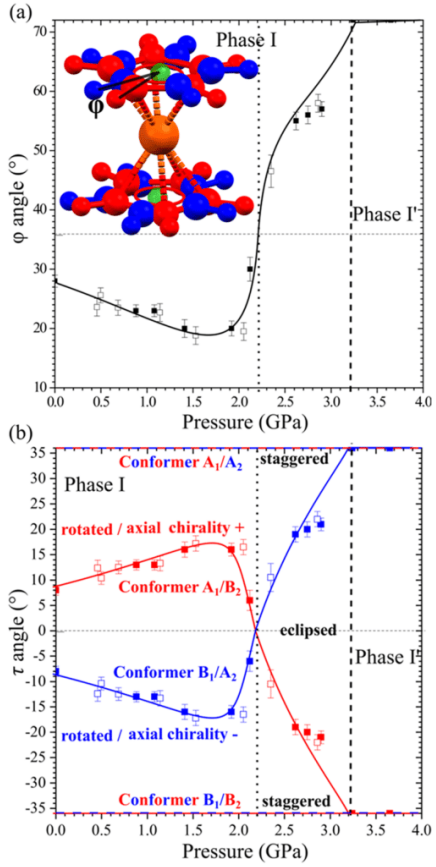

Figure 3. (a) Pressure dependence of angle φ measuring the angular displacement between sites A and B around the average centroid of the disordered Cp ring in ferrocene (*cf.* Figure 2). At 2.2 GPa (the vertical dotted line), angle φ becomes equal to 36° (horizontal dotted line), corresponding to the eclipsed conformation between sites A_1/B_2 and B_1/A_2, when the difference between parameters SOF_A and SOF_B is the largest (Figure 4) and the crystal is composed of 69% staggered and 31% eclipsed conformers. The vertical dashed line marks the phase transition to ordered phase I′. (b) Evolution of the molecular conformation measured by angle τ.

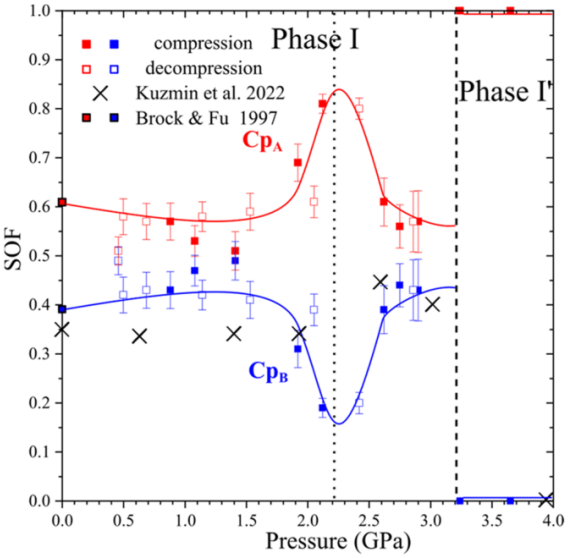

Figure 4. Site-occupation factors (SOFs) of the disordered Cp ring in ferrocene phase I are plotted as a function of pressure. The SOF_A (red) and SOF_B (blue) at 293 K/0.1 MPa after Brock and Fu.[13] The compression and decompression runs are denoted with full and empty symbols, respectively. The vertical dotted line indicates the φ angle of 36° assumed in ferrocene at 2.2 GPa, corresponding to the eclipsed conformation between the Cp-ring sites A_1/B_2 and B_1/A_2, when the crystal is composed in 69% of the staggered and 31% of the eclipsed conformers. The vertical dashed line indicates the phase transition to ordered phase I′. The SOF(p) values reported by Kuzmin et al. are indicated by black crosses.[14]

Information) and the distance d_{AB} between the centroids of sites A and B (Figure 1). In the SM model of the disorder, the inclination angle α_{AB} and displacement d_{AB} generate a considerable dipole moment for the rotated and eclipsed conformers (Figure 6), consistent with the dielectric response of ferrocene crystals.[2,15]

The ferrocene crystals exhibit a remarkable interdependence of the compressibility, thermal expansion, and molecular conformation. The onset of negative linear compressibility (NLC) of parameter b starts above 2.2 GPa when the displacement angle φ approaches values of ±36°, making the highest population of eclipsed conformers. This conformation—NLC correlation is observed also as a function of temperature below 230 K (Figure S4 in the Supporting Information). On cooling the crystal to 270 K, parameter a contracts stronger than parameter c, while at still lower temperature, this trend is reversed. An analogous reversed trend occurs for the compression of parameters a and c around 0.5 GPa. The rule of reverse effects of temperature and pressure[22] is fulfilled within the range of phase I. The transitions to phase I″ below 172.8 K and to phase I′ above 3.2 GPa are clearly different in their characters and associated lattice strains. The analogous relations between the lattice strain and the molecular conformation as a function of pressure and temperature were observed in nickelocene too (*cf.* Figure S5 in the Supporting Information).

■ CONCLUSIONS

Despite the relatively simple molecular structure of ferrocene, its disordered phase I exhibits complex relations among the molecular dynamics, conformation, and lattice strain. The structural models of phase I reveal the rich conformational landscape evolving under pressure and temperature, depending on the disorder parameters SOF, φ, d_{AB}, α_{AB}, and the atomic positions. The dynamic nature of the disorder, recently confirmed by quasielastic scattering,[7] implies the presence of several populations of conformers, including the rotated and eclipsed ones, apart from the dominant centrosymmetric staggered conformer. The disorder parameters are connected to the molecular conformers and their crystal environment. This correlation explains the anomalous b-parameter compression when all conformers become staggered in fully ordered phase I′. The distribution of conformer changes in the SOF and φ parameters observed in ferrocene phases I and I′ are similar to those in nickelocene. The observed convolution of disordered rings resulting in the pressure-dependent populations of staggered, rotated, and eclipsed conformers in ferrocene phase I is consistent with recent dielectric[2,15] and

https://doi.org/10.1021/acs.jpcc.4c05399
J. Phys. Chem. C 2024, 128, 19392−19397

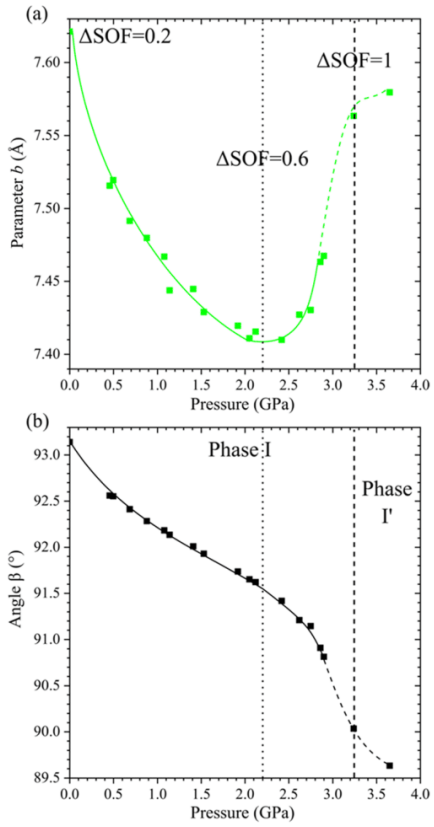

Figure 5. (a) Unit-cell parameter b and (b) monoclinic β angle of ferrocene phases I and I′ as a function of pressure. Standard deviations are smaller than the plotted symbols. The dotted vertical lines indicate the pressure of 2.2 GPa, when the difference between parameters SOF_A and SOF_B is the largest (Figure 4); the dashed vertical lines mark the boundary of fully ordered phase I′.

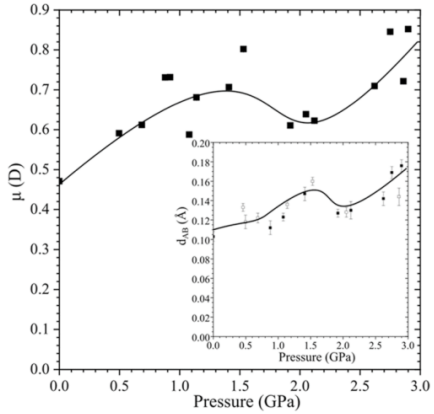

Figure 6. Molecular dipole moment calculated for the rotated and eclipsed conformers, based on the molecular dimensions, SOF_A, SOF_B, and the distance between centroids Cp_{cA} and Cp_{cB} (d_{AB}) shown in the inset.

Raman studies,[23] as well as with the previously obtained populations of conformers in nickelocene.[21] The obtained information contradicts the ideally nonpolar structure of ferrocene molecules, as it is presented in textbooks.[24−26] Our study reveals a class of crystals, where within one phase, the conformational conversions impact macroscopic properties, such as the dielectric response, anomalous expansion, and compressibility.

■ ASSOCIATED CONTENT

Supporting Information

The Supporting Information is available free of charge at https://pubs.acs.org/doi/10.1021/acs.jpcc.4c05399.

Changes of unit-cell parameters a and c as a function of pressure, angle α_{AB} changes as a function of pressure, relative unit-cell parameters of ferrocene phases I, I′, I″, and II as a function of temperature and pressure, relative unit-cell parameters of nickelocene as a function of temperature and pressure, distance between Cp_c and Fe^{2+} as a function of pressure, and shortest CH···Fe contact as a function of pressure (PDF)

■ AUTHOR INFORMATION

Corresponding Author

Andrzej Katrusiak − *Department of Materials Chemistry, Faculty of Chemistry, Adam Mickiewicz University, 61-614 Poznań, Poland;* orcid.org/0000-0002-1439-7278; Phone: +48 61 829 1590; Email: katran@amu.edu.pl

Authors

Ida Moszczyńska − *Department of Materials Chemistry, Faculty of Chemistry, Adam Mickiewicz University, 61-614 Poznań, Poland;* orcid.org/0000-0002-0791-2278

Damian Paliwoda − *European Spallation Source ERIC, 224 84 Lund, Sweden;* orcid.org/0000-0003-0020-0515

Complete contact information is available at: https://pubs.acs.org/10.1021/acs.jpcc.4c05399

Author Contributions

The manuscript was written through contributions of all authors. All authors have given approval to the final version of the manuscript.

Notes

The authors declare no competing financial interest.

■ ACKNOWLEDGMENTS

This study was supported by the Polish Ministry of Higher Education through the statutory fund of Adam Mickiewicz University in Poznań.

■ REFERENCES

(1) Kealy, T. J.; Pauson, P. L. A New Type of Organo-Iron Compound. *Nature* **1951**, *168*, 1039−1040.

(2) Katrusiak, A.; Rusek, M.; Dušek, M.; Petříček, V.; Szafrański, M. Dipole-Moment Modulation in New Incommensurate Ferrocene. *J. Phys. Chem. Lett.* **2023**, *14*, 3111−3119.

(3) Seiler, P.; Dunitz, J. D. The Structure of Triclinic Ferrocene at 101, 123 and 148 K. *Acta Crystallogr., Sect. B: Struct. Crystallogr. Cryst. Chem.* **1979**, *35*, 2020−2032.

(4) Seiler, P.; Dunitz, J. D. Low-Temperature Crystallization of Orthorhombic Ferrocene: Structure Analysis at 98 K. *Acta Crystallogr., Sect. B: Struct. Crystallogr. Cryst. Chem.* **1982**, *38*, 1741−1745.

(5) Calvarin, G.; Berar, J. F. Etude Par Diffraction Des Rayons X Sur Poudre de La Transition Ordre−Désordre Du Ferrocène $Fe(C_5H_5)_2$. *J. Appl. Crystallogr.* **1975**, *8*, 380−385.

(6) Paliwoda, D.; Kowalska, K.; Hanfland, M.; Katrusiak, A. U-Turn Compression to a New Isostructural Ferrocene Phase. *J. Phys. Chem. Lett.* **2013**, *4*, 4032−4037.
(7) Appel, M.; Frick, B.; Spehr, T. L.; Stühn, B. Molecular Ring Rotation in Solid Ferrocene Revisited. *J. Chem. Phys.* **2015**, *142*, No. 114503.
(8) Haaland, A.; Nilsson, J. E.; Olson, T.; Norin, T. The Determination of Barriers to Internal Rotation by Means of Electron Diffraction. Ferrocene and Ruthenocene. *Acta Chem. Scand.* **1968**, *22*, 2653−2670.
(9) Bohn, R. K.; Haaland, A. On the Molecular Structure of Ferrocene, $Fe(C_5H_5)_2$. *J. Organomet. Chem.* **1966**, *5*, 470−476.
(10) Dunitz, J. D.; Orgel, L. E.; Rich, A. The Crystal Structure of Ferrocene. *Acta Crystallogr.* **1956**, *9*, 373−375.
(11) Eiland, P. F.; Pepinsky, R. X-Ray Examination of Iron Biscyclopentadienyl. *J. Am. Chem. Soc.* **1952**, *74*, 4971.
(12) Takusagawa, F.; Koetzle, T. F. A Neutron Diffraction Study of the Crystal Structure of Ferrocene. *Acta Crystallogr., Sect. B: Struct. Crystallogr. Cryst. Chem.* **1979**, *35*, 1074−1081.
(13) Brock, C. P.; Fu, Y. Rigid-Body Disorder Models for the High-Temperature Phase of Ferrocene. *Acta Crystallogr., Sect. B: Struct. Sci.* **1997**, *53*, 928−938.
(14) Kuzmin, A. V.; Meletov, K. P.; Faraonov, M. A. Pressure and Temperature Transformations of the Molecular Conformation and Crystal Structure of Ferrocene $Fe^{2+}(\eta^5\text{-}C_5H_5)^{2-}$. *J. Phys. Chem. C* **2022**, *126*, 3688−3695.
(15) Bermúdez-García, J. M.; Yáñez-Vilar, S.; Castro-García, S.; Señarís-Rodríguez, M. A.; Sánchez-Andújar, M. New Properties in Old Systems: Cooperative Electric Order in Ferrocene and Ammonia-Borane. *RSC Adv.* **2015**, *5*, 83818−83824.
(16) Paliwoda, D.; Hanfland, M.; Katrusiak, A. Pressure-Enhanced Environment Effects in Ferrocene Phases. *J. Phys. Chem. C* **2019**, *123*, 25719−25723.
(17) Braga, D.; Grepioni, F. Crystal Construction and Molecular Interplay in Solid Ferrocene, Nickelocene, and Ruthenocene. *Organometallics* **1992**, *11*, 711−718.
(18) Levendis, D. C.; Boeyens, J. C. A. Analysis of the Molecular Conformation and Rotational Disorder in Crystalline Ferrocene and Nickelocene. *J. Crystallogr. Spectrosc. Res.* **1985**, *15*, 1−17.
(19) Sheldrick, G. M. Crystal Structure Refinement with SHELXL. *Acta Crystallogr., Sect. C: Struct. Chem.* **2015**, *71*, 3−8.
(20) Dolomanov, O. V.; Bourhis, L. J.; Gildea, R. J.; Howard, J. A. K.; Puschmann, H. OLEX2: A Complete Structure Solution, Refinement and Analysis Program. *J. Appl. Crystallogr.* **2009**, *42*, 339−341.
(21) Moszczyńska, I.; Katrusiak, A. Lattice-Strain Coupled to Molecular Conformation and Disorder in Compressed Nickelocene. *J. Phys. Chem. C* **2021**, *125*, 15670−15675.
(22) Hazen, R. M.; Finger, L. W. *Comparative Crystal Chemistry. 468 Temperature, Pressure, Composition and Variation of the Crystal 469 Structure*; John Wiley: New York, 1982.
(23) Meletov, K. Raman Study of the Conformational Instability of a Ferrocene Molecule at High Pressure: Influence of a Crystal Field *J. Raman Spectrosc.* 2024 DOI: 10.1002/jrs.6713.
(24) Cotton, F. A.; Wilkinson, G.; Murillo, C. A.; Bochmann, M. *Advanced Inorganic Chemistry*; John Wiley & Sons: New York, 1999.
(25) Eliel, E. L.; Wilen, S. H.; Mander, L. N. *Stereochemistry of Organic Compounds*; John Wiley & Sons: New York, 1994.
(26) Lee, J. D. *Concise Inorganic Chemistry*; Blacwell Science: Oxford, 1996.

https://doi.org/10.1021/acs.jpcc.4c05399
J. Phys. Chem. C 2024, 128, 19392−19397

Artykuł 3

Ida Moszczyńska, Andrzej Katrusiak

Competition between Hydrogen and Anagostic Bonds in Ruthenocene Phases under High Pressure
***J. Phys. Chem C,* 2022, *126 (10)*, 5028-5035**

THE JOURNAL OF PHYSICAL CHEMISTRY C
A JOURNAL OF THE AMERICAN CHEMICAL SOCIETY

pubs.acs.org/JPCC

Article

Competition between Hydrogen and Anagostic Bonds in Ruthenocene Phases under High Pressure

Ida Moszczyńska and Andrzej Katrusiak*

Cite This: *J. Phys. Chem. C* 2022, 126, 5028–5035

Read Online

ACCESS | Metrics & More | Article Recommendations | Supporting Information

ABSTRACT: High pressure favors anagostic bonds CH···Ru, which leads to a new polymorph of ruthenocene $RuCp_2$, where Cp denotes the cyclopentadienyl ring $[C_5H_5]^-$. Ruthenocene can be isothermally compressed in its ambient-pressure phase α up to 3.9 GPa, when it transforms to the new phase, β. The transition between phases α and β proceeds with an exceptionally wide hysteresis extending between 0.7 and 3.9 GPa. The transition destroys single crystals of $RuCp_2$, but a single crystal of polymorph β can be obtained by high-pressure nucleation (above 3.9 GPa) and its isochoric growth continued above 1.0 GPa. On decompression, phase β transforms back to phase α at 0.7 GPa. The structures of phases α (space group *Pnma*) and β (space group *Pcmb*) have been determined by X-ray diffraction in the pressure range from 0.1 MPa up to 3.9 GPa. The eclipsed conformation of α-$RuCp_2$ is retained in phase β, which contrasts with the conformational phase transitions in ferrocene and nickelocene. The lattice dimensions and molecular orientations in ruthenocene polymorphs are clearly related, which leads to the characteristic twinning-like oriented growth of the crystals of concomitant phases.

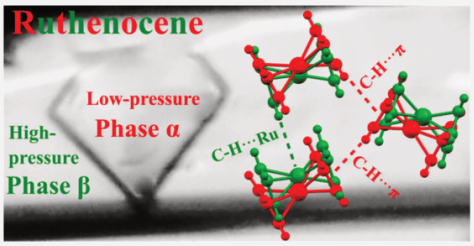

INTRODUCTION

Metallocenes are known to undergo solid-state transformations involving the conformational changes in molecules. In analogy to conformational polymorphs,[1,2] we term such transformations conformational phase transitions. Well known are the phase transitions of metallocenes MCp_2, where divalent metal cation M^{2+} is sandwiched between two cyclopentadiene rings (Cp). Crystals of prototypic metallocenes $FeCp_2$ and $NiCp_2$ are isostructural under ambient conditions (0.1 MPa, 293 K): their symmetry is of monoclinic space group $P2_1/n$ (Z = 2), and staggered conformation prevails in the disordered molecules located in the inversion center. This type of structure was reported for ferrocene phase I,[3,4] nickelocene phase I,[5] vanadocene,[6] chromocene,[7] cobaltocene,[8] and magnesocene.[9] Another type of metallocene crystals, of orthorhombic space group *Pnma* (Z = 4), and ordered molecules in the eclipsed conformation is characteristic for metallocenes with the cations from eighth group of the periodic table: ruthenocene,[10] osmocene,[11] and ferrocene phase III, obtained at low temperature and transformed back to phase I upon heating at about 270 K.[12] Doman et al.[13] established that the energy of M−Cp stretching in $OsCp_2$ (1090 kJ/mol Å^2), $RuCp_2$, and $FeCp_2$ (859 kJ/mol Å^2) is higher than those of other metallocenes containing the metal cation from the first row of transition metals, which do not fulfill the 18-electron rule. The Ru^{2+}, Os^{2+}, and Fe^{2+} configuration in MCp_2 is $(e_{2g})^4$ $(a_{1g})^2$ $(e_{1g})^0$ and the bond between the M^{2+} cation and the Cp ring involves electron donation from the cation to molecular orbitals of neighboring Cp rings from e_{2g} orbitals (d_{xy} and $d_{x^2-y^2}$) and the backdonation from Cp rings to e_{1g} orbitals (d_{xy}, d_{yz}).[14,15] It appears that the molecular conformation and its disorder under normal conditions correlate with the atomic number (as well as the atomic weight) of the M atom and the M−Cp distance, as shown in Figure 1. Our inspection of the recommended storage conditions of metalocenes MCp_2 has shown that the orthorhombic metallocenes with the M^{2+} cation in the d^6 configuration are more stable and less sensitive to air and humidity than those with M^{2+} in other configurations. There are also metallocenes with nonparallel Cp rings (Cp_c···M···Cp_c angle around 150°, where Cp_c denotes the Cp centroid), characteristic for metal cations from 14th group of the periodic table: $SnCp_2$ (space group *Pbcm*)[16] and $GeCp_2$ ($P22_12_1$).[17] These molecules are bent due to the lone electron pair of the M^{2+} cation.[18] Under high pressure, $FeCp_2$ and $NiCp_2$ transform into phase I′, built of ordered staggered conformers favored by their centrosymmetric environment in the crystal. Differential scanning calorimetry revealed no anomalies in ruthenocene between 100 and 330 K,[19] and X-ray diffraction structural determination[20] has shown that phase α can be cooled down to 15 K.

Received: December 2, 2021
Revised: February 22, 2022
Published: March 7, 2022

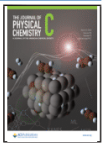

https://doi.org/10.1021/acs.jpcc.1c10249
J. Phys. Chem. C 2022, 126, 5028–5035

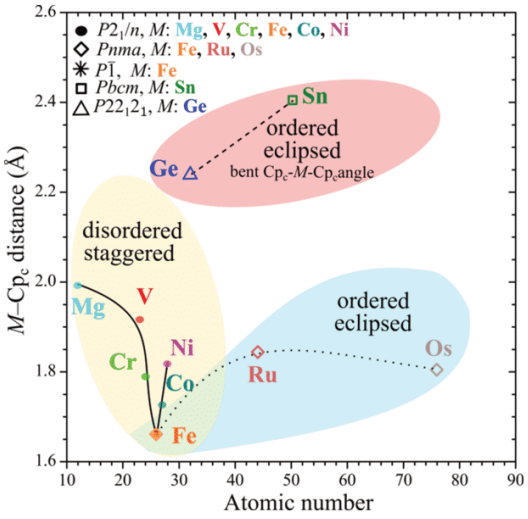

Figure 1. Distance M−Cp_c as a function of atomic number for $M^{2+}Cp_2$ metallocenes (Cp_c denotes the Cp-ring centroid) under ambient pressure. The legend lists the space groups and metal centers of metallocene crystal types distinguished by different symbols in this plot. Highlights indicate the conformer type.

Presently, we have investigated the high-pressure structure of $RuCp_2$, in order to check if its conformation can be destabilized under nonambient conditions. The temperature- and pressure-dependent $FeCp_2$ phases I, II, III, and I′ have been applied as the reference structural types for $RuCp_2$ and other metallocenes throughout this article. For example, $RuCp_2$ at ambient pressure belongs to the structural type III (i.e., it is isostructural with $FeCp_2$ phase III). All phase transitions revealed so far for MCp_2 metalocenes involved the conformational transformations of molecules. However, presently, we have found a new $RuCp_2$ phase, which does not match to that pattern. For labeling the phases of $RuCp_2$, Greek letters α (the ambient-pressure type III structure) and β (the new high-pressure phase) have been applied.

EXPERIMENTAL SECTION

All experiments on $RuCp_2$ were performed in a Merrill-Bassett diamond anvil cell (DAC)[21] modified by mounting the anvils directly on the edges of steel conical windows. In the first series of experiments, X-ray diffraction data were measured on single crystals obtained under normal conditions and compressed in the methanol/ethanol/water (MEW, 16:3:1) mixture. The second series of experiments was performed for ruthenocene single-crystal samples, nucleated at 3.9 GPa, and grown by isochoric in situ recrystallization at 1 GPa. In these experiments, tetrahydrofuran (THF) was used both as the solvent and as the hydrostatic medium. The pressure in the DAC chamber was calibrated by the ruby-fluorescence shift,[22] measured with a photon control spectrometer with enhanced resolution affording the 0.02 GPa accuracy. In the first series of experiments, the single crystals of $RuCp_2$ were gradually isothermally compressed to 3.9 GPa, above which the single crystals broke. The MEW mixture was also used in powder X-ray diffraction (PXRD) measurements on the gently grounded sample. It was compressed in the DAC up to 5.29 GPa. These PXRD patterns showed that above 3.9 GPa, the $RuCp_2$ sample transforms to a new phase β.

The in situ crystallizations in the pressure range up to 1.3 GPa from THF solution without prior high-pressure nucleation yielded exclusively the crystals of the ambient-pressure phase α (Figure 2). Single crystals of phase β were

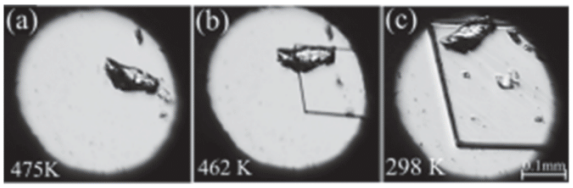

Figure 2. High-pressure in situ isochoric crystallization of $RuCp_2$ in phase α (a) nucleation at 475 K; (b) single crystal at 462 K; and (c) single crystal at 296 K/1.00 GPa. One big and several small irregular ruby chips for pressure calibration (cf. Figure S1a in the Supporting Information) are grouped in the right part of the chamber.

grown in the following steps: (i) the polycrystalline sample was compressed in THF to about 3.9 GPa, above the hydrostatic limit of this pressure transmitting medium (2.24 GPa[23]); (ii) the pressure was reduced to 1.0 GPa; (iii) all but one crystal grains were dissolved; and (iv) a single crystal was grown under isochoric conditions (Figure 3). The hysteresis pressure values for between 0.7 and 3.9 GPa were determined by PXRD, single-crystal X-ray diffraction (SCXRD) measurements, and recrystallizations.

One of the isochoric in situ recrystallizations at 1.0 GPa resulted in two single crystals, the larger one of phase β (space group *Pcmb*) and the smaller one of phase α (space group *Pnma*). Crystal axes of both phases are exactly parallel (Figure 3d), which indicates a strong preference of these structures for

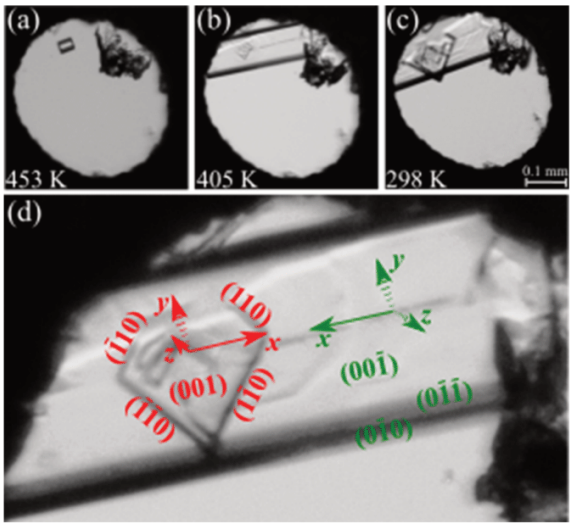

Figure 3. Isochoric concomitant crystallization of $RuCp_2$ phases: (a) phase β nucleated at 453 K; (b) single crystal of phase β with a nucleus of phase α on its top face at 405 K; and (c) two single crystals grown together at 298 K/1.00 GPa. (d) In situ-grown double-nucleus oriented polymorphs α (rhomboid, red labels) and polymorph β (elongated plate, green labels). Polymorphs α and β have grown along parallel crystal directions (cf. Figure S1b in the Supporting Information). Several ruby chips for pressure calibration are grouped by the top-right edge of the gasket.

https://doi.org/10.1021/acs.jpcc.1c10249
J. Phys. Chem. C 2022, 126, 5028−5035

Table 1. Selected Crystallographic Data of $RuCp_2$ Phases α and β (cf. Table S1 in the Supporting Information)

pressure (GPa)		0.0001	2.05	1.30	2.10
Phase		α	α	β	β
space group[a]		*Pnma*	*Pnma*	*Pcmb*	*Pcmb*
unit cell (Å)	*a*	7.13(2)	6.7022(4)	5.5336(3)	5.4427(3)
	b	8.99(2)	8.5063(5)	9.6862(12)	9.5246(13)
	b	12.81(2)	12.4057(8)	13.564(4)	13.433(4)
Z/Z'		4/0.5	4/0.5	4/0.5	4/0.5
density (g/cm^3)		1.871	2.172	2.113	2.208

[a]Nonstandard setting of space group no. 57, *Pbcm*, has been applied to phase β.

this particular mutual orientation. This feature resembles the pseudo-symmetry relating the orientation of crystal twins. The difference is that in typical twins, both grains are of the same phase (and identical structure), while in the α-$RuCp_2$/β-$RuCp_2$, the phases of the grains are different. Therefore, in this study, we refer to the traditional twins as identical twins, as distinguished from the double-nucleus (or nonidentical) twin α-$RuCp_2$/β-$RuCp_2$. The phenomenon of oriented intergrowth of two different crystal phases of the same compound was reported in the literature, for example, for polytypes of silicoferrites of calcium and aluminum[24] and carbon silicate.[25]

SCXRD data were measured on a KUMA KM-4 CCD 4-cycle diffractometer, while PXRD experiments on an Excalibur EOS diffractometer, both employing the MoKα radiation. XRD experiments and preliminary data reduction were performed with the CrysAlis software from Oxford Diffraction. Corrections for the DAC absorption, sample shadowing by the gasket, and sample absorption were added to eliminate the diamond reflections and to correct the intensities of sample reflections.[26,27] The crystal structures of phase α under ambient conditions and phase β at 1.0 GPa were solved by direct methods of Shelxs and refined by full-matrix least squares on F^2's with Shelxl,[28] operated through Olex 2.[29] Then, these structures were used as the starting models for the higher-pressure experiments. The H atoms were ideally located by AFIX 43 at 0.93 Å from the C-atoms. The crystallographic data of $RuCp_2$ phases are summarized in Table 1 and detailed in Table S1 in the Supporting Information. The crystallographic and structural information has been deposited in the Cambridge Crystallographic Database Centre as supporting publications with numbers CCDC 2111120−2111130. Their copies can be obtained free of charge from www.ccdc.cam.ac.uk.

RESULTS AND DISCUSSION

The crystal structures of metallocenes MCp_2 are connected with their molecular conformation, symmetry, dynamics, cation size, and electron configuration (Figure 1). The structure−conformation interdependence is apparent for the $FeCp_2$ polymorphs. Under normal conditions in its phase I, the molecules are conformationally disordered: above 3.24 GPa in phase I′, the molecules are present in D_{5i}-symmetric staggered conformation; below 164 K in phase II, both *R*- and *S*-rotamers are present and their molecular symmetry is reduced to D_5; and below 100 K in phase III, the eclipsed conformer is D_{5h} symmetric.[30] This preference for the eclipsed conformation prevails over the effect of crystal field in low temperature, when ferrocene phase III is formed at atmospheric pressure. The staggered conformation is energetically unfavored, but in phase I′, it is induced by the centrosymmetric crystal environment of molecules. Phase α of ruthenocene is isostructural with ferrocene phase III; however, the high-pressure phase β of $RuCp_2$, revealed in this study, retains the eclipsed conformers. To our knowledge, phases α and β of $RuCp_2$ are the first metallocene polymorphs with the identical molecular conformation (eclipsed), the same symmetry (D_{5h}) of conformers, and even the same special positions of molecules in the crystal (atom Ru is located on the mirror plane perpendicular to [*y*] and the Cp rings are perpendicular to this plane, Figure 4).

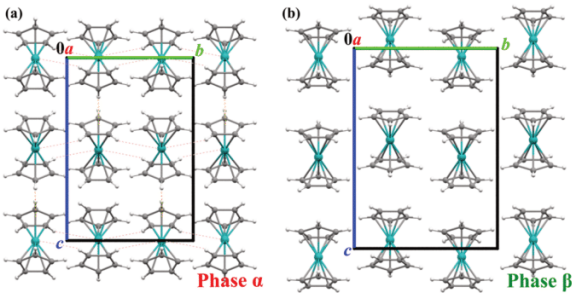

Figure 4. Structures of ruthenocene: (a) phase α at 0.13 GPa and (b) phase β at 1.00 GPa. Both these projections are drawn along the direction [100] in the same scale (cf. Table 1). The intermolecular C−H···Ru and C−H···π are indicated in phase α in pale pink and yellow, respectively. Contacts C−H···Ru in phase β run along the viewing direction and therefore they cannot be marked in this projection.

Compression of $RuCp_2$ Phases α and β. The in situ recrystallizations of ruthenocene performed in the DAC yield the atmospheric-pressure phase α up to 1.3 GPa. α-$RuCp_2$ can be compressed to 3.9 GPa, when it transforms to β-$RuCp_2$. The stability region of phase β has been determined by PXRD for the sample compressed in the MEW mixture in the DAC (cf. Figure S2 in the Supporting Information). In the compression mode, the PXRD pattern changes above 3.9 GPa, and the new reflections are consistent with phase β. The decompression of phase β results in its transition to phase α at 0.7 GPa, as confirmed by the PXRD patterns of the sample. These PXRD measurements revealed that the transition proceeds with a considerable hysteresis of about 3.2 GPa. This wide pressure hysteresis suggests that there are some specific intermolecular interactions in phases α and β stabilizing their structures. The wide hysteresis can be explained by the double-well potential energy (E_p), where the E_p difference between the barrier maximum and the β-phase minimum is of about 14.6 kJ/mol, as assessed from the estimated volume reduction at 3.9 GPa, when the transition to phase β takes place (cf. Figures 5 and S3 in the Supporting Information).

https://doi.org/10.1021/acs.jpcc.1c10249
J. Phys. Chem. C 2022, 126, 5028−5035

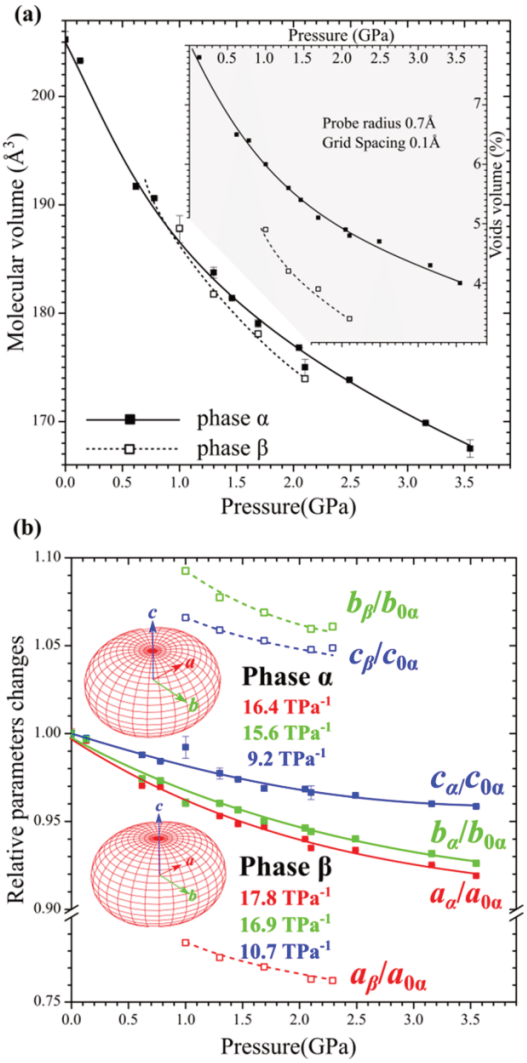

Figure 5. Compression of ruthenocene phase α (full symbols and solid lines) and phase β (open symbols and dashed lines): (a) molecular volume, the inset shows the relative volume of voids and (b) unit-cell parameters related to the ambient-pressure values of phase α at 0.1 MPa/296 K, the insets show the graphical representation of compressibility tensors and their eigenvalues along directions [x] (red), [y] (green), and [z] (blue).

The similar crystal structures of phases α and β (Figure 4) result in their similar linear compressibilities $\beta_x = -1/x \cdot dx/dp$ (Figure 5). The lowest compressibility is along the [z] direction, which correlates with the elongated shape of the $RuCp_2$ molecules and their orientation, inclined by about 30° to the [z] axis. A similar relation between the molecular elongation, orientation, and compressibility was noted for molecular crystals of xylitol.[31] The compressibilities are clearly nonlinear, which correlates with the strong reduction of intermolecular voids. The molecular-volume plots for phases α and β intersect at about 1.1 GPa, above which the gap between higher volume of phase α and lower volume of phase β increases. In our experiment, the single crystal of phase β was grown at 1.0 GPa and then it was isothermally compressed to 2.3 GPa, just above the freezing pressure of THF at 2.24 GPa. Thus, the last SCXRD measurement was performed under pseudo-hydrostatic conditions. The nonhydrostatic conditions in frozen THF hampered the SCXRD measurements under still higher pressure.

According to the shortest-contact analysis,[32] the $RuCp_2$ α-polymorph is mainly stabilized by CH···π interactions (Figure 6). At 0.1 MPa, the shortest intermolecular distance between the H atom and the Cp ring centroid (Cp_c) equals about 2.86 Å and contacts C−H···Cp_c are shorter by circa 0.04 Å than the sum of van der Waals radii, equal to 2.9 Å, according to Bondi.[33] The C−H···Cp_c angle equals about 160°. In polymorph β, the shortest intermolecular C−H···Cp_c increases to 3.06 Å and the C−H···Cp_c angle equals about 136°, which shows that this type of interaction becomes less significant than in phase α. The elongation of C−H···π bonds in phase β contrasts with the shortening of contacts C−H···Ru and H···H. In phase α, the shortest intermolecular contacts C−H···Ru are longer than the sum of van der Waals radii (3.42 Å at 0.1 MPa), up to 0.7 GPa.[33,34] Angle C−H···Ru in phase α hardly changes between 0.1 MPa (144.4°) and 3.6 GPa (cf. Figure S4 in the Supporting Information). In this molecular orientation, the lone pair on the d orbital cannot effectively coordinate the hydrogen atom, which would require a linear arrangement.[35] This suggests that the intermolecular C−H···Ru contacts in phase α hardly contribute to the cohesion forces. In phase β, the C−H···Ru contacts become shorter than those in phase α (Figure 6) and angle C−H···Ru approaches 180°: 177.5° at 1.00 GPa and 174° at 2.1 GPa (cf. Figure S4 in the Supporting Information). This arrangement allows the ruthenium cation to accept the proton.[35] Such anagostic C−H···Ru bonds[36−39] are documented in the structures under ambient conditions in the literature, but they involve H-donor groups more polar compared to the Cp ring.[40]

Short H···H contacts are associated with weak van der Waals interactions connected with the steric hindrances and the close packing of molecules in the compressed structure. These distances are similar to those in the structures of $FeCp_2$ and $NiCp_2$,[41] where the H···H contacts and the crystal environment interfere with the molecular conformation (Figure 6). Interestingly, the H···H contacts and C−H···π bonds are compressed at a very similar rate within phase α, but the H···H contacts are abruptly shortened and C−H···π bonds are elongated on the transition to phase β. This difference can result from the directional character of hydrogen bonds C−H···π and the central character of contacts H···H.

Borissova et al.[42] considered short C−H···Ru contacts as important cohesion forces in the crystal structure of α-$RuCp_2$. However, these shortest H···Ru distances under ambient conditions are about 0.18 Å longer than the sum of van der Waals radii (3.25 Å).[33,34] Thus, this interaction is most likely weaker than the hydrogen C−H···π bond (described above in detail). In β-$RuCp_2$, a new type of C−H···Ru interaction appears: it is shorter and it is easily compressed compared to that in phase α (Figure 6). These new features suggest that interactions C−H···Ru in β-$RuCp_2$ are stronger compared to those in phase α. According to the H-donor and H-acceptor properties and to geometrical parameters, this new C−H···Ru interaction in β $RuCp_2$ can be classified as an anagostic interaction.[36,38] Contacts C−H···Ru link the $RuCp_2$ molecules into chains expanding along the direction [010] in phase α (there are two molecules per b translation) and along [100] in

https://doi.org/10.1021/acs.jpcc.1c10249
J. Phys. Chem. C 2022, 126, 5028−5035

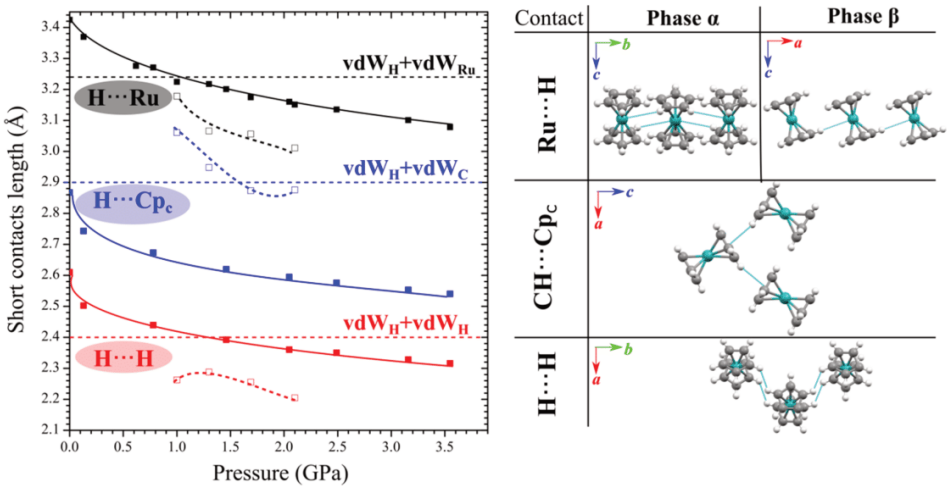

Figure 6. Compression of shortest contacts in $RuCp_2$ phases α (solid lines) and β (dashed lines): Ru···H (black), H···H (red), and H···Cp_c (blue). Horizontal dashed lines indicate the corresponding sums of van der Waals radii of H (1.2 Å),[33] C (1.7 Å),[33] and Ru (2.05 Å)[34] (cf. Figure S5 in the Supporting Information).

phase β (one molecule per a translation, as shown in Figure S5 in the Supporting Information).

The shortest Ru···H−C contacts are usually described as agostic bonds where the H atom approaches the bonding orbital electrons of the Ru atom. The geometric criteria for such agostic bonds are Ru···H distance shorter than 2.3 Å and Ru···H−C angle less than 140°.[43] Presently, no structures with such contacts are deposited in the Cambridge Structural Database (CSD),[44] but longer interactions denoted as agostic are known in the literature, for example, in H_2RuCH_2 (2.55 Å)[45] and carbonyl-chloro-hydrido-bis(tri-isopropylphosphine)-ruthenium(II) (2.32 Å).[46] The longer contacts, usually with angle Ru···H−C between 140 and 170°, are described as anagostic bonds (Figure 7). Although their geometry (the distance shorter than the sum of van der Waals radii) corresponds to classical hydrogen bonds, these latter involve electronegative H-donor atoms which contrasts with usually neutral CH groups.

Comparison of α-$RuCp_2$ and β-$RuCp_2$ with III-$FeCp_2$. The structures of ruthenocene α and ferrocene III are very similar in (i) the crystal symmetry (space group *Pnma*) and unit-cell dimensions, (ii) the positions and arrangement of molecules, and (iii) the eclipsed conformation of the molecules. The molecular orientation hardly differs between ruthenocene α and ferrocene III, either. Angle ψ between directions Fe−Cp_c and axis [z] in $FeCp_2$ at 98 K/0.1 MPa is 28.36(2)°, which is slightly smaller than that in ruthenocene α (Figure 8). Our results show that angle ψ in α-$RuCp_2$ weakly depends on pressure at a rate of −0.3°/GPa. However, the transition to β-$RuCp_2$ abruptly reduces angle ψ to circa 20° at 1 GPa and its pressure dependence is much stronger of −2.4°/GPa (Figure 8).

This strong ψ (p) dependence indicates that in β-$RuCp_2$, the molecular reorientation can efficiently release intramolecular strains induced by pressure. Moreover, the direction of the molecular reorientation opens the access to the Ru cation between the Cp rings on one side and on the other points the closest C−H bond of the neighboring molecule toward the Ru cation (Figure 8). This reorientation can be connected with the formation of anagostic C−H···Ru bonds. The C−H···Ru

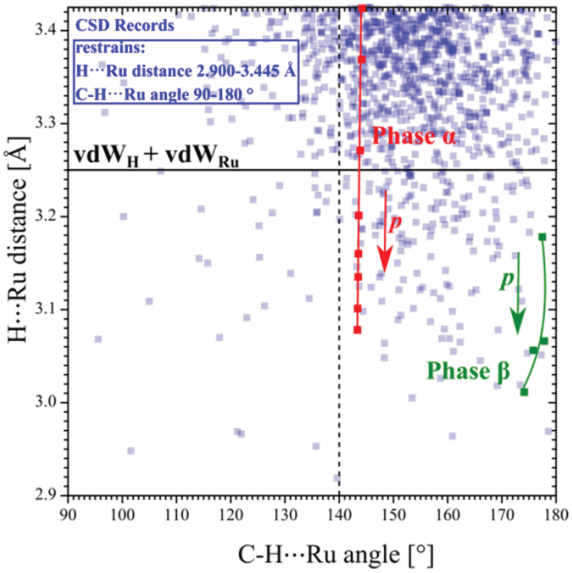

Figure 7. Scatter plot of C−H···Ru found among the CSD deposits[44] under boundary conditions H···Ru distance 2.900−3.445 Å and C−H···Ru angle between 90 and 180° (blue squares). Consecutive changes in the C−H···Ru dimensions with increasing pressure (arrows) are indicated for α-$RuCp_2$ (red) and β-$RuCp_2$ (green).

distances drastically shorten in β-$RuCp_2$ (Figure 6), while distances C−H···Cp_c become longer. Thus, the comparison can lead to the competition between hydrogen bonds C−H···π, favored in phase α, with anagostic bonds C−H···Ru favored in phase β. It should be noted that within each of the α-$RuCp_2$ and β-$RuCp_2$ phases, the only degree of freedom for structural changes involving the molecular orientation is angle ψ. This angle together with the intermolecular contacts is the microscopic structural effect resulting in the macroscopic compressibility.

https://doi.org/10.1021/acs.jpcc.1c10249
J. Phys. Chem. C 2022, 126, 5028−5035

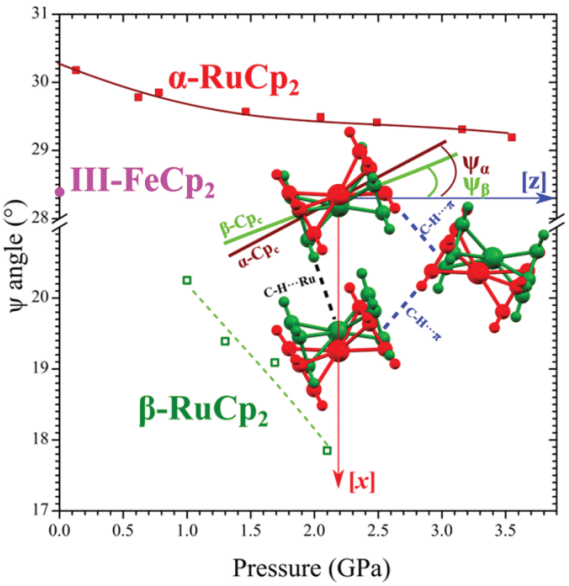

Figure 8. Angle ψ, between the molecular axis in the $RuCp_2$ phases and III-$FeCp_2$ (see the inset), plotted as a function of pressure. The purple point indicates the ψ angle in ferrocene phase III at 98 K.[12]

We have observed a clear effect of pressure on the molecular dimensions of the $RuCp_2$ molecule: the compression of the distance between the Cp ring and the Ru atom, as well as the changing inclination of the Cp rings. The Cp···Ru distance is strongly compressed in all the pressure range of phase α (Figure 9), but in phase β, the Cp···Ru distance initially sharply increases and then it asymptotically approaches the value of about 1.77 Å. This behavior coincides with the formation of short anagostic contacts C−H···Ru, which require the H atom

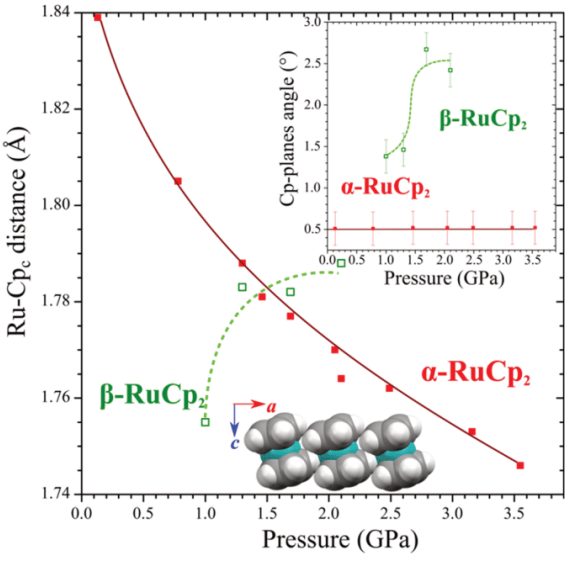

Figure 9. Ru−Cp_c distance plotted as a function of pressure. The insets show the Cp plane angle in one molecule and a space-filling model of C−H···Ru bonded chain in β-$RuCp_2$.

to penetrate between the Cp rings. Thus, the Cp rings are pushed apart by the H atom approaching the Ru^{2+} atom. At the same time, the Cp rings increase their inclination in phase β as they open up to facilitate the shortening of the anagostic CH··· Ru contact too. It contrasts with the pressure dependence of the angle between Cp rings in phase α, which is equal to 0.52 and practically pressure independent up to 3.6 GPa at least (see the inset in Figure 9).

CONCLUSIONS

Ruthenocene is the first simple metallocene, MCp_2, for which a phase transition does not involve any conformational changes. In both phases α and β, the $RuCp_2$ molecules are in the eclipsed conformation. This new β-ruthenocene polymorph is unprecedented for all groups of metallocenes MCp_2 investigated so far (Figure 1). On the other hand, both phases α and β of ruthenocene are strikingly similar: they are both orthorhombic, belonging to symmetry class *mmm*, the molecules are located on mirror planes, the unit-cell dimensions are similar, and the molecules are similarly inclined to the lattice directions. Consequently, the anisotropy of compressibilities of both phases is similar too. Moreover, $RuCp_2$ phases α and β can grow as concomitant, oriented nonidentical twins, with their corresponding lattice axes parallel. This feature resembles the oriented intergrown polytype forms but the differences in the lattice dimensions are larger for the $RuCp_2$ phases. This contrasts with the twinning law of identical twins, which are related by a nonidentical twins observed in ruthenocene, resembling the racemic twins of enantiomers, where all lattice axis superimpose too. The transformation between ruthenocene phases and the large hysteresis of this transformation are consistent with the competing cohesion forces specific for phases α and β. In phase α, the CH···π hydrogen bond has been clearly identified. These C−H···π bonds are weakened in phase β, where anagostic CH···Ru contacts become significantly shorter than in phase α. The competition between bonds C−H···π and C−H···Ru stabilizes the structures of phases α and β in the exceptionally wide hysteresis region from 0.7 to 3.9 GPa. A clear correlation between the molecular dimensions and anagostic CH···Ru bonds has been rationalized in the terms of steric hindrances involving H···Cp contacts. The strong energetic preference of $RuCp_2$ molecules for the eclipsed conformation prevents the transformation of ruthenocene to phase I′, which contrasts with ferrocene phases I, II, and III[47] and nickelocene phase I.[48]

ASSOCIATED CONTENT

Supporting Information

The Supporting Information is available free of charge at https://pubs.acs.org/doi/10.1021/acs.jpcc.1c10249.

Photographs of high-pressure in situ crystallization of ruthenocene phases α and β; PXRD patterns of $RuCp_2$ as a function of pressure; Gibbs energy analysis for the crystal structure of $RuCp_2$; C−H···Ru angle as a function of pressure, autostereograms of phases α and β with C−H···Ru contact description; comparison of C−H···π contacts in $RuCp_2$, $NiCp_2$, and $FeCp_2$; shortest C−H··· H contacts compared for $RuCp_2$ and $NiCp_2$; unwrap pictures for twinned crystals; Raman spectra of ruthenocene in DAC registered at three different

https://doi.org/10.1021/acs.jpcc.1c10249
J. Phys. Chem. C 2022, 126, 5028−5035

pressures; and experimental and crystal data for ruthenocene (PDF)

AUTHOR INFORMATION

Corresponding Author

Andrzej Katrusiak − *Department of Materials Chemistry, Faculty of Chemistry, Adam Mickiewicz University, 61-614 Poznań, Poland;* orcid.org/0000-0002-1439-7278; Phone: +48 61 829 1590; Email: katran@amu.edu.pl

Author

Ida Moszczyńska − *Department of Materials Chemistry, Faculty of Chemistry, Adam Mickiewicz University, 61-614 Poznań, Poland;* orcid.org/0000-0002-0791-2278

Complete contact information is available at: https://pubs.acs.org/10.1021/acs.jpcc.1c10249

Author Contributions

The manuscript was written through contributions of all authors. All authors have given approval to the final version of the manuscript.

Notes

The authors declare no competing financial interest.

ACKNOWLEDGMENTS

This study was supported by the Polish Ministry of Higher Education; I.M. is grateful to the Adam Mickiewicz University in Poznań for financial support, minigrant for PhD student 017/02/SNŚ/0018.

REFERENCES

(1) Bernstein, J.; Hagler, A. T. Conformational Polymorphism. The Influence of Crystal Structure on Molecular Conformation. *J. Am. Chem. Soc.* **1978**, *100*, 673−681.

(2) Bernstein, J. Conformational Polymorphism. III. The Crystal and Molecular Structures of Form II and Form III of Iminodiacetic Acid. *Acta Crystallogr., Sect. B: Struct. Crystallogr. Cryst. Chem.* **1979**, *35*, 360−366.

(3) Pfab, W.; Fischer, E. O. Zur Kristallstruktur der Di-cyclopentadienyl-verbindungen des zweiwertigen Eisens, Kobalts und Nickels. *ZAAC—J. Inorg. Gen. Chem.* **1953**, *274*, 316−322.

(4) Calvarin, G.; Weigel, D. Mise en évidence et étude, par diffraction des rayons X sur poudre, d'une transition ordre-désordre pour le nickelocène Ni(CSHS)2. *J. Appl. Crystallogr.* **1976**, *9*, 212−215.

(5) Seiler, P.; Dunitz, J. D. The Structure of Nickelocene at Room Temperature and at 101 K. *Acta Crystallogr., Sect. B: Struct. Crystallogr. Cryst. Chem.* **1980**, *36*, 2255−2260.

(6) Antipin, M. Y.; Boese, R. Structure of Vanadocene in the Temperature Interval 108-357 K and the Nature of the Ring Disorder. *Acta Crystallogr., Sect. B: Struct. Sci.* **1996**, *52*, 314−322.

(7) Weiss, E.; Fischer, E. O. Zur Kristallstruktur von Di-Cyclopentadienyl-Chrom(II). *Z. Anorg. Allg. Chem.* **1956**, *284*, 69−72.

(8) Antipin, M. Y.; Boese, R.; Augart, N.; Schmid, G. Redetermination of the Cobaltocene Crystal Structure at 100 K and 297 K: Comparison with Ferrocene and Nickelocene. *Struct. Chem.* **1993**, *4*, 91−101.

(9) Bünder, W.; Weiss, E. Verfeinerung Der Kristallstruktur von Dicyclopentadienylmagnesium, $(\eta\text{-}C_5H_5)_2Mg$. *J. Organomet. Chem.* **1975**, *92*, 1−6.

(10) Hardgrove, G. L.; Templeton, D. H. The Crystal Structure of Ruthenocene. *Acta Crystallogr.* **1959**, *12*, 28−32.

(11) Bobyens, J. C. A.; Levendis, D. C.; Bruce, M. I.; Williams, M. L. Crystal structure of osmocene, Os(?-C5H5)2. *J. Crystallogr. Spectrosc. Res.* **1986**, *16*, 519−524.

(12) Seiler, P.; Dunitz, J. D. Low-Temperature Crystallization of Orthorhombic Ferrocene: Structure Analysis at 98 K. *Acta Crystallogr., Sect. B: Struct. Crystallogr. Cryst. Chem.* **1982**, *38*, 1741−1745.

(13) Doman, T. N.; Landis, C. R.; Bosnich, B. Molecular Mechanics Force Fields for Linear Metallocenes. *J. Am. Chem. Soc.* **1992**, *114*, 7264−7272.

(14) Rayón, V. M.; Frenking, G. Bis (Benzene) Chromium Is a δ-Bonded Molecule and Ferrocene Is a π-Bonded Molecule. *Organometallics* **2003**, *22*, 3304−3308.

(15) Green, J. C. Bent Metallocenes Revisited. *Chem. Soc. Rev.* **1998**, *27*, 263−271.

(16) Atwood, J. L.; Hunter, W. E.; Cowley, A. H.; Jones, R. A.; Stewart, C. A. X-Ray Crystal Structures of Bis(Cyclopentadienyl)Tin and Bis(Pentamethylcyclopentadienyl)Lead. *J. Chem. Soc., Chem. Commun.* **1981**, *17*, 925−927.

(17) Grenz, M.; Hahn, E.; du Mont, W.-W.; Pickardt, J. Novel Structures Containing Germanium(II): Germanocene Dimeric Tricarbonyl(Di-Tert-Butoxygermylene)Nickel(0). *Angew. Chem., Int. Ed. Engl.* **1984**, *23*, 61−63.

(18) Beswick, M. A.; Palmer, J. S.; Wright, D. S. p-Block metallocenes: the other side of the coin. *Chem. Soc. Rev.* **1998**, *27*, 225.

(19) Azokpota, C.; Pommier, C.; Berar, J. F.; Calvarin, G. Etudes Calorimetrique et Radiocristallographique Du Cobaltocene et Du Ruthenocene Entre 77 et 298 K. *J. Organomet. Chem.* **1977**, *135*, 125−135.

(20) Fumagalli, A.; Koetzle, T. F.; Takusagawa, F.; Chini, P.; Martinengo, S.; Heaton, B. T. Isolation and Characterization of Penta-.Mu.2-Carbonyl-Decacarbonylpentarhodate(1-): A Key Product in Rhodium Carbonyl Chemistry. *J. Am. Chem. Soc.* **1980**, *102*, 1740−1742.

(21) Merrill, L.; Bassett, W. A. Miniature diamond anvil pressure cell for single crystal x-ray diffraction studies. *Rev. Sci. Instrum.* **1974**, *45*, 290−294.

(22) Piermarini, G. J.; Block, S.; Barnett, J. D.; Forman, R. A. Calibration of the pressure dependence of theR1ruby fluorescence line to 195 kbar. *J. Appl. Phys.* **1975**, *46*, 2774−2780.

(23) Dziubek, K. F.; Jęczmiński, D.; Katrusiak, A. Pressure-Generated Hydrogen Bonds and the Role of Subtle Molecular Features in Tetrahydrofuran. *J. Phys. Chem. Lett.* **2010**, *1*, 844−849.

(24) Kahlenberg, V.; Krüger, H.; Goettgens, V. S. Structural Elucidation of Triclinic and Monoclinic SFCA-III - Killing Two Birds with One Stone. *Acta Crystallogr., Sect. B: Struct. Sci., Cryst. Eng. Mater.* **2019**, *75*, 1126−1136.

(25) Palosz, B.; Stel'makh, S.; Gierlotka, S. Refinement of Polycrystalline Disordered Cubic Silicon Carbide by Structure Modeling and X-Ray Diffraction Simulation. *Z. Kristallogr. N. Cryst. Struct.* **1995**, *210*, 731−740.

(26) Katrusiak, A. Shadowing and Absorption Corrections of Single-Crystal High-Pressure Data. *Z. Kristallogr.* **2004**, *219*, 461−467.

(27) Budzianowski, A.; Katrusiak, A. High-Pressure Crystallographic Experiments with a CCD-Detector. *High-Pressure Crystallography*; Springer Netherlands: Dordrecht, 2004; Vol. *140*, pp 101−112.

(28) Sheldrick, G. M. Crystal structure refinement withSHELXL. *Acta Crystallogr., Sect. C: Struct. Chem.* **2015**, *71*, 3−8.

(29) Dolomanov, O. V.; Bourhis, L. J.; Gildea, R. J.; Howard, J. A. K.; Puschmann, H. OLEX2: a complete structure solution, refinement and analysis program. *J. Appl. Crystallogr.* **2009**, *42*, 339−341.

(30) Paliwoda, D.; Kowalska, K.; Hanfland, M.; Katrusiak, A. U-Turn Compression to a New Isostructural Ferrocene Phase. *J. Phys. Chem. Lett.* **2013**, *4*, 4032−4037.

(31) Safari, F.; Katrusiak, A. Structure-property relationships of molecular shape and orientation with compression and expansion of xylitol. *Acta Crystallogr., Sect. B: Struct. Sci., Cryst. Eng. Mater.* **2021**, *77*, 205−210.

(32) Kaźmierczak, M.; Katrusiak, A. Bimodal Distribution of the Shortest Intermolecular Contacts in Crystals of Organic Compounds. *Cryst. Growth Des.* **2014**, *14*, 2223−2229.
(33) Bondi, A. Van Der Waals Volumes and Radii. *J. Phys. Chem.* **1964**, *68*, 441−451.
(34) Batsanov, S. S. Van Der Waals Radii of Elements. *Inorg. Mater.* **2001**, *37*, 871−885.
(35) Epstein, L. M.; Shubina, E. S. New Types of Hydrogen Bonding in Organometallic Chemistry. *Coord. Chem. Rev.* **2002**, *231*, 165−181.
(36) Brookhart, M.; Green, M. L. H.; Parkin, G. Agostic Interactions in Transition Metal Compounds. *Proc. Natl. Acad. Sci.* **2007**, *104*, 6908−6914.
(37) Sundquist, W. I.; Bancroft, D. P.; Lippard, S. J. Synthesis, Characterization, and Biological Activity of Cis-Diammineplatinum-(II) Complexes of the DNA Intercalators 9-Aminoacridine and Chloroquine. *J. Am. Chem. Soc.* **1990**, *112*, 1590−1596.
(38) Braga, D.; Grepioni, F.; Tedesco, E.; Biradha, K.; Desiraju, G. R. Hydrogen Bonding in Organometallic Crystals. 6. X−H—M Hydrogen Bonds and M—(H−X) Pseudo-Agostic Bonds. *Organometallics* **1997**, *16*, 1846−1856.
(39) Brammer, L. Metals and Hydrogen Bonds. *Dalton. Trans.* **2003**, 3145−3157.
(40) Shubina, E. S.; Belkova, N. V.; Epstein, L. M. Novel types of hydrogen bonding with transition metal π-complexes and hydrides. *J. Organomet. Chem.* **1997**, *536*−*537*, 17−29.
(41) Levendis, D. C.; Boeyens, J. C. A. Analysis of the Molecular Conformation and Rotational Disorder in Crystalline Ferrocene and Nickelocene. *J. Crystallogr. Spectrosc. Res.* **1985**, *15*, 1−17.
(42) Borissova, A. O.; Antipin, M. Y.; Perekalin, D. S.; Lyssenko, K. A. Crucial role of Ru···H interactions in the crystal packing of ruthenocene and its derivatives. *CrystEngComm* **2008**, *10*, 827−832.
(43) Zhang, Y.; Lewis, J. C.; Bergman, R. G.; Ellman, J. A.; Oldfield, E. NMR Shifts, Orbitals, and M···H−X Bonding in d8 Square Planar Metal Complexes. *Organometallics* **2006**, *25*, 3515−3519.
(44) Groom, C. R.; Bruno, I. J.; Lightfoot, M. P.; Ward, S. C. The Cambridge Structural Database. *Acta Crystallogr., Sect. B: Struct. Sci., Cryst. Eng. Mater.* **2016**, *72*, 171−179.
(45) Roos, B. O.; Lindh, R.; Cho, H.-G.; Andrews, L. Agostic Interaction in the Methylidene Metal Dihydride Complexes H2MCH2 (M = Y, Zr, Nb, Mo, Ru, Th, or U). *J. Phys. Chem. A* **2007**, *111*, 6420−6424.
(46) Huang, D.; Streib, W. E.; Bollinger, J. C.; Caulton, K. G.; Winter, R. F.; Scheiring, T. 14-Electron Four-Coordinate Ru(II) Carbyl Complexes and Their Five-Coordinate Precursors: Synthesis, Double Agostic Interactions, and Reactivity. *J. Am. Chem. Soc.* **1999**, *121*, 8087−8097.
(47) Paliwoda, D.; Hanfland, M.; Katrusiak, A. Pressure-Enhanced Environment Effects in Ferrocene Phases. *J. Phys. Chem. C* **2019**, *123*, 25719−25723.
(48) Moszczyńska, I.; Katrusiak, A. Lattice-Strain Coupled to Molecular Conformation and Disorder in Compressed Nickelocene. *J. Phys. Chem. C* **2021**, *125*, 15670−15675.

https://doi.org/10.1021/acs.jpcc.1c10249
J. Phys. Chem. C 2022, 126, 5028−5035

Artykuł 4

Ida Moszczyńska, Iwona Gulaczyk, Andrzej Katrusiak

Giant Deformation between Osmocene Phases Induced by Anagostic Bonds Promoted under High Pressure
***J. Phys. Chem C,* 2023, *127 (38)*, 19250-19257**

THE JOURNAL OF PHYSICAL CHEMISTRY C
A JOURNAL OF THE AMERICAN CHEMICAL SOCIETY

pubs.acs.org/JPCC
Article

Giant Deformation between Osmocene Phases Induced by Anagostic Bonds Promoted under High Pressure

Ida Moszczyńska, Iwona Gulaczyk, and Andrzej Katrusiak*

Cite This: J. Phys. Chem. C 2023, 127, 19250−19257

Read Online

ACCESS | Metrics & More | Article Recommendations | Supporting Information

ABSTRACT: Above 3.6 GPa, osmocene, α-Os$(C_5H_5)_2$, transforms to the new phase β-Os$(C_5H_5)_2$, unprecedented among prototypic metallocenes $M(C_5H_5)_2$. Despite the isostructural ambient-pressure phases of osmocene α-Os$(C_5H_5)_2$ and ruthenocene α-Ru$(C_5H_5)_2$, the high pressure differentiates the symmetry of phases β-Os$(C_5H_5)_2$ and β-Ru$(C_5H_5)_2$ and the patterns of intermolecular anagostic bonds CH···M in their structures. The formation of CH···Os bonds in β-Os$(C_5H_5)_2$ and their breaking on the transition to α-Os$(C_5H_5)_2$ result in an exceptionally wide pressure hysteresis, extending between 0.3 and 3.6 GPa. In β-Os$(C_5H_5)_2$, each molecule is the H-donor of four and the H-acceptor of other four of eight CH···Os bonds, compared to the capabilities of one H-donor and one H-acceptor of each molecule in β-Ru$(C_5H_5)_2$. The mechanism combining the competition of hydrogen bonds CH···π with anagostic bonds CH···Os, the molecular conformation, and the pressure-induced phase transitions in ferrocene, ruthenocene, and osmocene is explained.

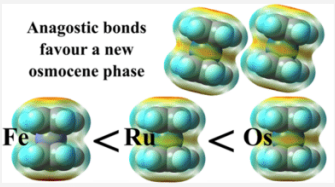

INTRODUCTION

Ferrocene ($FeCp_2$, where Cp denotes the cyclopentadienyl ring), ruthenocene ($RuCp_2$), and osmocene ($OsCp_2$) form the group of prototypic stable metallocenes, fulfilling the rule of 18-electrons. Under ambient conditions, their structures are stabilized by hydrogen bonds CH···π. High-pressure studies of $FeCp_2$ and $RuCp_2$ revealed new phases of these compounds.[1,2] In ferrocene phase I at ambient conditions, the conformationally disordered molecules are aggregated by hydrogen bonds CH···π, which continue to prevail above 3.2 GPa in the structure of ferrocene phase I′, where the ordered staggered conformers are present. Otherwise, ferrocene phases I and I′ are isostructural, both of monoclinic space group ($P2_1/n$). Low-temperature ferrocene phase III (orthorhombic space group $Pnma$)[3] is isostructural with the ambient phases of ruthenocene[4] and osmocene,[5] where the molecules assume the eclipsed conformation. At 3.9 GPa, ruthenocene transforms to a new phase β-$RuCp_2$, retaining the eclipsed conformers but eliminating hydrogen bonds CH···π dominating the ambient-pressure structure.[2] In their stead, anagostic bonds CH···Ru are formed. Their formation increases the molecular bending angle Cp_{c1}−Ru−Cp_{c2} from 179.53° in α-$RuCp_2$ (Cp_{c1} and Cp_{c2} are centroids of rings Cp_1 and Cp_2, respectively) to 178.98° in β-$RuCp_2$. This bending angle generates a molecular electric dipole due to the displacement of the dication and anionic Cp rings along the direction perpendicular to the pseudo-C_5-symmetry axis. Consequently, the dipole−dipole forces contribute to intermolecular interactions. The energies of differently aggregated dimers of ferrocene, ruthenocene, and osmocene were calculated by Vargas−Caamal et al.[6] The ruthenocene phase β (orthorhombic space group $Pcmb$)[2] was unprecedented among metallocenes so far.[3,7−9] Thus, it was natural to ask if osmocene, isostructural with α-ruthenocene at ambient conditions, transforms to a high-pressure phase of this symmetry, too. The main aim of our present study on $OsCp_2$ was to investigate its high-pressure behavior. On the one hand, the very similar ambient-pressure phases α-$RuCp_2$ and α-$OsCp_2$, both dominated by CH···π bonds between the eclipsed energetically favored conformers, suggested that the phase diagrams of these compounds were similar. On the other hand, the different thermodynamic transformations of isostructural phases can reveal subtle differences in the properties of analogous compounds. For example, the high-pressure behavior of $FeCp_2$ and $NiCp_2$ is similar, as they both[1,8,9] transform isostructurally within the space group $P2_1/n$ to analogous phases I′. However, $FeCp_2$ and $NiCp_2$ transform differently on decreasing the temperature.[10−12] In any of their phases, no anagostic CH···M bonds are formed. The $FeCp_2$-III structure is similar to α-$RuCp_2$, but all distances H···Fe are at least 0.1 Å longer than the sum of van der Waals radii, 3.18 Å according to Bondi.[13,14] Also, in $FeCp_2$ phases I and II, and even in phase I′ up to 38 GPa, no short anagostic type of Fe···H contacts are present. In the ambient phase α of ruthenocene,[4] bonds CH···π are considerably shorter than contacts CH···Ru, but in the high-pressure-phase β-$RuCp_2$, anagostic bonds CH···Ru are the shortest contacts, while contacts CH···π become longer than the sums of van der Waals radii.[2] Thus, it appears that high pressure strongly favors

Received: July 7, 2023
Revised: August 25, 2023
Published: September 13, 2023

https://doi.org/10.1021/acs.jpcc.3c04579
J. Phys. Chem. C 2023, 127, 19250−19257

anagostic bonds CH···*M* and this dependence is presently being further investigated for osmocene.

METHODS

Both Raman and X-ray experiments on osmocene were performed in a Merrill−Basset diamond anvil cell (DAC)[15] modified by mounting the anvils directly on the edges of steel backing plates with conical windows. The pressure was calibrated by the ruby fluorescence shift method[16] before and after the diffraction and spectroscopic experiments. This method and the resolution of our Photon Control spectrometer afford an accuracy of about 0.02 GPa.

The Raman experiments were measured for the polycrystalline sample compressed in a DAC equipped with low-fluorescence synthetic IIA diamond anvils with a Hamamatsu Photonic multichannel detector and a laser M266 from Solar Laser Systems with an excitation wavelength of 785 nm. A methanol/ethanol/water (MEW) mixture (16:3:1 vol) was used as the hydrostatic pressure-transmitting medium.

Our compression experiments on the pulverized $OsCp_2$ sample and subsequent powder X-ray diffraction (pXrd, *cf.* Figure S1 in the Supporting Information) showed that the ambient-pressure phase α-$OsCp_2$ persists up to 3.6 GPa when it transforms to a new phase β. The single-crystal X-ray diffraction (scXrd) experiments confirmed that phase α can be compressed until 3.6 GPa, but the transition shattered the single crystals into small pieces (Figure 1).

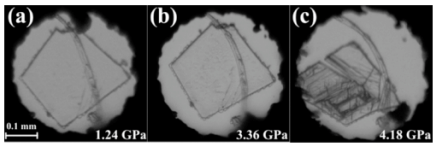

Figure 1. Compression of an α-$OsCp_2$ single crystal at room temperature to (a) 1.24 GPa, (b) 3.36 GPa, and (c) 4.18 GPa, when the crystal is broken after the transition to phase β at 3.6 GPa. Several small ruby chips lie close to the gasket edge in the DAC chamber.

In order to obtain a good-quality single crystal of phase β, we undertook its high-pressure in situ crystallization. Like for ruthenocene,[2] we grew single crystals from the tetrahydrofuran (THF) solution. Up to 1.5 GPa, the in situ crystallization of osmocene yielded crystals of phase α only (Figure 2). At 296 K, THF freezes at 2.24 GPa.[17] Therefore, the single crystals of phase β were grown by the method of high-pressure nucleation in the following steps: (i) the polycrystalline sample was compressed in THF to about 4.0 GPa, i.e., above the transition to phase β; (ii) the pressure was reduced to 0.5 GPa, insufficient to trigger the reverse transition; (iii) all but one crystal grain was dissolved by heating the sample; and (iv) from this one seed, a single crystal of phase β was grown in isochoric conditions (Figure 3). This method of in situ high-pressure nucleation was used previously for obtaining the single crystals of $RuCp_2$ β-phase.[2] On releasing pressure, the crystals remain in phase β down to 0.3 GPa, when they transform back to phase α (*cf.* Figures 3 and S2 in the Supporting Information).

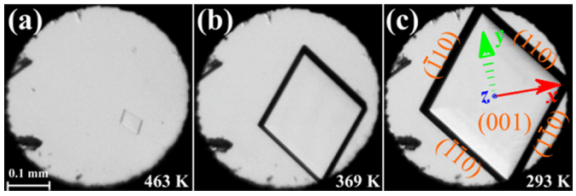

Figure 2. Isochoric in situ recrystallization of α-$OsCp_2$: (a) 463 K, (b) 369 K, and (c) 296 K/0.35 GPa. Two ruby chips are placed near the left edge of the gasket. The crystal axes and Miller indices of faces are indicated in (c).

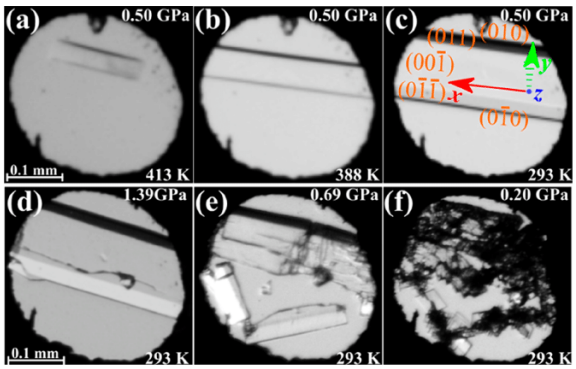

Figure 3. Photos (a)−(c) show the isochoric growth of a single crystal of β-$OsCp_2$ from one of the seeds nucleated above 3.6 GPa/296 K: (a) one seed left after reducing pressure to 0.5 GPa and heating the sample to 413 K; (b) the crystal at 388 K and (c) at 293 K/0.5 GPa. Photos (d) and (e) show the isothermal decompression of the β-$OsCp_2$ crystal and (f) the small crystal pieces at 0.2 GPa, after the transition to phase α. Several ruby chips lie close to the gasket, and one moves around the chamber. The crystal axes and Miller indices of faces are indicated in (c).

The scXrd data for the compressed $OsCp_2$ samples were measured on a KUMA KM-4 CCD 4-circle diffractometer, while the pXrd data were recorded on an Excalibur EOS diffractometer, both using Mo Kα radiation. The scXrd and pXrd experiments and preliminary data reduction were performed with CrysAlis software.[18] Corrections for the DAC absorption, sample shadowing by the gasket, and sample absorption were calculated, and diamond reflections were eliminated.[19,20] The crystal structures of phase α at ambient conditions and of phase β at 1.0 GPa were solved by direct methods of Shelxs and refined by full-matrix least-squares on F^2's with Shelxl,[21] operated through Olex 2.[22] Then, these structures were used as the starting models for the higher-pressure experiments. The H atoms were ideally located from the Cp ring geometry (AFIX 43 and C−H distances of 0.93 Å). The crystallographic information about the phases of $OsCp_2$ is summarized in Table 1 and detailed in Table S1 in the Supporting Information (SI). We have applied a non-conventional setting of the space group *Pcab* for describing the symmetry of phase β-$OsCp_2$ (*cf.* Table 1) in order to facilitate its comparison with the structure of phase α.

The internal energy for the structures of phases α-$OsCp_2$ and β-$OsCp_2$, as well as the conformational energy of molecules, was calculated by Gaussian 16W software using the density functional theory (DFT) method with the standard double-ζ LANL2DZ basis set for Os, Ru, and Fe, while the SDD basis set associated with pseudopotential and the D95 basis set were used for C and H, respectively.[23−25] All of the DFT calculations were carried out using the Perdew−Burke−

https://doi.org/10.1021/acs.jpcc.3c04579
J. Phys. Chem. C 2023, 127, 19250−19257

Table 1. Selected Crystallographic Data of $OsCp_2$ Phases α and β[a]

pressure (GPa)		0.14	2.3	0.5	1.78
phase		α	α	β	β
space group[b]		*Pnma*	*Pnma*	*Pcab*	*Pcab*
unit cell (Å)	*a*	7.0109(2)	6.6513(2)	11.2020(4)	10.8976(4)
	b	8.8334(2)	8.4446(3)	9.8404(3)	9.5556(3)
	c	12.755(12)	12.447(14)	13.802(14)	13.521(14)
V (Å^3)		789.9(7)	699.1(8)	1521.4(15)	1408.0(15)
Z/*Z*′		4/0.5	4/0.5	8/1	8/1
density (g cm^{-3})		2.694	3.044	2.797	3.023

[a] *cf.* Table S1 with 13 high-pressure structures of $OsCp_2$ in the Supporting Information. [b] Nonstandard setting of space group No.61, *Pbca*, has been applied to phase β.

Ernzerhof (PBE) functional in Gaussian 16W. The periodic boundary conditions,[26] reproducing the translation vectors in the crystal structures, were applied.

RESULTS AND DISCUSSION

Our Raman spectroscopy, as well as powder and single-crystal X-ray diffraction experiments, shows that α-$OsCp_2$ can be compressed up to 3.6 GPa when it transforms to phase β. The β-phase can be decompressed down to 0.3 GPa when it transforms back to phase α. The structure of phase α has been determined in all its stability and hysteresis range up to 3.6 GPa, while the structure of high-pressure phase β has been determined between 0.5 and 2.0 GPa. This upper limit of the β-phase determination by scXrd was due to the crystallization of THF at 2.24 GPa,[17] which distorted the hydrostatic conditions and destroyed the single crystals.

High-Pressure Phase of Osmocene. The ambient-pressure phases of α-$RuCp_2$ and α-$OsCp_2$ resemble each other because (i) they are isostructural; (ii) their structures are stabilized mainly by CH···π bonds; and (iii) the morphology of crystals of phases α-$RuCp_2$ and α-$OsCp_2$ is very similar (compare Figures 2 and 3 with Figures 2 and 3 in ref 2). There are also similarities in the pressure-induced phase transitions of osmocene and ruthenocene and in the structures and morphologies of their high-pressure phases, β-$RuCp_2$ and β-$OsCp_2$. However, phases β-$RuCp_2$ and β-$OsCp_2$ differ in their space group symmetries and in the symmetry of molecular sites. In phase β-$RuCp_2$, the molecule lies on the mirror plane, and the molecular conformation is precisely eclipsed, whereas in β-$OsCp_2$, the molecule lies in a general position, so the symmetry does not interfere with the molecular conformation, but it only marginally diverts from the eclipsed conformation (Figure S3 in the Supporting Information). The angle Cp_{c1}−Os−Cp_{c2} is bent by about 1° (Figure S4 in the Supporting Information). The absence of mirror planes in the structure of phase β-$OsCp_2$ is mainly due to the rotations of the eclipsed conformers by 14.5° at 0.5 GPa (Figure S5 in the Supporting Information).

The unit-cell dimensions of α-$RuCp_2$ and α-$OsCp_2$ crystals are very similar, and they compress very similarly, too. In both these compounds, the most compressed are parameters a_α, intermediate compressed are parameters b_α, and the least compressed are parameters c_α (the Greek subscripts refer to the phase label). The compression of phase α-$OsCp_2$ is clearly nonlinear (Figure 4), which is characteristic of molecular crystals. Anagostic-like contacts between molecules along the [*y*] direction (Figures S6 and S7 in the Supporting Information) are more compressible than H-bonds CH···π, connecting the osmocene molecule along the [*z*] direction (Figure 5).

As a consequence of the similar structures, molecular shape, and interactions, the deformations of the $OsCp_2$ and $RuCp_2$ crystals at their transitions to phase β and then the compressions of phases β-$OsCp_2$ and β-$RuCp_2$ are very similar. The abrupt deformation of the crystal of $OsCp_2$ is very strong: in the β phase, the crystal becomes shorter by over 20% along [*x*] and longer by over 10 and 8% along [*y*] and [*z*], respectively (Figure 4b). The magnitudes of the deformations of $RuCp_2$ are equally large.

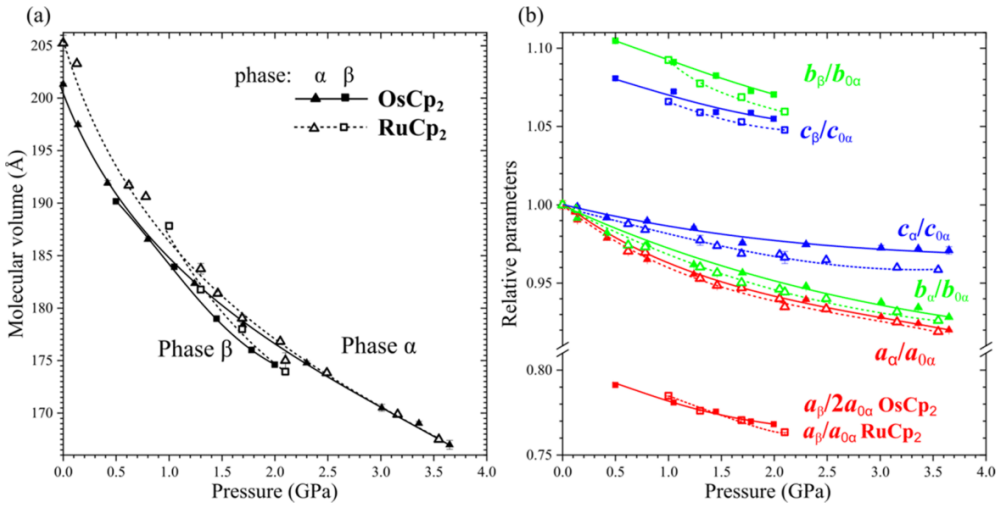

Figure 4. Compression of osmocene (full symbols), phase α (squares), and phase β (triangles): (a) the molecular volume and (b) unit cell parameters related to the ambient pressure values of phase α at 0.1 MPa/296 K. For comparison, the compressibility of ruthenocene (open symbols, dotted lines) is indicated.

https://doi.org/10.1021/acs.jpcc.3c04579
J. Phys. Chem. C 2023, 127, 19250−19257

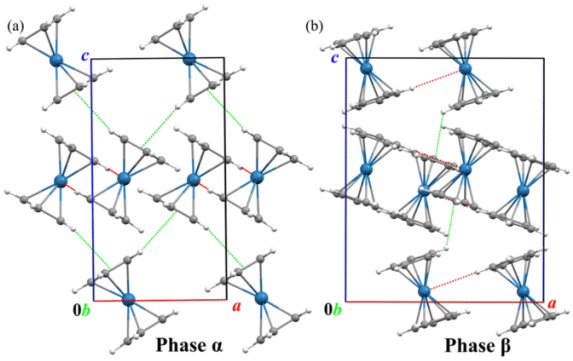

Figure 5. Crystal structures of osmocene projected down direction [010]: (a) phase α at 0.14 GPa and (b) phase β at 0.50 GPa. The shortest contacts CH···M and CH···π are indicated with dotted red and green lines, respectively. Note the corresponding set of eight molecules in (a) two unit cells of phase α and (b) one unit cell of phase β.

Transitions between Phases α and β in $RuCp_2$ and $OsCp_2$. The similarities in the pressure stability regions of phases α and β, their compression, and the deformation between the phases of osmocene and ruthenocene can be rationalized by the high-pressure stimulated increased role of anagostic bonds CH···M. However, a significant difference is that in β-$OsCp_2$, the mirror planes disappear and the unit cell is doubled along direction [x] (Figures S8 and S9 in the Supporting Information). The symmetry of mirror planes is broken because the molecules are rotated by *ca.* 14° from this plane to the position best exposing the Os atom to four H atoms of neighboring molecules. In phase β-$OsCp_2$, each Os atom becomes the H-acceptor of four anagostic bonds. As shown in Figure 6, each of these four anagostic bonds is located between two opposing C−C bonds, nearly parallel in the eclipsed Cp rings.

Thus, in phase β, four anagostic CH···Os bonds can be formed in the favored directions after the molecules rotate by about 14° at 0.5 GPa (this molecular rotation is denoted as angle φ and plotted vs pressure in Figure S5 in the Supporting Information), opening the best access to the Os acceptor. This rotation breaks the symmetry of the mirror plane present in phase α, which restricts the molecules in the position optimal for only one short anagostic contact CH···Os. In β-$RuCp_2$, the only anagostic contact CH···Ru shorter than the sum of van der Waals radii is formed along the mirror plane directed between the C−C bonds of Cp rings, while other Ru···H distances are ca. 0.6 Å longer (Figures 6 and S10 in the Supporting Information). In β-$OsCp_2$, for each Os atom, four intermolecular contacts Os···H are shorter than the sum of van der Waals radii, 3.36 Å,[13,27] (Figures 6 and 7). Noteworthy, the rotation angle φ in β-$OsCp_2$ decreases with increasing pressure to about 8° at 0.5 GPa (*cf.* Figure S5), which is an indication of a competition between the directional anagostic CH···Os bonds and nondirectional London forces for the molecular arrangement in the compressed structure. The London interactions in the approximately C_s-symmetric crystal environment of molecules tend to reduce the inclination to the pseudo-mirror plane, substituted by the glide plane a perpendicular to the crystal [y] axis (*cf.* Table 1 and Figure 6). An analogical effect of C_i-symmetric crystal field was observed in the structure of disordered ferrocene phase I and nickelocene phase I, where high pressure increased the intermolecular interactions and induced the transition of these crystals to the ordered phases I′ with all the molecules in the staggered, i.e., energetically unfavorable conformation.

This is apparent that in both high-pressure phases β-$OsCp_2$ and β-$RuCp_2$, the anagostic bonds are favored, but under high pressure, the H-acceptor capacity of the H-bonded crystalline structure of Os becomes four times higher than that of Ru. In order to understand the different H-acceptor capacities of the $OsCp_2$ and $RuCp_2$ molecules, we have calculated their electrostatic potential (Figure 8).

It can be observed that in the series of ferrocene, ruthenocene, and osmocene, the negative electrostatic potential on the metal center sandwiched between Cp rings becomes increasingly more negative (Figure 8) and that this electrostatic potential is more negative for the eclipsed than that for the staggered conformers (Figure S10 in the Supporting Information). The highest negative electrostatic potential in β-$OsCp_2$ coincides with its 4-fold H-acceptor capacity. Moreover, we established that the electrostatic potential on the molecular surface of the Os and Ru atoms decreases with increasing pressure in all of the $OsCp_2$ and $RuCp_2$ planes (Figure S11 in the Supporting Information), which increases the H-accepting capability of the Os and Ru cations under high pressure. Thus, the phase transition and the

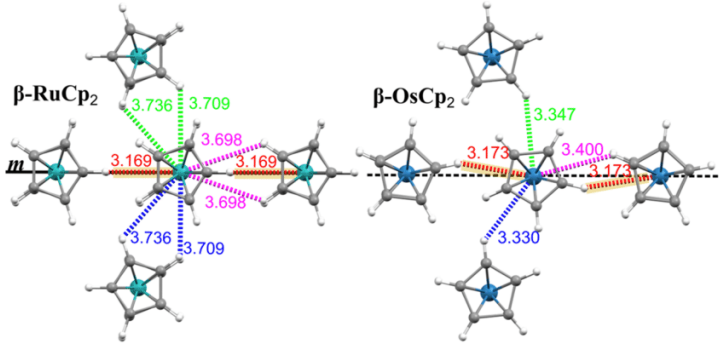

Figure 6. Anagostic CH···M bonds in β-$RuCp_2$ at 1.00 GPa and in β-$OsCp_2$ at 1.05 GPa. The interacting molecules are viewed along their axes, lying in the mirror planes for ruthenocene and close to the glide plane a for osmocene. The distances (Å) are indicated in colors used for plotting the distances in Figure 7.

https://doi.org/10.1021/acs.jpcc.3c04579
J. Phys. Chem. C 2023, 127, 19250−19257

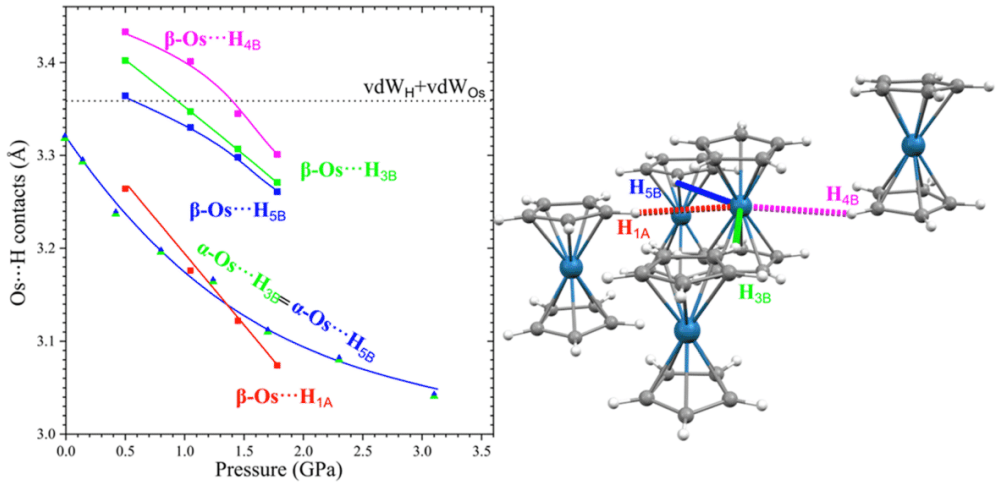

Figure 7. The H-acceptor molecule and its four H-donors for anagostic CH···Os bonds in β-$OsCp_2$ at 0.5 GPa. Shortest distances, Os···H_{1A} (red), Os···H_{5B} (blue), Os···H_{3B} (green), and Os···H_{4B} (purple), plotted as a function of pressure for α-$OsCp_2$ (triangles) and β-$OsCp_2$ (squares). The symmetry-equivalent distances in phase α are labeled with the corresponding H atoms of phase β indicated with atomic labels in the structural fragment. The sum of van der Waals radii of Os and H is marked by the horizontal dotted line (vdW_H = 1.20 Å after Bondi[13] and vdW_{Os} = 2.16 Å after Hu).[27] All ESDs are smaller than the plotted symbols.

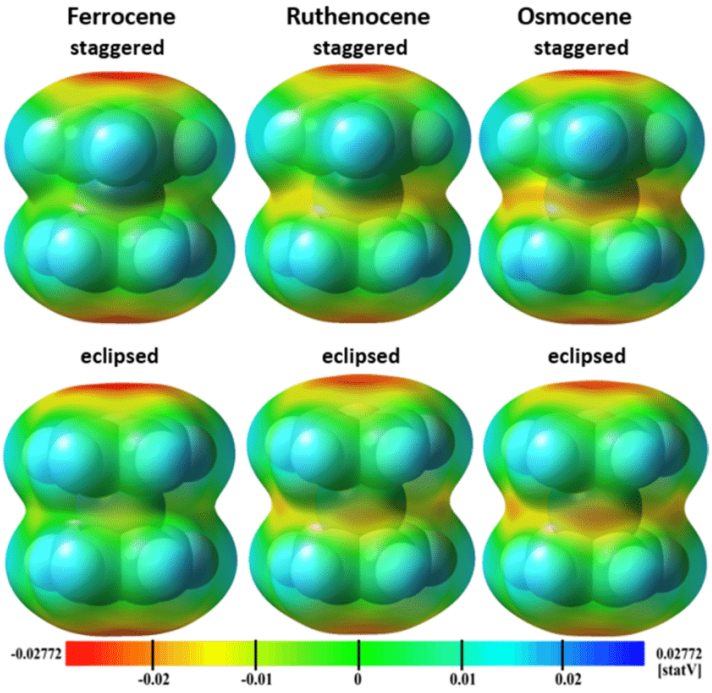

Figure 8. Electrostatic potential mapped on the molecular surface of isolated ferrocene, ruthenocene, and osmocene staggered and eclipsed conformers (*cf.* Figure S12 in the Supporting Information).

structure of β-$OsCp_2$ are directly connected with the pressure-promoted anagostic bonds CH···Os. Moreover, the potential on metal centers becomes increasingly negative with compression (*cf.* Figure S11 in the Supporting Information), which is consistent with the preference for anagostic bonds CH···*M* in the compressed $RuCp_2$ and $OsCp_2$ crystals.

The scatter plots for structures with CH···Os and CH···Ru contacts deposited in the Cambridge Structural Database (CSD)[28] (Figure 9) show similar weak correlations between the distances and CH···*M* angles, albeit in the CSD, there are 9 times fewer structures with Os, H, and C atoms than those with Ru. When taking into account these different numbers of deposits, it can be concluded that the CH···Os bonds are twice as frequent compared to CH···Ru bonds.

The scatter plots in Figure 9 show a very similar pressure dependence of the distance−angle correlation between CH···

https://doi.org/10.1021/acs.jpcc.3c04579
J. Phys. Chem. C 2023, 127, 19250−19257

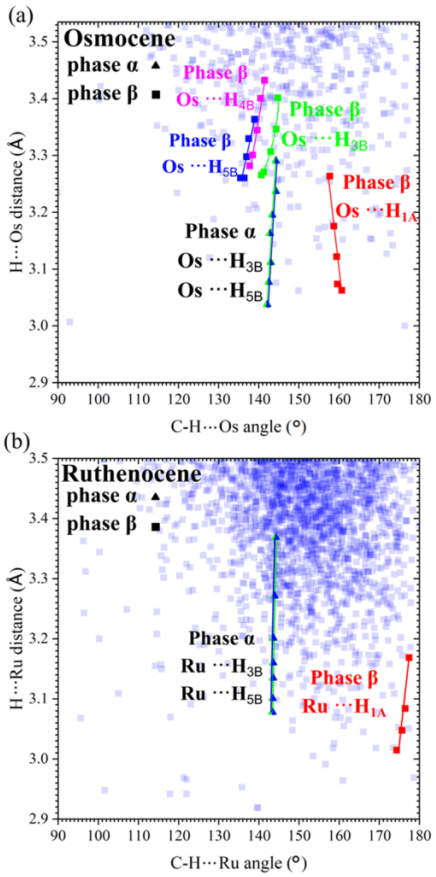

Figure 9. Scatter plots of intermolecular contacts (a) C−H···Os and (b) C−H···Ru found in the CSD deposites[28] fulfilling the conditions of angle 90° < CH···Os/Ru < 180° and distance 2.9 Å < H···Os/Ru < sum of van der Waals radii +0.175 Å (blue squares). The pressure-induced changes in these dimensions are indicated for α phases with triangles and for β phases with squares for osmocene (a) and ruthenocene (b).

Os and CH···Ru bonds in α-$OsCp_2$ and α-$RuCp_2$: the H···M distance is compressed by about 0.3 Å, while the C−H···M angle hardly changes between 140 and 145°. However, the distance−angle correlation for the β phases is different: in β-$OsCp_2$, four independent CH···Os bonds are bent to about 140−160°, whereas in β-$RuCp_2$, the one independent CH···Ru bond is compressed along the line gradually diverting from the 180° C−H···Ru angle (*cf.* Figure S13 in the Supporting Information). It suggests that the preferentially straight anagostic CH···Os bond adjusts its angles to the local strains in the β-$OsCp_2$ structure. It is also characteristic of the β-$OsCp_2$ phase that only one of the CH···Os bonds is significantly shorter than the others, which is another analogy to the structure of β-$RuCp_2$.

All but one hydrogen bond CH···π is compressed in osmocene and ruthenocene phases α and β, which suggests that these interactions continue to play a significant role in stabilizing the high-pressure structures of $OsCp_2$ and $RuCp_2$ (*cf.* Figure S14 in the Supporting Information).

Raman Spectroscopy. The fingerprint regions of Raman spectra (400−1600 cm^{-1}) for $OsCp_2$ and $RuCp_2$ at ambient pressure are analogues.[29] The most intense bands are present at 356, 413, 1059, and 1097 cm^{-1} for osmocene (Figure 10a),

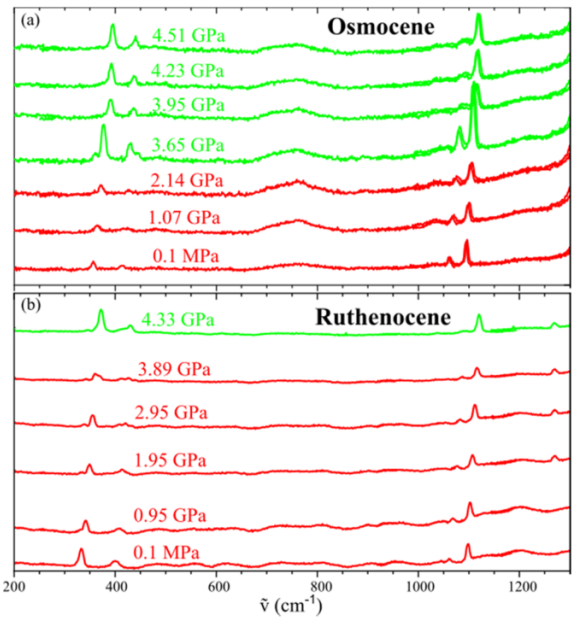

Figure 10. Raman spectra of (a) osmocene and (b) ruthenocene registered for the λ = 785 nm excitation wavelength. The α and β phases are colored red and green, respectively.

which are close to the corresponding bands at 332, 398, 1059, and 1097 cm^{-1}, for ruthenocene, respectively (Figure 10b). The peak at the smallest wavenumber corresponds to the metal−Cp ring stretching, the second peak (around 400 cm^{-1}) is related to the ring tilting, the band with medium intensity (around 1060 cm^{-1}) corresponds to the C−H out-of-plane bending, and the most intense band (around 1100 cm^{-1}) corresponds to the C−C streching.[30] Above 3.6 and 3.9 GPa, for osmocene and ruthenocene, respectively, when the new phase appears, the band at $\tilde{\nu}$ = 439 cm^{-1} starts to be more intense, while the band at $\tilde{\nu} \approx$ 1060 cm^{-1} corresponding to C−H out-of-plane bending significantly decreases. These changes are visible in the spectra of $OsCp_2$, while for $RuCp_2$, they are smaller, which can be caused by the 4-fold larger number of anagostic interactions formed in β-$OsCp_2$ than in $RuCp_2$. All bands shift with the increasing pressure to the higher-energy region (*cf.* Figure S15 in the Supporting Information), but a rapid change of the trend at the critical pressure is visible only for the metal−Cp ring stretching mode, while the bands of higher energies are less sensitive to the high-pressure changes.

Crystal Structure Energy Calculations. In order to evaluate the energetic effect of the crystal-symmetry change between osmocene phases α and β as well as for the quantitative comparison of the aggregation energy of osmocene and ruthenocene phases, we performed the crystal structure single-point energy (SPE) calculations. The SPE calculations were performed for the crystal structures exactly as determined by us for ruthenocene[2] and for osmocene in this study; no optimization of these structures was activated. The SPE values obtained in this way for ruthenocene (−410 773 kJ mol^{-1} for α-$RuCp_2$ at 0.1 MPa) are generally lower than the SPE for osmocene (−403 322 kJ mol^{-1} for α-$OsCp_2$ at 0.1

https://doi.org/10.1021/acs.jpcc.3c04579
J. Phys. Chem. C 2023, 127, 19250−19257

MPa, Figure 11). The SPE value of phase β-$OsCp_2$ is about 300 kJ mol^{-1} higher than that for phase α. According to our

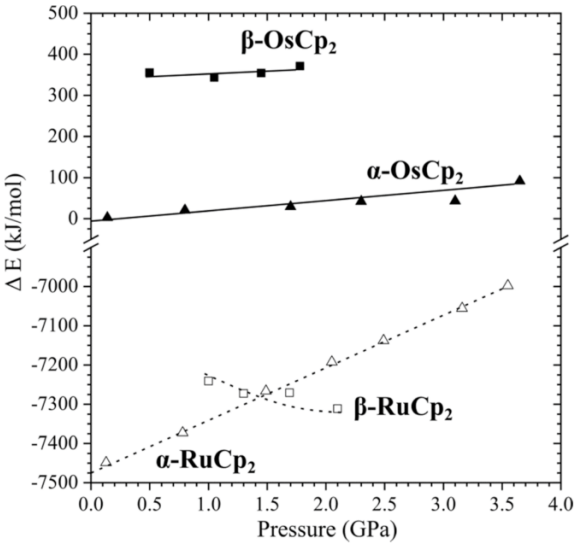

Figure 11. Relative single-point energies calculated for osmocene (full symbols, solid lines) and ruthenocene (open symbols, dashed lines) plotted as a function of pressure for phases α (triangles) and β (squares). The computations used the DFT/PBE method and the LANL2DZ basis set for Os and Ru; for C and H atoms, the SDD basis set with a pseudopotential and D95, respectively. All energy points are related to that of α-$OsCp_2$ at 0.1 MPa.

computations, the rate of energy change of compressed α-$RuCp_2$ is 125 kJ GPa^{-1}, which is 5 times larger than that of $OsCp_2$ (25 kJ GPa^{-1}). It indicates that the crystal structure of α-$RuCp_2$ is more sensitive to compression. Interestingly, the SPE for β-$RuCp_2$ intersects with the energy for phase α at about 1.5 GPa. This intersection point corresponds to the stability regions of $RuCp_2$ phases α and β. However, our calculations for $OsCp_2$ have not revealed such an intersection point up to 2 GPa, which can be an indication that instead of the SPE calculations, the geometry optimization should be performed. It is plausible that the considerable changes in the molecular dimensions of $OsCp_2$, such as the Os−Cp_c distance (Cp_c denotes the centroid of the Cp ring), shown in Figure S16, are not correctly represented by the SPE calculations. Due to their extensive computing power requirements, the crystal structure SPE calculations were performed only for the fixed molecular geometry. Presently, further studies involving the optimization of molecular geometry are planned to resolve this problem.

CONCLUSIONS

The structure of the new high-pressure phase β of osmocene revealed in this study clearly indicates a systematic change of properties in the series of prototypic metallocene compounds with the general formula MCp_2. For the series of 18-e configuration compounds $FeCp_2$, $RuCp_2$, and $OsCp_2$, we found a gradual increase of the negative electrostatic potential on the molecular surface around the metal cations, which correlates with its H-acceptor capability, 1-fold in β-$RuCp_2$ and 4-fold in β-$OsCp_2$. The stronger H-affinity of $OsCp_2$ differentiates its high-pressure β-phase from that of $RuCp_2$, despite their nearly identical ambient-pressure α-phases. The significant role of high-pressure-promoted anagostic bonds in β-$OsCp_2$ and $RuCp_2$ can be extended to their atmospheric α-phases, where similar contacts H···Os and H···Ru, albeit longer than the sums of van der Waals radii, are present. The crystal structures of phases III-$FeCp_2$, α-$RuCp_2$, α-$OsCp_2$, β-$RuCp_2$, and β-$OsCp_2$ confirm that hydrogen bonds CH···π play a significant role in all these phases, although their role is reduced compared to the anagostic bonds in phases β-$RuCp_2$ and β-$OsCp_2$. The presence of CH···π bonds and the preference for the eclipsed conformers both combine in favoring the orthorhombic phases III-$FeCp_2$, α-$RuCp_2$, and α-$OsCp_2$. However, the clearly lowest H-affinity of Fe corroborates the exceptional stability of this structure in the low-temperature region, as well as the preference for the high-pressure structure of phase I′-$FeCp_2$ dominated by hydrogen bonds CH···π.[8] The dielectric response of ferrocene crystals,[31,32] as well as the conformational features recently revealed in the new modulated structure of phase I″ of ferrocene,[31] suggests a contribution of dipole−dipole cohesion forces, which until recently were not considered. The weaker anagostic interactions and a stronger contribution of other types of cohesion forces can contribute to the presently known distinctly higher number of crystal phases (I, I′, I″, II, and III) of ferrocene compared to other simple metallocenes, e.g., only two phases are known for osmocene, ruthenocene, and nickelocene. These intermolecular forces interplay with the conformational features of metallocene compounds, leading to their different structures and properties.

ASSOCIATED CONTENT

Supporting Information

The Supporting Information is available free of charge at https://pubs.acs.org/doi/10.1021/acs.jpcc.3c04579.

Powder patterns of osmocene measured in a DAC chamber; photos of β-$OsCp_2$ decompression; average of torsion angles Ci_1−Cp_{c1}−Cp_{c2}−Ci_2; angle Cp_{c1}−Os−Cp_{c2} plotted as a function of pressure; rotation of β-$OsCp_2$ molecules breaking the mirror plane symmetry, CH···M contact arrangement in α-$RuCp_2$, α-$OsCp_2$, and III-$FeCp_2$ view along [101] and [010] directions; reconstructed sections $h0l$ by instruction UNWRAP of CrysAlis for β-$OsCp_2$ and β-$RuCp_2$; anagostic contact lengths for $FeCp_2$, $RuCp_2$, and $OsCp_2$; calculated charge distribution on metal centers (Os/Ru) as a function of pressure; anagostic contact angle as a function of pressure; shortest CH···π bonds for osmocene and ruthenocene plotted as a function of pressure; relative shifts of Raman bands for osmocene plotted as a function of pressure; M−Cp_c distances in ruthenocene and osmocene plotted as a function of pressure; intermolecular potentials in the crystal structures of osmocene; and experimental and crystal data of osmocene (PDF)

Accession Codes

The crystallographic and structural information has been deposited in the Cambridge Crystallographic Database Centre as supporting publications with numbers CCDC 2201960−2201966 and 2201971−2201975. Their copies can be obtained free of charge from www.ccdc.cam.ac.uk.

https://doi.org/10.1021/acs.jpcc.3c04579
J. Phys. Chem. C 2023, 127, 19250−19257

AUTHOR INFORMATION

Corresponding Author

Andrzej Katrusiak − *Faculty of Chemistry, Adam Mickiewicz University, 61-614 Poznań, Poland;* orcid.org/0000-0002-1439-7278; Phone: +48 61 829 1590; Email: katran@amu.edu.pl

Authors

Ida Moszczyńska − *Faculty of Chemistry, Adam Mickiewicz University, 61-614 Poznań, Poland;* orcid.org/0000-0002-0791-2278

Iwona Gulaczyk − *Faculty of Chemistry, Adam Mickiewicz University, 61-614 Poznań, Poland*

Complete contact information is available at: https://pubs.acs.org/10.1021/acs.jpcc.3c04579

Notes

The authors declare no competing financial interest.

ACKNOWLEDGMENTS

This study was supported by the Polish Ministry of Higher Education. I.M. is grateful to the Adam Mickiewicz University in Poznań for financial support, Minigrant for Ph.D. student 017/02/SNŚ/0018.

REFERENCES

(1) Paliwoda, D.; Kowalska, K.; Hanfland, M.; Katrusiak, A. U-Turn Compression to a New Isostructural Ferrocene Phase. *J. Phys. Chem. Lett.* **2013**, *4*, 4032−4037.

(2) Moszczyńska, I.; Katrusiak, A. Competition between Hydrogen and Anagostic Bonds in Ruthenocene Phases under High Pressure. *J. Phys. Chem. C* **2022**, *126*, 5028−5035.

(3) Seiler, P.; Dunitz, J. D. Low-Temperature Crystallization of Orthorhombic Ferrocene: Structure Analysis at 98 K. *Acta Crystallogr., Sect. B: Struct. Crystallogr. Cryst. Chem.* **1982**, *38*, 1741−1745.

(4) Hardgrove, G. L.; Templeton, D. H. The Crystal Structure of Ruthenocene. *Acta Crystallogr.* **1959**, *12*, 28−32.

(5) Bobyens, J. C. A.; Levendis, D. C.; Bruce, M. I.; Williams, M. L. Crystal Structure of Osmocene, $Os(\eta\text{-}C_5H_5)_2$. *J. Crystallogr. Spectrosc. Res.* **1986**, *16*, 519−524.

(6) Vargas-Caamal, A.; Pan, S.; Ortiz-Chi, F.; Cabellos, J. L.; Boto, R. A.; Contreras-Garcia, J.; Restrepo, A.; Chattaraj, P. K.; Merino, G. How Strong Are the Metallocene-Metallocene Interactions? Cases of Ferrocene, Ruthenocene, and Osmocene. *Phys. Chem. Chem. Phys.* **2016**, *18*, 550−556.

(7) Seiler, P.; Dunitz, J. D. The Structure of Triclinic Ferrocene at 101, 123 and 148 K. *Acta Crystallogr., Sect. B: Struct. Crystallogr. Cryst. Chem.* **1979**, *35*, 2020−2032.

(8) Paliwoda, D.; Hanfland, M.; Katrusiak, A. Pressure-Enhanced Environment Effects in Ferrocene Phases. *J. Phys. Chem. C* **2019**, *123*, 25719−25723.

(9) Moszczyńska, I.; Katrusiak, A. Lattice-Strain Coupled to Molecular Conformation and Disorder in Compressed Nickelocene. *J. Phys. Chem. C* **2021**, *125*, 15670−15675.

(10) Seiler, P.; Dunitz, J. D. Low-Temperature Crystallization of Orthorhombic Ferrocene: Structure Analysis at 98 K. *Acta Crystallogr., Sect. B: Struct. Crystallogr. Cryst. Chem.* **1982**, *38*, 1741−1745.

(11) Ogasahara, K.; Sorai, M.; Suga, H. New Finding of a Stable Low-Temperature Phase in Ferrocene Crystal. *Chem. Phys. Lett.* **1979**, *68*, 457−460.

(12) Seiler, P.; Dunitz, J. D. The Structure of Nickelocene at Room Temperature and at 101 K. *Acta Crystallogr., Sect. B: Struct. Crystallogr. Cryst. Chem.* **1980**, *36*, 2255−2260.

(13) Bondi, A. van der Waals Volumes and Radii. *J. Phys. Chem. A* **1964**, *68*, 441−451.

(14) Batsanov, S. S. Van der Waals Radii of Elements. *Inorg. Mater.* **2001**, *37*, 871−885.

(15) Merrill, L.; Bassett, W. A. Miniature Diamond Anvil Pressure Cell for Single Crystal X-ray Diffraction Studies. *Rev. Sci. Instrum.* **1974**, *45*, 290−294.

(16) Piermarini, G. J.; Block, S.; Barnett, J. D.; Forman, R. A. Calibration of the Pressure Dependence of the R1 Ruby Fluorescence Line to 195 Kbar. *J. Appl. Phys.* **1975**, *46*, 2774−2780.

(17) Dziubek, K. F.; Jęczmiński, D.; Katrusiak, A. Pressure-Generated Hydrogen Bonds and the Role of Subtle Molecular Features in Tetrahydrofuran. *J. Phys. Chem. Lett.* **2010**, *1*, 844−849.

(18) Rigaku, O. D. *CrysAlisPro*; Rigaku Oxford Diffraction Ltd.: Yarnton, Oxfordshire, England, 2015.

(19) Katrusiak, A. Shadowing and Absorption Corrections of Single-Crystal High-Pressure Data. *Z. Kristallogr.—Cryst. Mater.* **2004**, *219*, 461−467.

(20) Budzianowski, A.; Katrusiak, A. High-Pressure Crystallographic Experiments with a CCD-Detector. In *High-Pressure Crystallography*; Springer: Dordrecht, 2004; Vol. *140*, pp 101−112.

(21) Sheldrick, G. M. Crystal Structure Refinement with SHELXL. *Acta Crystallogr., Sect. C: Struct. Chem.* **2015**, *71*, 3−8.

(22) Dolomanov, O. V.; Bourhis, L. J.; Gildea, R. J.; Howard, J. A. K.; Puschmann, H. OLEX2 : A Complete Structure Solution, Refinement and Analysis Program. *J. Appl. Crystallogr.* **2009**, *42*, 339−341.

(23) Frisch, M. J.; Trucks, G. W.; Schlegel, H. B.; Scuseria, G. E.; Robb, M. A.; Cheeseman, J. R.; Scalmani, G.; Barone, V.; Petersson, G. A.; Nakatsuji, H.; Li, X.; Caricato, M.; Marenich, A. V.; Bloino, J.; Janesko, B. G.; Gomperts, R.; Mennucci, B.; Hratchian, H. P.et al. *Gaussian 16*, revision C.01; Gaussian, Inc.: Wallingford, CT, 2016.

(24) Schuchardt, K. L.; Didier, B. T.; et al. Basis Set Exchange: A Community Database for Computational Sciences. *J. Chem. Inf. Model.* **2007**, *47*, 1045−1052.

(25) Feller, D. The Role of Databases in Support of Computational Chemistry Calculations. *J. Comput. Chem.* **1996**, *17*, 1571−1586.

(26) Ladik, J. J. Polymers as Solids: A Quantum Mechanical Treatment. *Phys. Rep.* **1999**, *313*, 171−235.

(27) Hu, S. Z.; Zhou, Z. H.; Robertson, B. E. Consistent Approaches to van Der Waals Radii for the Metallic Elements. *Z. Kristallogr.* **2009**, *224*, 375−383.

(28) Groom, C. R.; Bruno, I. J.; Lightfoot, M. P.; Ward, S. C. The Cambridge Structural Database. *Acta Crystallogr., Sect. B: Struct. Sci., Cryst. Eng. Mater.* **2016**, *72*, 171−179.

(29) Kimel'fel'd, Y. M.; Smirnova, E. M.; Aleksanyan, V. T. The Vibrational Spectra of Molecular Crystals of Ferrocene, Ruthenocene, Osmocene and Nickelocene. *J. Mol. Struct.* **1973**, *19*, 329−346.

(30) Parker, S. F.; Butler, I. R. Synthesis, Computational Studies, Inelastic Neutron Scattering, Infrared and Raman Spectroscopy of Ruthenocene. *Eur. J. Inorg. Chem.* **2019**, *2019*, 1142−1146.

(31) Katrusiak, A.; Rusek, M.; Dušek, M.; Petříček, V.; Szafrański, M. Dipole-Moment Modulation in New Incommensurate Ferrocene. *J. Phys. Chem. Lett.* **2023**, *14*, 3111−3119.

(32) Bermúdez-García, J. M.; Yáñez-Vilar, S.; Castro-García, S.; Señarís-Rodríguez, M. A.; Sánchez-Andújar, M. New Properties in Old Systems: Cooperative Electric Order in Ferrocene and Ammonia-Borane. *RSC Adv.* **2015**, *5*, 83818−83824.

Artykuł 5

Ida Moszczyńska, Marek Szafrański, Andrzej Katrusiak

New Osmocene and Ruthenocene Phases Reveal the Common Conformational Bahavior Regulated by Anagostic Bonds in Prototypical Matallocenes

***J. Phys. Chem Lett.*, 2025, DOI: 10.1021/acs.jpclett.5c00686**

Data akceptacji: 28.05.2025 (załączono wersję PROOF publikacji)

THE JOURNAL OF PHYSICAL CHEMISTRY LETTERS
A JOURNAL OF THE AMERICAN CHEMICAL SOCIETY

pubs.acs.org/JPCL

Letter

New Osmocene and Ruthenocene Phases Reveal the Common Conformational Behavior Regulated by Anagostic Bonds in Prototypical Metallocenes

Ida Moszczyńska, Marek Szafrański, and Andrzej Katrusiak*

Cite This: https://doi.org/10.1021/acs.jpclett.5c00686

Read Online

ACCESS | Metrics & More | Article Recommendations | Supporting Information

ABSTRACT: Ruthenocene and osmocene, under normal conditions isostructural to low-temperature ferrocene phase III, have been regarded as prototypical metallocenes exclusively present in the energetically favored eclipsed conformation. This strong preference contrasts with ferrocene, which exhibits the staggered, rotated, eclipsed, disordered, and modulated conformations in its five polymorphic forms. Here we show that ruthenocene at 394.0 K and osmocene at 421.5 K transform to new higher-symmetry isostructural phases, where the cyclopentadienyl rings become disordered in two modes: seesaw tilts hinged on the metal cation and rotations about the molecular pseudo-C_5 axis. The transitions' entropy change and the Fourier transformations of the diffraction data indicate the hindered rotations, with molecules dynamically disordered between the staggered and eclipsed conformations, whereas in the final structural models the electron density distribution around the rings, calculated from the atomic displacement parameters of refined atomic sites, is continuous. For the prototypical metallocenes, a common pattern of transformations leading to disordered conformations has been connected with intramolecular anagostic bonds CH···M (M = Fe, Ni, Ru, Os). Their strength correlates with the critical temperatures of phase transitions when the anagostic bonds are broken.

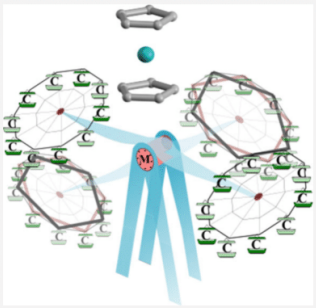

Prototypical metallocenes MCp_2, where M is a metal dication and Cp denotes the cyclopentadienyl $[C_5H_5]^-$ anion, are textbook examples of conformationally dependent solid-state phases.[1−9] Both gas-phase electron diffraction[10,11] and theoretical calculations[12,13] consistently indicate that the eclipsed conformer of ferrocene ($FeCp_2$) is 3.8 ± 1.3 kJ mol^{-1} more stable than the staggered one. Ferrocene is a stunning example of different crystal phases depending on the molecular conformation. The conformation, i.e., the position of one Cp ring (Cp1) relative to the other (Cp2), is measured by torsion angle τ (C−Cp1 centroid−Cp2 centroid−C′) between the closest C atoms of the opposite Cp rings around the (pseudo)-D_5 axis. Ferrocene in its ambient phase I initially was associated only with the staggered conformation (τ = 36°),[14] but the disorder of the Cp rings[15,16] implies an entanglement of populations of other conformers,[17] too. A high pressure of 3.24 GPa is needed to order the Cp rings exclusively in the staggered conformation.[7,18−20] At ambient pressure (0.1 MPa), below 172.8 K, ferrocene transforms to the conformationally modulated disordered phase I″;[21] below 163.5 K, in phase II, the molecules order in independent conformers rotated right and left (τ = ±8° and ±9°),[1] and in subsequent phase III the molecules assume the eclipsed conformation (τ = 0°).[2] The low-temperature ferrocene phase III is isostructural with ambient-pressure phase α of ruthenocene[22] and osmocene.[4] Recently, we obtained new structurally different high-pressure phase β of ruthenocene (space group *Pcmb*) and high-pressure phase β of osmocene (space group *Pcab*), but their conformers remained eclipsed.[23,24] This exceptional stability of ruthenocene ($RuCp_2$)[22,23] and osmocene ($OsCp_2$)[4,24] in the eclipsed conformation was puzzling when taking into account the similar molecular dimensions (distance M−Cp at ambient conditions in ferrocene is 1.651 Å,[18] that in ruthenocene is 1.812 Å, and that in osmocene is 1.815 Å) as those of ferrocene, the same configuration of 18 valence electrons as well as the similar potential energy favoring the eclipsed conformers[10−12,25−27] by ca. 4 kJ mol^{-1}, and when confronted with the partly or fully built staggered conformers, ferrocene phases I, I′ and I″. Nickelocene,[28,29] vanadocene,[30] chromocene,[31] cobaltocene,[28,32] and magnesocene[33] were only reported in the disordered or staggered conformations. It is even more puzzling that ferrocene has been so far the only known metallocene crystal that topochemically transforms between staggered and eclipsed phases.[2,9,34,35] Recently, we revealed the systematic increase of the H-acceptor capability of the central M ion in the series from ferrocene to ruthenocene and osmocene molecules.[24] The anagostic CH···Ru bonds

Received: March 6, 2025
Revised: May 16, 2025
Accepted: May 28, 2025

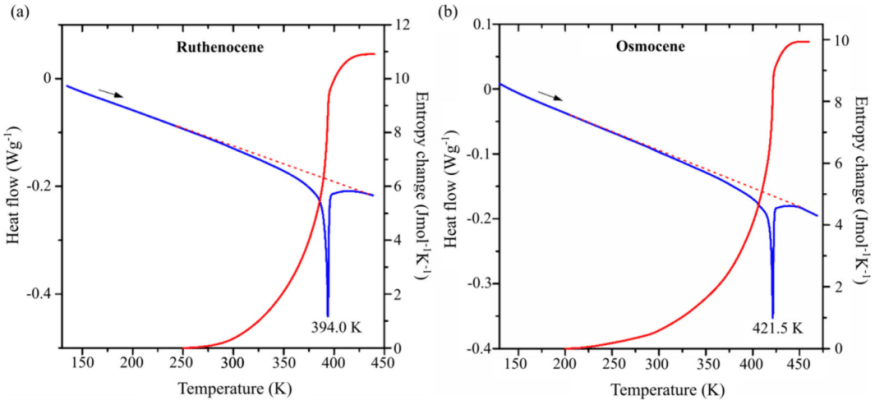

Figure 1. DSC heating runs (blue) and entropy changes (red) for (a) ruthenocene and (b) osmocene. The dashed lines indicate the baselines.

Table 1. Selected Crystal Data of Ruthenocene and Osmocene Phases α and γ[a]

	$RuCp_2$		$OsCp_2$	
Phase	α	γ	α	γ
Temperature	290 K	400 K	293 K	427 K
Space group	*Pnma*	*Fmmm*	*Pnma*	*Fmmm*
a (Å)	7.1097(1)	7.2161(5)	7.0848(3)	7.1956(4)
b (Å)	8.9752(2)	9.2195(6)	8.9122(5)	9.1560(5)
c (Å)	12.7934(3)	12.7724(6)	12.7883(7)	12.7736(7)
V (Å^3)	816.36(3)	849.73(9)	807.47(7)	841.56(8)
Z	4	4	4	4
Conformation	eclipsed	staggered 50%, eclipsed 50%	eclipsed	staggered 50%, eclipsed 50%

[a]See Table S1 in the Supporting Information.

between molecules, postulated by Borissova et al.[36] for ruthenocene phase α, become clearly more pronounced in high-pressure phase β, where they strongly stabilize the eclipsed conformer.[23,24] Likewise, short CH···Os bonds stabilize the eclipsed conformers of osmocene in its high-pressure phase β. The absence of short CH···M contacts in ferrocene coincides with the domination of its p-T diagram by the disordered and staggered phases I, I′ and I″. Here we reported the high-temperature breaking of the CH···Ru bonds in ruthenocene and the CH···Os bonds in osmocene, which induces the conformational transitions in these compounds. These observations provide the consistent landscape common for all prototypic metallocenes and their thermodynamic properties, at last.

Our calorimetric measurements show that the ruthenocene and osmocene crystals undergo high-temperature phase transitions at 394.0 and 421.5 K, respectively (Figure 1). The second-order character of these transitions is evident from the shape of the thermal anomalies and the lack of temperature hysteresis between the cooling and heating runs (cf. Figures S1 and S2 in the Supporting Information). This is also confirmed by the continuous change in entropy over a wide temperature range. The total gain in entropy accompanying the transition in ruthenocene amounts to $\Delta S = 11.5(6)$ J mol^{-1} K^{-1}. This value accounts for the configurational-entropy change, $\Delta S = R\ln(N_1/N_2)$, where $N_1/N_2 = 4$ is the ratio of configurations numbers in the high-temperature (N_1) and low-temperature (N_2) phases and R is the gas constant. For osmocene, the transition entropy is also high, $\Delta S = 9.9(5)$ J mol^{-1} K^{-1}, which corresponds to $\Delta S = R\ln 3.3$. These entropy changes clearly indicate the order–disorder mechanism of the transitions, where the high-temperature phases exhibit a 4-fold increase in the number of disorder sites. Furthermore, the stretch of observed thermal anomalies indicates that the disorder activation starts around 150 K below the critical temperatures (T_c − 150 K), as indicated in Figure 1 (cf. Figures S1–S4 in the Supporting Information).

The single-crystal X-ray diffraction (SCXRD) structural studies of the new γ phases of ruthenocene and osmocene were challenging due to the strong sublimation of these compounds above 350 K. To prevent the sublimation, we fixed the samples between cotton fibers gently pushed by a glass rod nearly matching the inner diameter of the capillary; we additionally filled the space between the rod and capillary with Distal (a two-component polymer glue). The capillaries were sealed by melting their ends in a microtorch: one capillary end was sealed first, then the cotton–sample–cotton–glass rod were inserted, and then the other end was melted together with the glass rod end. In the temperature range close to the T_c and in the γ phase, these protections of the sample crystal were sufficient to collect one full data set (during 30 min) and to start the subsequent one: after 5–10 min, the sample crystal started to move due to its sublimation. During one 30 min data collection, the intensity of control reflections dropped by about 90%; the reflection intensities accounted for this sublimation effect (cf. Figure S5). Despite these experimental difficulties, the structures were solved straightforwardly by direct methods in Shelxs,[37] and in the Fourier maps the electron density peaks clearly indicated the carbon atoms of the Cp ring disordered in four sites two due to the seesaw movement of molecules about

https://doi.org/10.1021/acs.jpclett.5c00686
J. Phys. Chem. Lett. XXXX, XXX, XXX−XXX

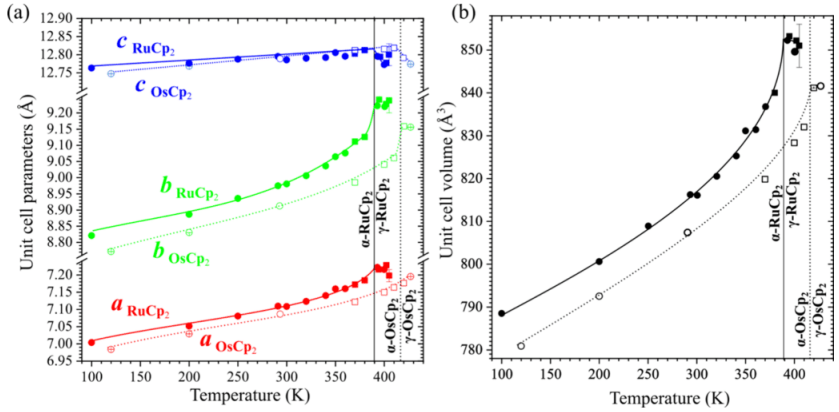

Figure 2. Thermal expansion of (a) unit-cell parameters of $RuCp_2$ (full symbols, solid lines) and $OsCp_2$ (open symbols, dotted lines) and (b) volume. Vertical solid and dotted lines mark the phase transitions. Squares and circles indicate the PXRD and SCXRD data, respectively. All estimated standard deviations (ESDs) are smaller than the plotted symbols.

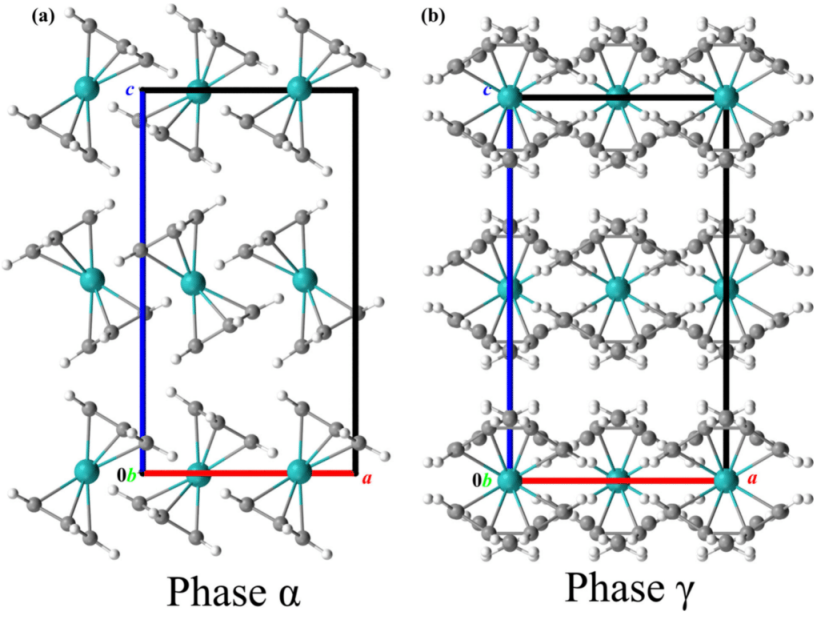

Figure 3. Crystal structures of $RuCp_2$ (a) in phase α at 293 K and (b) in phase γ at 395 K.

the [y]-axis and another two due to the rotation of the Cp rings by 36° about the pseudo-C_5 molecular axis. These clear locations of 4-fold disordered Cp rings were consistent for the γ phases of ruthenocene and osmocene, and their 4-fold disorder indicated by the entropy gains, associated with the transitions between the α and γ phases, were close to Rln 4 (see the calorimetric results presented above). All this information consistently confirmed the disordering mode, where the Cp ring jumps between two sites 36° apart about the pseudo-C_5 axis and between two sites one inclined by 60° to the other in the seesaw mode about the [z]-axis. The new γ phases of ruthenocene and osmocene, determined by SCXRD (cf. detailed information about the measurements and crystals are available in Experimental Section, in the Supporting Information, and in Table S1) at 400 K for $RuCp_2$ and 427 K for $OsCp_2$, are isostructural (Table 1). The group−subgroup symmetry relations between phases γ and α are consistent with the continuous character of the transitions. The unit-cell parameters and thermal expansions of $RuCp_2$ and $OsCp_2$ phases α and γ are similar (Figure 2). The thermal expansion of parameters a and b clearly increases when approaching T_c, whereas the thermal expansion of parameter c remains nearly constant. Above the transition temperatures, the c parameters display a strong negative thermal expansion, also observed for parameters a and b of ruthenocene and parameter b of osmocene.

This thermal expansion reflects structural transformations. The Ru and Os atoms remain at the D_{2h}-symmetric special

https://doi.org/10.1021/acs.jpclett.5c00686
J. Phys. Chem. Lett. XXXX, XXX, XXX−XXX

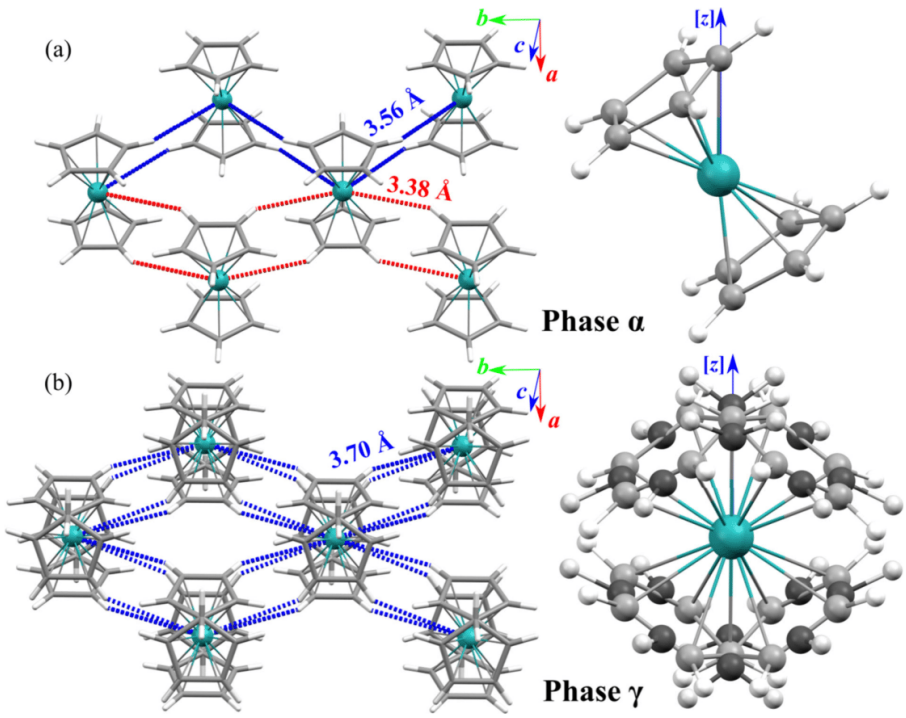

Figure 4. Autostereographic projections of ruthenocene phases (a) α and (b) γ and the ordered and disordered molecules inclined to the $[z]$ direction by angle $\alpha_{[z]}$. The shortest CH···Ru distances are indicated by red and blue dotted lines to distinguish symmetry-independent contacts in phase α at 290 K, while all indicated contacts in phase γ at 400 K are equivalent. One set of sites has been skipped in phase γ (b) for clarity. The components of disorder are deconvoluted in Figure S7.

position, at the intersection of three mirror planes (Figures 3 and 4). At T_σ the $RuCp_2$ and $OsCp_2$ molecules become disordered in an unprecedented manner for all metallocenes. This disorder can be decomposed into two modes: (i) the seesaw motion of the molecules about the $[y]$-direction measured by angle $\alpha_{[z]}$ between the molecular pseudo-C_5 axis and the $[z]$-direction, angle $\alpha_{[z]}$, is close to $\pm 30°$ (cf. Figures 3, 4, and S6) and (ii) the Cp-ring rotations by angle φ = 36° about the molecular pseudo-C_5 axis (Figures 3 and 4). The seesaw disorder (i) leads to two half-occupied sites of each Cp ring, and (ii) each of these time-averaged half Cp rings is further divided into two 0.25-occupied sites due to the pseudo-C_{10} rotations mode. Two Cp1-ring sites A and B (Figure S7) are symmetry-independent, and they can assume different site occupation factors SOF_A and SOF_B (= 0.5 − SOF_A). Our refinements of both structures γ-$RuCp_2$ and γ-$OsCp_2$ yielded SOF_A = 0.25(3) and 0.25(2), respectively; hence, we fixed the SOF values at 0.25 in the final refinements. Thus, each Cp ring becomes disordered in four equally 0.25-occupied positions. The connected symmetry change is consistent with the number of 4 configurations derived from the calorimetric measurements.

The radial distribution of the electron density of carbon atoms in the Cp ring as a function of temperature through the ordered and disordered phases α and γ of ruthenocene is plotted in Figure 5. It shows that some superposition of the distributions is present in phase α, even at 100 K, but it becomes significant at 200 K. This superposition of the densities of incoherently vibrating neighboring atoms, clearly

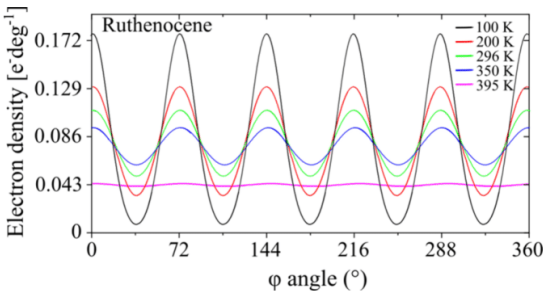

Figure 5. Electron density of carbon atoms radially distributed along the cyclopentadienyl ring as a function of temperature in ruthenocene phases α (100−350 K) and γ (395 K). These distributions were obtained by adding the probability distribution functions of the C atoms vibrating harmonically about their equilibrium positions, with the amplitudes derived from the anisotropic atomic displacement parameters in the directions tangential to the Cp ring. The amplitudes of the tangential components of mean atomic displacements were averaged for all atoms in the Cp ring and converted to the radial distribution. For phase γ, the atomic displacements were averaged separately for the disordered sites A and B; the common mean of the tangential components for atoms in A and B sites yielded the perfectly flat distribution (cf. Figure S9).

manifested at still higher temperatures, is consistent with the very wide pretransitional entropy increase observed in the calorimetric measurements (stretching for about 150 K), as

https://doi.org/10.1021/acs.jpclett.5c00686
J. Phys. Chem. Lett. XXXX, XXX, XXX−XXX

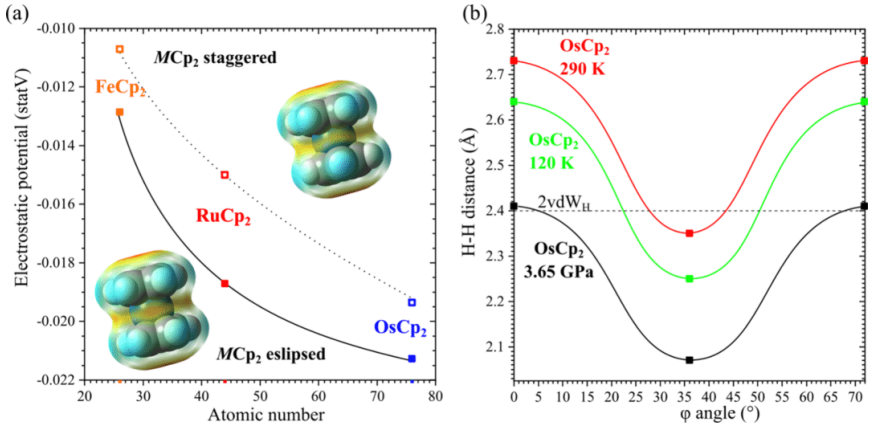

Figure 6. (a) Electrostatic potential on the molecular surface about the metal in ferrocene, ruthenocene and osmocene molecules; the insets show the electrostatic potential calculated for the molecule of osmocene in the staggered (top) and eclipsed (bottom) conformations. (b) Intermolecular H···H distances of the H atom involved in the anagostic bond to the closest H atom of the Cp ring in the experimental osmocene structures (eclipsed) and calculated for the other conformers.

well as with the low E_p barrier for the Cp ring rotations. This electron-density distribution in phase α, where the positions of atoms (ordering of the Cp rings) is beyond doubt, illustrates the coexistence of two aspects of the atomic positions: those long-range vibrations correlated consistently with the crystal symmetry and were thus traceable through the Fourier analysis, yielding fixed mean positions of atoms, and the uncorrelated thermal vibrations, strongly diminishing the form factors as a function of the scattering angle θ. Thus at 296 K, despite the well-defined mean atomic centers (at φ=n·72°, where n = 0, 1−5), the overlap region (at φ = n·72° + 36°) accounts for about half of the electron density (instantaneous atomic positions). At 350 K, on approaching the transition temperature, the overlap region accounts for about 75% of the atomic distribution around the ring, which testifies that the large-amplitude torsional vibrations are present, while each C-atom is clearly located in a single position, and no other sites are present.

Above the transition to phase γ, apart from the seesaw disorder, the practically continuous distribution of electrons of carbon atoms, in light of the 4-fold increased number of states in phase γ compared to phase α, can be interpreted as the strong thermal uncorrelated vibrations of atoms (rings) around their disordered mean (long-range correlated) positions at sites A (φ = n·72°) and B (φ = n·72° + 36°). This model is consistent with the Fourier map analysis, which reveals the positions of the electron densities of the disordered rings at two mean positions A and B radially separated by 36° along the ring circumference and their successful anisotropic refinement. This Fourier analysis confirms the long-range correlation of the atomic positions in the rings in the crystal (cf. Figure S8). It should be stressed that the continuously nearly constant distribution of the electron density resulting from the summation of atoms in both sites A and B and their thermal vibrations is the projection of all the real crystal structure onto the independent part of the unit cell. The alternative interpretation of the continuous distribution of electrons in the Cp ring is its free rotation, but it would imply a much higher entropy change,[38] and no long-range correlations of atomic positions in the crystal would yield not the mean atomic sites in the Fourier maps but their continuous circular distribution. Therefore it is plausible that the ring positions persist to be correlated in phase γ, most likely through the hindered rotations of the ring additionally complicated by the seesaw jumps, and the strong thermal motions of the atoms lead to the atomic-density distribution overlaps. It should be stressed that in the structural refinements of all the structures in this work we have applied the harmonic model of atomic vibrations. It is adequate for the low-amplitude vibrations, but for the strongly vibrating Cp rings at high temperatures, such as those in phases α and γ of ruthenocene and osmocene, considerable anharmonic contributions are expected. The measurements of the anharmonic vibrations are hampered due to the limited resolution at high temperatures and the presence of strong X-ray scattering in these structures. The theoretical computations based on the harmonic approximation for isolated molecular dimers predict hindered-to-free rotor transitions at 220 K in the ferrocene dimer, at 270 K in the ruthenocene dimer, and at 350 K in the osmocene dimer.[26]

It should be also noted that the vibrations and disorder of Cp rings was thoroughly investigated for ferrocene, nickelocene, and other metallocenes.[11,25,26,39−45] The primary concern was the distinction between the Cp ring disorder as the result of the dynamic motion of either rigid MCp_2 molecules or their internal torsions. The vibrational spectroscopy, inelastic neutron scattering, and theoretical computations indicate the prevailing contribution of the intramolecular torsions. Most of these experiments were performed for the low and ambient temperatures only, except for one experiment on nickelocene at 350 K.[11]

The seesaw reorientations of the whole molecule about axis [y] are by angle $\alpha_{[z]}$ = 30.32(2)° for ruthenocene at 400 K and 30.42(2)° for osmocene at 427 K. It is remarkable that angle $\alpha_{[z]}$ between the molecular pseudo-C_5-axis and the crystal axis [z] change only by less than 1° through all temperature range between 100 and 440 K for $RuCp_2$ and $OsCp_2$ in their ordered α phases and disordered γ phases (cf. Figure S6). This angle $\alpha_{[z]}$ approximates the angle between the M−C bond and the pseudo-C_5 axis, which is consistent with the coupling of the seesaw tumbling and the Cp rings rotations. In fact, the seesaw

https://doi.org/10.1021/acs.jpclett.5c00686
J. Phys. Chem. Lett. XXXX, XXX, XXX−XXX

movement of ring 1 from its site $Cp1_A$ brings it to site $Cp1_B$ (Figures 4 and S7), and a ring rotation of 36° is needed to bring the ring into the new $Cp1_A$ position. Likewise, the seesaw movement connects sites $C2_A$ with $C2_B$ and $C2_B$ with $C2_A$.

We have shown recently that the new high-pressure phase β of ruthenocene and the new phase β of osmocene were stabilized by anagostic CH···M bonds.[23,24] The theoretical computations of the charge distribution in $FeCp_2$, $RuCp_2$ and $OsCp_2$ molecules[24] show that the magnitude of electronegative potential around the metal site grows in the sequence $FeCp_2$ < $RuCp_2$ < $OsCp_2$, which make the H-acceptor capabilities grow in the same sequence: the lowest for $FeCp_2$ and the largest for $OsCp_2$. Most importantly, the computations showed that the magnitudes of the negative electrostatic potential on the molecular surface about the metal atoms are significantly larger for the eclipsed conformers and that the formation of anagostic bonds imposes steric hindrance on the staggered conformers. The electrostatic-potential magnitudes on the molecular surface about the M cation and the intermolecular H···H distances involving the closest neighbors of the H-atom involved in the CH···M bond are plotted in Figure 6. Thus, the close intermolecular H···H contacts favor the eclipsed conformers, too. The weak H-acceptor capability of the Fe-site in ferrocene and the absence of short CH···Fe contacts coincides with the domination of the p-T diagram of ferrocene by the disordered and staggered phases I, I′, and I″. Due to the temperature-agitated strong vibrations and rotations of Cp rings between the eclipsed and staggered conformations, the α phases of ruthenocene and osmocene are destabilized, and they both transform to the γ phases.

The dynamic Cp-ring disorder (independent pseudo-C_5 rotations in the disordering mode (ii) in γ-$RuCp_2$ and γ-$OsCp_2$ phases results in equal populations of the staggered and eclipsed conformers. However, the staggered conformation hinders the access to the M cation, and the anagostic interactions present in phases α and β are broken. The transitions of α-ruthenocene and α-osmocene to the γ phases increases the lengths of anagostic CH···M contacts by over 0.2 Å (*cf.* Figure S10), i.e., significantly beyond the sums of the van der Waals radii of H and Ru (3.33 Å) and H and Os (3.36 Å).[46,47] The direction of these contacts is close to the [y] direction, which is the axis of the seesaw motion (i), and therefore the increased CH···M distance corresponds to the largest elongation of the crystal along [y] on approaching the γ phase. The energy of breaking the CH···M bonds, the connected crystal expansion, and the entropy associated with the disorder all contribute to the considerable energy required for transforming the structures of ruthenocene and osmocene to phases γ. The plot in Figure 7 illustrates this relationship between the transition temperatures to the disordered phases with the CH···M distances, showing their essential role in controlling the molecular conformation.

We conclude that the new disordered phases of ruthenocene and osmocene revealed in this study widen a common landscape of transformations of prototypic metallocenes. Their unique sandwiched structure and axial M-Cp bonds result in conformational and dynamic properties inspiring the construction of molecular machines,[48,49] not to mention other multiple applications of metalocenes. According to our study, the rotations of Cp rings and their seesaw movements can be thermally activated in ruthenium and osmocene. To our knowledge, the seesaw disordering has not been considered so far for metallocenes, while there are intense studies of the

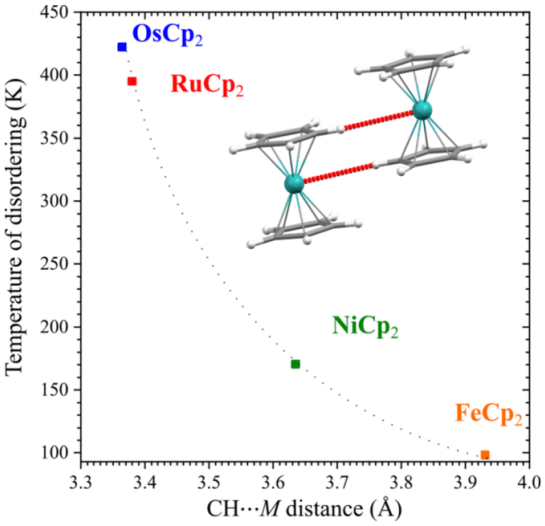

Figure 7. Temperature triggering conformational disordering in prototypic metallocenes as a function of the shortest CH···M distance, measured under ambient conditions (293 K/0.1 MPa).

nature of the Cp-ring rotations around the molecular C_5 axis. We established that in the solid state, the anagostic bonds CH···M are responsible for the strong stabilization of the eclipsed conformers in ruthenocene and osmocene phases α and β. This conclusion is consistent with the H-acceptor capability increasing in the series $FeCp_2$ < $RuCp_2$ < $OsCp_2$,[24] which is also illustrated by the series of CH···M distances observed in the crystals of these compounds and the reverse correlation of CH···M distances with the temperatures required for triggering the conformational disorder. Other factors, like the molecular mass and Cp1−Cp2 ring distance, can be also significant, as suggested by the absence of the eclipsed phase in $NiCp_2$ and the ordering of its Cp rings in the staggered conformation in phase I′, which for nickelocene extends to ambient-pressure low-temperature regions where ferrocene enters the eclipsed phase III. However, the role of anagostic bonds for the eclipsed conformers in ruthenocene and osmocene has been confirmed by their new γ phases.

■ EXPERIMENTAL METHODS

Differential scanning calorimetry (DSC) measurements were performed with a Q20000 calorimeter (TA Instruments), and DSC cooling and heating runs were measured for polycrystalline $OsCp_2$ and $RuCp_2$ samples at a temperature change rate of 10 K/min. The indium standard was used for calibration, whereas synthetic sapphire was used for specific heat calibration.

Single-crystal (SCXRD) and powder (PXRD) X-ray diffraction measurements were conducted for the samples sealed in thin-wall glass capillaries to prevent sublimation (cf. Supporting Information). An Agilent Xcalibur Atlas diffractometer, graphite-monochromated Mo Kα radiation, and an Oxford Cryostream Plus attachment were used to collect the low- and high-temperature X-ray diffraction data for all measurements for osmocene and for γ-ruthenocene at 400 K, while low- and high-temperature X-ray diffraction data for ruthenocene where collected with graphite-monochromated

https://doi.org/10.1021/acs.jpclett.5c00686
J. Phys. Chem. Lett. XXXX, XXX, XXX−XXX

Cu Kα radiation on a Bruker D8 Quest diffractometer, also equipped with an Oxford Cryostream Plus attachment. Detailed experimental and crystal data are presented in Tables S1−S3.

The observations of the sample crystals undergoing the phase transitions for ruthenocene at 395 K and osmocene at 422 K were conducted with an Olympus MVX 10 microscope equipped with a digital CCD camera.

The SCXRD experiments and preliminary data reduction were performed with the CrysAlis software from Rigaku Oxford Diffraction and Apex III from Bruker.[50,51] The SCXRD yielded the structures of $RuCp_2$ and $OsCp_2$ phases γ, solved by direct methods using Shelxt[52] and refined by full-matrix least-squares on F^2 values with Shelxl,[52] operated through Olex 2.[53] The H-atoms were located at idealized positions (C−H distance 1.0 Å) and their isotropic displacement parameter U_{iso} = 1.2 U_{eq} of their carriers. The high-temperature structures of ruthenocene and osmocene above T_c are disordered in a complex way involving two modes of seesaw tumbling and Cp ring reorientations by 36°, as described in the text and Supporting Information (cf. Figures 3, 4, S7, and S11); details of the refinements of the disordered structural models are given in the Supporting Information. The structures of ruthenocene and osmocene (2420348−2420357 and 2444809−2444813) have been deposited with the Cambridge Crystallographic Database Centre. The copies can be obtained free of charge on request from www.ccdc.cam.ac.uk.

The unit-cell parameters at 370 and 380 K for ruthenocene, as well as those 370, 400, 410, and 420 K for osmocene, were obtained by fitting the reflections in the PXRD patterns (marked with squares in the Figure 2) with program FullProf[54] implemented in the Match! software.[55]

■ ASSOCIATED CONTENT

Supporting Information

The Supporting Information is available free of charge at https://pubs.acs.org/doi/10.1021/acs.jpclett.5c00686.

Differential scanning calorimetry (DSC) heat flow plot for ruthenocene and osmocene, averaged carbon vibrational ellipsoid parameter U_1 tangential to the Cp rings for ruthenocene and osmocene, crystal structures of α- and γ-$RuCp_2$, deconvolution of a disordered molecule, angle $\alpha_{[z]}$ as a function of temperature for $RuCp_2$ and $OsCp_2$, CH···M distance for ruthenocene and osmocene as a function of temperature, discussion of unit-cell parameter changes, and entropy change calculation (PDF)

Transparent Peer Review report available (PDF)

■ AUTHOR INFORMATION

Corresponding Author

Andrzej Katrusiak − *Department of Materials Chemistry, Faculty of Chemistry, Adam Mickiewicz University, 61-614 Poznań, Poland;* orcid.org/0000-0002-1439-7278; Phone: +48 61 829 1590; Email: katran@amu.edu.pl

Authors

Ida Moszczyńska − *Department of Materials Chemistry, Faculty of Chemistry, Adam Mickiewicz University, 61-614 Poznań, Poland;* orcid.org/0000-0002-0791-2278

Marek Szafrański − *Faculty of Physics, Adam Mickiewicz University, 61-614 Poznań, Poland;* orcid.org/0000-0001-8178-5222

Complete contact information is available at: https://pubs.acs.org/10.1021/acs.jpclett.5c00686

Author Contributions

The manuscript was written through contributions of all authors. All authors have given approval to the final version of the manuscript.

Notes

The authors declare no competing financial interest.

■ ACKNOWLEDGMENTS

This study was supported by the Polish Ministry of Higher Education. I.M. is grateful to the Adam Mickiewicz University in Poznań for financial support.

■ REFERENCES

(1) Seiler, P.; Dunitz, J. D. The Structure of Triclinic Ferrocene at 101, 123 and 148 K. *Acta Crystallogr. Sect. B Struct. Crystallogr. Cryst. Chem.* **1979**, *35* (9), 2020−2032.

(2) Seiler, P.; Dunitz, J. D. Low-Temperature Crystallization of Orthorhombic Ferrocene: Structure Analysis at 98 K. *Acta Crystallogr. Sect. B Struct. Crystallogr. Cryst. Chem.* **1982**, *38* (6), 1741−1745.

(3) Hardgrove, G. L.; Templeton, D. H. The Crystal Structure of Ruthenocene. *Acta Crystallogr.* **1959**, *12* (1), 28−32.

(4) Boeyens, J. C. A.; Levendis, D. C.; Bruce, M. I.; Williams, M. L. Crystal Structure of Osmocene, $Os(\eta\text{-}C_5H_5)_2$. *J. Crystallogr. Spectrosc. Res.* **1986**, *16* (4), 519−524.

(5) Dunitz, J. D.; Orgel, L. E.; Rich, A. The Crystal Structure of Ferrocene. *Acta Crystallogr.* **1956**, *9* (4), 373−375.

(6) Moszczyńska, I.; Katrusiak, A. Lattice-Strain Coupled to Molecular Conformation and Disorder in Compressed Nickelocene. *J. Phys. Chem. C* **2021**, *125* (28), 15670−15675.

(7) Paliwoda, D.; Kowalska, K.; Hanfland, M.; Katrusiak, A. U-Turn Compression to a New Isostructural Ferrocene Phase. *J. Phys. Chem. Lett.* **2013**, *4* (23), 4032−4037.

(8) Levendis, D. C.; Boeyens, J. C. A. Analysis of the Molecular Conformation and Rotational Disorder in Crystalline Ferrocene and Nickelocene. *J. Crystallogr. Spectrosc. Res.* **1985**, *15* (1), 1−17.

(9) Katrusiak, A.; Rusek, M.; Dušek, M.; Petříček, V.; Szafrański, M. Dipole-Moment Modulation in New Incommensurate Ferrocene. *J. Phys. Chem. Lett.* **2023**, *14* (13), 3111−3119.

(10) Haaland, A.; Nilsson, J. E.; Olson, T.; Norin, T. The Determination of Barriers to Internal Rotation by Means of Electron Diffraction. Ferrocene and Ruthenocene. *Acta Chem. Scand.* **1968**, *22*, 2653−2670.

(11) Chhor, K.; Lucazeau, G.; Sourisseau, C. Vibrational Study of the Dynamic Disorder in Nickelocene and Ferrocene Crystals. *J. Raman Spectrosc.* **1981**, *11* (3), 183−198.

(12) Mohammadi, N.; Ganesan, A.; Chantler, C. T.; Wang, F. Differentiation of Ferrocene D_{5d} and D_{5h} Conformers Using IR Spectroscopy. *J. Organomet. Chem.* **2012**, *713*, 51−59.

(13) Coriani, S.; Haaland, A.; Helgaker, T.; Jørgensen, P. The Equilibrium Structure of Ferrocene. *ChemPhysChem* **2006**, *7* (1), 245−249.

(14) Eiland, P. F.; Pepinsky, R. X-Ray Examination of Iron Biscyclopentadienyl. *J. Am. Chem. Soc.* **1952**, *74* (19), 4971−4971.

(15) Brock, C. P.; Fu, Y. Rigid-Body Disorder Models for the High-Temperature Phase of Ferrocene. *Acta Crystallogr. Sect. B Struct. Sci.* **1997**, *53* (6), 928−938.

(16) Takusagawa, F.; Koetzle, T. F. A Neutron Diffraction Study of the Crystal Structure of Ferrocene. *Acta Crystallogr. Sect. B Struct. Crystallogr. Cryst. Chem.* **1979**, *35* (5), 1074−1081.

(17) Moszczyńska, I.; Paliwoda, D.; Katrusiak, A. Pressure-Tuned Conformers and Their Populations in Ferrocene. *J. Phys. Chem. C* **2024**, *128* (45), 19392−19397.
(18) Paliwoda, D.; Hanfland, M.; Katrusiak, A. Pressure-Enhanced Environment Effects in Ferrocene Phases. *J. Phys. Chem. C* **2019**, *123* (42), 25719−25723.
(19) Kuzmin, A. V.; Meletov, K. P.; Faraonov, M. A. Pressure and Temperature Transformations of the Molecular Conformation and Crystal Structure of Ferrocene $Fe^{2+}(\eta^5\text{-}C_5H_5)^{2-}$. *J. Phys. Chem. C* **2022**, *126* (7), 3688−3695.
(20) Meletov, K. Raman Study of the Conformational Instability of a Ferrocene Molecule at High Pressure: Influence of a Crystal Field. *J. Raman Spectrosc.* **2024**, *55* (10), 1105−1112.
(21) Katrusiak, A.; Rusek, M.; Dušek, M.; Petříček, V.; Szafrański, M. Dipole-Moment Modulation in New Incommensurate Ferrocene. *J. Phys. Chem. Lett.* **2023**, *14* (13), 3111−3119.
(22) Hardgrove, G. L.; Templeton, D. H. The Crystal Structure of Ruthenocene. *Acta Crystallogr.* **1959**, *12* (1), 28−32.
(23) Moszczyńska, I.; Katrusiak, A. Competition between Hydrogen and Anagostic Bonds in Ruthenocene Phases under High Pressure. *J. Phys. Chem. C* **2022**, *126* (10), 5028−5035.
(24) Moszczyńska, I.; Gulaczyk, I.; Katrusiak, A. Giant Deformation between Osmocene Phases Induced by Anagostic Bonds Promoted under High Pressure. *J. Phys. Chem. C* **2023**, *127* (38), 19250−19257.
(25) Boeyens, J. C. A.; Levendis, D. C. Force Field Study of Ring Orientation in Metallocenes. *South African J. Chem.* **1982**, *35* (4), 144−152.
(26) Ferreira Da Cunha, T.; Calderini, D.; Skouteris, D. Analysis of Partition Functions for Metallocenes: Ferrocene, Ruthenocene, and Osmocene. *J. Phys. Chem. A* **2016**, *120* (27), 5282−5287.
(27) Vargas-Caamal, A.; Pan, S.; Ortiz-Chi, F.; Cabellos, J. L.; Boto, R. A.; Contreras-Garcia, J.; Restrepo, A.; Chattaraj, P. K.; Merino, G. How Strong Are the Metallocene−Metallocene Interactions? Cases of Ferrocene, Ruthenocene, and Osmocene. *Phys. Chem. Chem. Phys.* **2016**, *18* (1), 550−556.
(28) Pfab, W.; Fischer, E. O. Zur Kristallstruktur Der Di-cyclopentadienyl-verbindungen Des Zweiwertigen Eisens, Kobalts Und Nickels. *Z. für Anorg. und Allg. Chemie* **1953**, *274* (6), 316−322.
(29) Seiler, P.; Dunitz, J. D. The Structure of Nickelocene at Room Temperature and at 101 K. *Acta Crystallogr. Sect. B Struct. Crystallogr. Cryst. Chem.* **1980**, *36* (10), 2255−2260.
(30) Antipin, M. Y.; Boese, R. Structure of Vanadocene in the Temperature Interval 108−357 K and the Nature of the Ring Disorder. *Acta Crystallogr. Sect. B Struct. Sci.* **1996**, *52* (2), 314−322.
(31) Weiss, E.; Fischer, E. O. Zur Kristallstruktur von Di-Cyclopentadienyl-Chrom(II). *Z. für Anorg. und Allg. Chemie* **1956**, *284* (1−3), 69−72.
(32) Antipin, M. Y.; Boese, R.; Augart, N.; Schmid, G. Redetermination of the Cobaltocene Crystal Structure at 100 and 297 K: Comparison with Ferrocene and Nickelocene. *Struct. Chem.* **1993**, *4* (2), 91−101.
(33) Bünder, W.; Weiss, E. Verfeinerung Der Kristallstruktur von Dicyclopentadienylmagnesium, $(\eta\text{-}C_5H_5)_2Mg$. *J. Organomet. Chem.* **1975**, *92* (1), 1−6.
(34) Braga, D.; Grepioni, F. Crystal Construction and Molecular Interplay in Solid Ferrocene, Nickelocene, and Ruthenocene. *Organometallics* **1992**, *11* (2), 711−718.
(35) Azokpota, C.; Pommier, C.; Berar, J. F.; Calvarin, G. Etudes Calorimetrique et Radiocristallographique Du Cobaltocene et Du Ruthenocene Entre 77 et 298 K. *J. Organomet. Chem.* **1977**, *135* (1), 125−135.
(36) Borissova, A. O.; Antipin, M. Y.; Perekalin, D. S.; Lyssenko, K. A. Crucial Role of Ru···H Interactions in the Crystal Packing of Ruthenocene and Its Derivatives. *CrystEngComm* **2008**, *10* (7), 827−832.
(37) Sheldrick, G. M. *Acta Crystallogr.* **2008**, *A64*, 112−122.
(38) Page, M. I. The Energetics of Neighbouring Group Participation. *Chem. Soc. Rev.* **1973**, *2* (3), 295.
(39) Appel, M.; Frick, B.; Spehr, T. L.; Stühn, B. Molecular Ring Rotation in Solid Ferrocene Revisited. *J. Chem. Phys.* **2015**, *142* (11), 114503 DOI: 10.1063/1.4915067.
(40) Bodenheimer, J. S.; Low, W. A Vibrational Study of Ferrocene and Ruthenocene. *Spectrochim. Acta Part A Mol. Spectrosc.* **1973**, *29* (9), 1733−1743.
(41) Braga, D. Dynamical Processes in Crystalline Organometallic Complexes. *Chem. Reviews* **1992**, *92*, 633−665.
(42) Kearley, G. A Review of the Analysis of Molecular Vibrations Using INS. *Nucl. Instruments Methods Phys. Res. Sect. A Accel. Spectrometers, Detect. Assoc. Equip.* **1995**, *354* (1), 53−58.
(43) Kemner, E.; de Schepper, I. M.; Kearley, G. J.; Jayasooriya, U. A. The Vibrational Spectrum of Solid Ferrocene by Inelastic Neutron Scattering. *J. Chem. Phys.* **2000**, *112* (24), 10926−10929.
(44) Parker, S. F.; Butler, I. R. Synthesis, Computational Studies, Inelastic Neutron Scattering, Infrared and Raman Spectroscopy of Ruthenocene. *Eur. J. Inorg. Chem.* **2019**, *2019* (8), 1142−1146.
(45) Gardner, A. B.; Howard, S.; Waddington, T. C.; Richardson, R. M.; Tomkinson, J. The Dynamics of Ring Rotation in Ferrocene, Nickelocene and Ruthenocene by Incoherent Quadi-Elastic Neutron Scattering. *Chem. Phys.* **1981**, *57* (3), 453−460.
(46) Bondi, A. Van Der Waals Volumes and Radii. *J. Phys. Chem.* **1964**, *68* (3), 441−451.
(47) Hu, S. Z.; Zhou, Z. H.; Robertson, B. E. Consistent Approaches to van der Waals Radii for the Metallic Elements. *Z. fur Krist.* **2009**, *224* (8), 375−383.
(48) Chen, K. J.; Chen, P. L.; Horie, M. Dynamic Pseudorotaxane Crystals Containing Metallocene Complexes. *Sci. Rep.* **2017**, *7*, No. 14195.
(49) Scottwell, S. Ø.; Crowley, J. D. Ferrocene-containing non-interlocked molecular machines. *Chem. Commun.* **2016**, *52*, 2451−2464.
(50) *CrysAlis Pro*. Rigaku Oxford Diffraction Ltd.: Oxfordshire, England, 2015.
(51) *APEX3*. Bruker AXS Inc: Wisconsin, USA, 2017.
(52) Sheldrick, G. M. SHELXT - Integrated Space-Group and Crystal-Structure Determination. *Acta Crystallogr. Sect. A Found. Crystallogr.* **2015**, *71* (1), 3−8.
(53) Dolomanov, O. V.; Bourhis, L. J.; Gildea, R. J.; Howard, J. A. K.; Puschmann, H. OLEX2 : A Complete Structure Solution, Refinement and Analysis Program. *J. Appl. Crystallogr.* **2009**, *42* (2), 339−341.
(54) Rodriguez-Carvajal, J. *FullProf*Laboratoire Léon Brillouin (CEA-CNRS), 1990.
(55) Putz, H.; Brandenburg, K. *Match! Phase Analysis Using Powder Diffraction*. Crystal Impact: Bonn, Germany, 2016.

https://doi.org/10.1021/acs.jpclett.5c00686
J. Phys. Chem. Lett. XXXX, XXX, XXX−XXX

OŚWIADCZENIA

Poznań, 30.05.2025

Ida Moszczyńska

Zakład Chemii Materiałów

Uniwersytet im. Adama Mickiewicza w Poznaniu

Uniwersytetu Poznańskiego 8,

63-614 Poznań

Polska

Deklaracja autorska kandydata do stopnia doktora

W związku z aplikacją Idy Moszczyńskiej na stopień Doktora Nauk Chemicznych na Uniwersytecie im. Adama Mickiewicza w Poznaniu deklaruję, że jestem współautorem następujących publikacji:

- I. Moszczyńska, A. Katrusiak „*Lattice-strain Coupled to Molecular Conformation and Disorder in Compressed Nickelocene*" J. Phys. Chem. C, 2021, 125, 15670-15675
  Mój wkład w powstanie tej pracy dotyczył zaprojektowania i przeprowadzenia eksperymentów, przygotowania próbki do pomiarów wysokociśnieniowych w komorze diamentowej, przygotowania próbki do pomiarów niskotemperaturowych, zebrania danych i ich analizy, dyskusji wyników, przeprowadzenia analizy strukturalnej i jej dyskusji, dokonania przeglądu literatury tematycznej, nakreślenia wersji roboczej manuskryptu oraz jego edycji.
- I. Moszczyńska, D. Paliwoda, A. Katrusiak „*Pressure-tuned Conformers and Their Populations in Ferrocene*" J. Phys. Chem. C 2024, 128 19392-19397
  Mój wkład w powstanie tej pracy dotyczył przeprowadzenia analizy strukturalnej i jej dyskusji, dyskusji wyników, dokonania przeglądu literatury tematycznej, nakreślenia wersji roboczej manuskryptu oraz jego edycji.

- I. Moszczyńska, A. Katrusiak *„Competition between Hydrogen and Anagostic Bonds in Ruthenocene Phases under High Pressure”* J. Phys. Chem. C 2022, 126, 5028-5035
  Mój wkład w powstanie tej pracy dotyczył zaprojektowania i przeprowadzenia eksperymentów, przygotowania próbki do pomiarów wysokociśnieniowych w komorze diamentowej, zebrania danych i ich analizy, dyskusji wyników, przeprowadzenia analizy strukturalnej i jej dyskusji, dokonania przeglądu literatury tematycznej, nakreślenia wersji roboczej manuskryptu oraz jego edycji.
- I. Moszczyńska, I. Gulaczyk, A. Katrusiak *„Giant Deformation between Osmocene Phases Induced by Anagostic Bonds Promoted under High Pressure*” J. Phys. Chem. C 2023, 127, 19250-19257
  Mój wkład w powstanie tej pracy dotyczył zaprojektowania i przeprowadzenia eksperymentów, przygotowania próbki do pomiarów wysokociśnieniowych w komorze diamentowej, zebrania danych i ich analizy, dyskusji wyników, przeprowadzenia analizy strukturalnej i jej dyskusji, dokonania przeglądu literatury tematycznej, nakreślenia wersji roboczej manuskryptu oraz jego edycji.
- I. Moszczyńska, M. Szafrański, A. Katrusiak *„New Osmocene and Ruthenocene Phases Reveal the Common Conformational Bahavior Regulated by Anagostic Bonds in Prototypical Matallocenes*” J. Phys. Chem. Lett. 2025 DOI: 10.1021/acs.jpclett.5c00686 (Akceptacja 28.05.2025)
  Mój wkład w powstanie tej pracy dotyczył zaprojektowania i przeprowadzenia eksperymentów, przygotowania próbki do pomiarów wysokotemperaturowych w kapilarze, zebrania danych i ich analizy, dyskusji wyników, przeprowadzenia analizy strukturalnej i jej dyskusji, dokonania przeglądu literatury tematycznej, nakreślenia wersji roboczej manuskryptu oraz jego edycji.

Moszczyńska A. Katrusiak

Poznań, 30.05.2025

Prof. Andrzej Katrusiak

Zakład Chemii Materiałów

Uniwersytet im. Adama Mickiewicza w Poznaniu

Uniwersytetu Poznańskiego 8,

63-614 Poznań

Polska

Deklaracja promotora

Potwierdzam swój wkład w następujące publikacje:

- I. Moszczyńska, A. Katrusiak „*Lattice-strain Coupled to Molecular Conformation and Disorder in Compressed Nickelocene*" J. Phys. Chem. C, 2021, 125, 15670-15675
- I. Moszczyńska, D. Paliwoda, A. Katrusiak „*Pressure-tuned Conformers and Their Populations in Ferrocene*" J. Phys. Chem. C 2024, 128 19392-19397
- I. Moszczyńska, A. Katrusiak „*Competition between Hydrogen and Anagostic Bonds in Ruthenocene Phases under High Pressure*" J. Phys. Chem. C 2022, 126, 5028-5035
- I. Moszczyńska, I. Gulaczyk, A. Katrusiak „*Giant Deformation between Osmocene Phases Induced by Anagostic Bonds Promoted under High Pressure*" J. Phys. Chem. C 2023, 127, 19250-19257
- I. Moszczyńska, M. Szafrański, A. Katrusiak „*New Osmocene and Ruthenocene Phases Reveal the Common Conformational Bahavior Regulated by Anagostic Bonds in Prototypical Matallocenes*" J. Phys. Chem. Lett. 2025 DOI: 10.1021/acs.jpclett.5c00686 (Akceptacja 28.05.2025)

Prowadziłem nadzór nad pracami doktorantki. Mój wkład w powstanie wyżej wymienionych prac polegał na pomocy w opisach wyników badań oraz bieżącym recenzowaniu szkicu manuskryptu.

Poznań, 02.06.2025

Prof. dr hab. Marek Szafrański

Zakład Fizyki Doświadczalnej Fazy Skondensowanej

Uniwersytet im. Adama Mickiewicza w Poznaniu

Uniwersytetu Poznańskiego 2,

63-614 Poznań

Polska

Oświadczenie o współautorstwie

Potwierdzam swój wkład w następującą publikację:

- I. Moszczyńska, M. Szafrański, A. Katrusiak „*New Osmocene and Ruthenocene Phases Reveal the Common Conformational Bahavior Regulated by Anagostic Bonds in Prototypical Matallocenes*" J. Phys. Chem. Lett. 2025 DOI: 10.1021/acs.jpclett.5c00686 (Akceptacja 28.05.2025)

  Mój wkład w powstanie wyżej wymienionej pracy dotyczył przeprowadzenia pomiarów DSC badanych próbek i nadzoru nad wykonaniem pomiarów rentgenowskich. Uczestniczyłam także aktywnie w pisaniu manuskryptu.

Dr Damian Paliwoda Poznań, 25.02.2025

European Spallation Source ERIC

Partikelgatan 2,

224 84 Lund

Sweden

Oświadczenie o współautorstwie

Potwierdzam swój wkład w następującą publikację:

- I. Moszczyńska, D. Paliwoda, A. Katrusiak „*Pressure-tuned Conformers and Their Populations in Ferrocene*" J. Phys. Chem. C 2024, 128 19392-19397

Mój wkład w powstanie wyżej wymienionej pracy dotyczył dostarczenia danych eksperymentalnych. Uczestniczyłem aktywnie w pisaniu manuskryptu.

Poznań, 25.02.2025

Prof. Iwona Gulaczyk

Zakład Chemii Kwantowej

Uniwersytet im. Adama Mickiewicza w Poznaniu

Uniwersytetu Poznańskiego 8,

63-714 Poznań

Polska

Oświadczenie o współautorstwie

Potwierdzam swój wkład w następującą publikację:

- I. Moszczyńska, I. Gulaczyk, A. Katrusiak „*Giant Deformation between Osmocene Phases Induced by Anagostic Bonds Promoted under High Pressure*" J. Phys. Chem. C 2023, 127, 19250-19257

  Mój wkład w powstanie wyżej wymienionej pracy dotyczył zaprojektowania i przeprowadzenie obliczeń w programie Gaussian, w tym dobór odpowiednich baz i strategii obliczeniowych. Uczestniczyłam także aktywnie w pisaniu manuskryptu.

Iwona Gulaczyk

OSIĄGNIĘCIA NAUKOWE

LISTA PUBLIKACJI NAUKOWYCH

1. Moszczyńska, I.; Szafrański, M.; Katrusiak, A. New Osmocene and Ruthenocene Phases Reveal the Common Conformational Bahavior Regulated by Anagostic Bonds in Prototypical Matallocenes. *J. Phys. Chem. Lett*, 2025 (Akceptacja 28.05.2025), $IF_{(2025)}$=4.8

2. Moszczyńska, I.; Golczak, A.; Sikorski, M.; Katrusiak, A. Fluorescence and absorption of Rhodamine 6G solutions as pressure standards for diamond-anvil cel. *Phys. Chem. Chem. Phys*. 2024, **26**, 27098-27105, DOI: 10.1039/d4cp03351e, $IF_{(2024)}$=2.9

3. Moszczyńska, I.; Paliwoda, D.; Katrusiak, A. Pressure-turned conformers and their populations in ferrocene. *J. Phys. Chem. C*. 2024, **128**, 19392-19397, DOI: 10.1021/acs.jpcc.4c05399, $IF_{(2024)}$=3.3

4. Patyk-Kaźmierczak, E.; Izquierdo-Ruiz, F.; Lobato, A.; Kaźmierczak, M.; Moszczyńska, I.; Olejniczak, A.; Recio, J. M. The curious case of proton migration under pressure in the malonic acid and 4,4'-bipiridine cocrystal. *IUCrJ*, 2024, **11**, 168-181 DOI: 10.1107/S2052252524000344, $IF_{(2024)}$=2.9

5. Moszczyńska, I.; Gulaczyk, I.; Katrusiak, A. Giant deformation between osmocene phases induced by anagostic bonds promoted under high pressure. *J. Phys. Chem. C* 2023, **127**, 19250-19257, DOI: 10.1021/acs.jpcc.3c04579, $IF_{(2023)}$=3.3

6. Moszczyńska, I.; Katrusiak, A. Competition between hydrogen and anagostic bonds in ruthenocene phases under high pressure. *J. Phys. Chem. C*, 2022 **126**, 5028-5035, DOI: 10.1021/acs.jpcc.1c10249, $IF_{(2022)}$=3.7

7. Moszczyńska, I.; Katrusiak, A. Lattice-strain coupled to molecular conformation and disorder in compressed nickelocene. *J. Phys. Chem. C* 2021, **125**, 15670-15675, DOI: 10.1021/acs.jpcc.1c04204, $IF_{(2021)}$=4.18

8. Runowski, M.; Sobczak, S.; Marciniak, J.; Bukalska, I.; Lis, S.; Katrusiak, A. Gold nanorods as a high-pressure sensor of phase transitions and refractive-index gauge. *Nanoscale*, 2019, **11**, 8718-8726, DOI: 10.1039/C9NR02792K, $IF_{(2019)}$=6.89

9. Rajewski, K. W., Bukalska, I., Katrusiak, A. Pressure-induced high-to-low Z' phase transition of conformationally disordered molecular crystal. *Cryst. Growth Des*. 2018, **18**, 3187-3192, DOI: 10.1021/acs.cgd.8b00282, $IF_{(2018)}$=4.15

LISTA KONFERENCJI NAUKOWYCH

(Międzynarodowe)

2025 35th European Crystallographic Meeting, *„Conformational transformations in ruthenocene and osmocene coupled to the CH···Ru and CH···Os bonds”* konferencja międzynarodowa w Poznaniu, prezentacja plakatowa

2024 34th European Crystallographic Meeting, *„Competition between CH···π and CH···M contacts in metallocenes structures”* konferencja międzynarodowa w Padwie, prezentacja plakatowa

2022 33rd European Crystallographic Meeting, *„High-Pressure Polymorphs of Osmocene and Ruthenocene”* konferencja międzynarodowa w Wersalu, prezentacja plakatowa

2021 IUCr High-Pressure Workshop, *„High-Pressure Transformation of Nickelocene”* konferencja międzynarodowa, prezentacja plakatu

2021 14th Frolic Goats High Pressure Diffraction Workshop, *„Pressure Induced Ordering of Nickelocene Molecule”* konferencja międzynarodowa, prezentacja referatu

2020 13th Frolic Goats High Pressure Diffraction Workshop, *„Pressure-Induced High to Low Z' Phase Transition of 6-chloro-4,4,5,7-Tetramethyldihydrocoumarin”* konferencja międzynarodowa, prezentacja plakatu

2018 11th Frolic Goats High Pressure Diffraction Workshop, *„Disordered structure of 6-chloro-4,4,5,7-tetramethyldihydrocoumarin and its phase transition”* konferencja międzynarodowa, prezentacja plakatu

2017 55th European High Pressure Reaserch Group Meeting, *„Pressure Effect on the Complication of Crystal Structures the Case Study on 6-chloro-4,4,5,7-tetramethyldihydrocoumarin”* konferencja międzynarodowa, prezentacja plakatu

2016 9th Frolic Goats High Pressure Diffraction Workshop, *„ Z' Reduction at High-Pressure β phase of on 6-chloro-4,4,5,7-tetramethyldihydrocoumarin”* konferencja międzynarodowa, prezentacja plakatu

(Ogólnopolskie)

2021 62. Konwersatorium Krystalograficzne, *„Nickelocene Molecule Orgering at High-Pressure Codnditions”* konferencja ogólnopolska, prezentacja plakatu

2018 60. Konwersatorium Krystalograficzne, *„Wpływ warunków ekstremalnych na unikalną topologię polimeru koordynacyjnego”* konferencja ogólnopolska, prezentacja plakatu

WYJAZDY ZAGRANICZNE/SZKOLENIA

1. Hercules European School, miesięczna międzynarodowa szkoła promieniowania synchrotronowego i neutronowego marzec 28.02.2022 – 01.04.2022 (DESY & EUROPEAN XFEL)

2. ESRF/ILL Summer School Programme, miesięczna studencka szkoła promieniowania synchrotronowego i neutronowego (ID06 Large Volume Press) 02.09 2018 – 29.09.2018

PROJEKTY NAUKOWE

1. SONATA16 Establishing the correlation between the acidity of coformers and the pressure of proton transfer in acid-base cocrystals (wykonawca) 01/2022- 05/2022

2. Kierownik Minigrantu Doktoranckiego IDUB Badania strukturalne metalocenów oraz pochodnych metalocenów w warunkach wysokiego ciśnienia (kierownik) 01/2021-12/2022

3. OPUS10 Porous materials under extreme conditions (wykonawca) 08/2017-06/2019